Higher order compact schemes and their applications to problems with complex geometries

by

Chitralekha Sarkar

DEPARTMENT OF MATHEMATICS
INDIAN INSTITUTE OF TECHNOLOGY GUWAHATI
GUWAHATI-781039, INDIA

January, 2017

Higher order compact schemes and their applications to problems with complex geometries

A thesis submitted

in partial fulfillment of the requirements

for the degree of

DOCTOR OF PHILOSOPHY

by

Chitralekha Sarkar

(Roll No. 09612312)

DEPARTMENT OF MATHEMATICS

INDIAN INSTITUTE OF TECHNOLOGY GUWAHATI

GUWAHATI - 781039, INDIA

January, 2017

Dedicated to my beloved parents
Shri. Amarendra Nath Sarkar and Smt. Indumati Sarkar

Certificate

It is certified that the work contained in this thesis entitled **"Higher order compact schemes and their applications to problems with complex geometries"** by **Chitralekha Sarkar,** a student of Department of Mathematics, Indian Institute of Technology Guwahati, for the award of the degree of Doctor of Philosophy has been carried out under my supervision and that this work has not been submitted elsewhere for a degree.

January, 2017

Dr. Durga Charan Dalal
Professor
Department of Mathematics
Indian Institute of Technology Guwahati

Acknowledgements

Completion of this thesis is possible due to the support and help of several people. I would like to take this opportunity to thank them all .

I would like to express my sincere gratitude to my thesis supervisor Prof. D. C. Dalal for his continuous support, constant encouragement and immense patience throughout all stages of the work. I am extremely grateful to him for spending his precious time in reading and providing valuable suggestions to complete this thesis. I would like to thank the doctoral committee members Prof. S. Natesan, Prof. S. N. Bora and Dr. A. K. De for their insightful comments, constructive criticism and valuable suggestions during the progress of my work. I would also like to express my sincere thanks to all the faculty members of the Department of Mathematics for their help and cooperation.

It is my privilege to express my deep sense of gratitude to Dr. Swapan Kumar Pandit for his help, timely suggestions and for spending invaluable time discussing my work. I would also wish to express my gratitude to Dr. Anjan Kumar Bhuniya for motivating me to pursue my research.

I take this opportunity to thank the Head, Department of Mathematics, IIT Guwahati for providing me the necessary facilities during my research work. I also thank CSIR, Govt. of India, for offering me financial assistance to carry out my research work. I would like to express my thanks to Sridhar da, Phatik da, Saurav da and Manoj da for their assistance in all official matters and also to our lab assistants Santanu da and Pranpratim da for their help.

I would like to express my heartfelt thanks to Manideepa di, Namita di, Jhuma, Deepanwita, Poulami and Gayatri for creating a homely atmosphere. We spent many enjoyable moments together which I will always treasure. I am also thankful to my colleagues and junior research mates: Debopam, Nasim, Abhishek, Anirban, Swarup, Pratibha, Tanushree, Koyel and many others for their help and cooperation in various occasions during my stay at IIT Guwahati.

I am extremely grateful to my parents (Baba and Maa), Boma, Borobaba, Mama, younger brother, elder brothers, sister and all other family members for their love, concern, care, encouragement and moral support throughout my life. I express my sincere and deepest sense of gratitude towards them for staying beside me all the time. I thank my well wishers and all people who have helped me directly or indirectly in this journey whose name I may have inadvertently missed. Above all, I thank God for everything.

January, 2017

With regards,

(**Chitralekha Sarkar**)

Department of Mathematics

Indian Institute of Technology Guwahati

Abstract

The thesis is aimed to modify an already existing higher order compact (HOC) finite difference scheme to enhance its applicability and robustness. To examine the robustness of the proposed scheme, it is applied to lid-driven cavity problems, natural and mixed convection problems including some magnetohydrodynamic effects in some complex geometries. Numerical results computed through the proposed HOC schemes are compared with analytical or established numerical results available in the literature and excellent agreements are found in all the cases.

A natural convection problem in a wavy enclosure in presence of magnetic field is studied numerically using the proposed scheme. The left and right walls of the enclosure are wavy whereas the top and bottom walls are straight. The bottom wall is much hotter compared to the side walls whereas the top wall is adiabatic. The effects of the use of porous media are studied. Streamlines and isotherms are plotted with different Rayleigh number, Hartmann number, Prandtl number and Darcy number. The effects of these parameters on the heat transfer rate are also discussed.

In order to explore whether a geometry like trapezoidal enclosure enhances the heat transfer rate or not, a mixed convection problem is solved using the proposed HOC scheme. The bottom wall is heated uniformly, the top wall moving with a constant velocity is adiabatic and the inclined walls are at low temperature. The parameters used to describe the flow characteristics and the heat transfer rate are Grashof number, Richardson number and Prandtl number. The influences of height (of the trapezoidal cavity with fixed bottom width) and also the width (of the bottom wall with fixed height) on the fluid flow and the heat transfer rate are discussed. A mixed convection problem in a vented cavity with bottom wavy wall is also included in this thesis work. The inlet is considered at the bottom part of the left wall, the rest part of this left wall is heated with a constant heat flux, the other walls are adiabatic whereas the outlet is at the top portion of the right vertical wall. The effects of parameters such as Rayleigh number, Reynolds number on the fluid flow and the heat transfer rate are discussed. The effects of the number of waves in the bottom wall are also studied.

The flow characteristics of an incompressible flow in a dilated channel in presence of magnetic field are also studied in this thesis where the dilated channel is assumed to be either lateral or axisymmetric. The effects of the Hartmann number and the Reynolds number on the flow behaviour are discussed.

Contents

List of Figures

List of Tables

1 Introduction

1.1 Background

Computational Fluid Dynamics (CFD) is a complex tool that has always been considered as a workflow consisting of many processes. Each process has its unique features in terms of algorithms, tools, and applications. The models of these processes consist of sets of partial or ordinary or integro-differential equations with boundary conditions. Such as in fluid dynamics, the well-known coupled partial differential equations (PDEs) are the Navier-Stokes (N-S) equations which are familiar as the model equations for fluid flow predictions. These systems of PDEs are highly non-linear coupled equations and not easy to solve. It is customary to say that the available techniques applied in CFD cannot be adopted without the existence of a computational grid that fills the flow domain. In most of the cases, CFD applications were mainly carried out on uniform rectilinear grids. This has the advantage of simpler governing equations and more robust solution algorithms. On the other hand, simple grids fail to simulate complex geometry of the fluid flow domains with reasonable degree of accuracy. Interestingly, the fact is that the flow conditions in majority of science and engineering applications are represented by complex geometries, not as simple as the rectangular or square domain where numerical simulation can easily be performed. So for the problem on irregular domains, it is still challenging to solve the partial differential equation efficiently.

In 1960s, the first efforts regarding the development of grid generation techniques in complex geometries were undertaken by a significant number of advanced methods namely, algebraic, elliptic, hyperbolic, parabolic, variational, Delaunay, advancing front etc. These methods reached a stage where calculations in fairly complicated multi-dimensional domains became possible. Because of its successful development, the field of numerical grid generation has already formed a separate mathematical discipline with

its own approaches and methodology.

In the mid 1980s, serious attention was directed towards casting the governing equations in coordinate free form in preparation for discretization over non-orthogonal curvilinear grids covering complex geometry flow domains. The methodology required algorithms for generating the computational grid that were simple for testing accuracy, convergence, and stability of the proposed solution techniques. At that time, these algorithms were simple, cumbersome, and offered very little control over the generated grid from the computational view point.

In the late 1980s, a new stage in the development of grid generation techniques was initiated. It was characterized by the creation of comprehensive, multipurpose, three dimensional grid generation codes which was aimed at providing a uniform environment for the construction of grids in arbitrary multidimensional geometries. Despite all these efforts, grid generation remains a major obstacle in CFD work flow and the most demanding process in terms of effort and time.

However, besides generation of computational grid, the importance of system of partial differential equations is unavoidable. The theory of PDEs is one of the most developed areas in mathematics. But instead of its success, very few problems of practical interest that require solutions of PDEs can be solved analytically. Numerical methods to obtain the approximate solutions of the problems are, therefore, preferable. In a numerical method, a continuous function present in the differential equation is discretized as a finite set of numbers and the original differential equation turns into a system of algebraic equations. Among the numerical methods, finite difference method (FDM), finite element method (FEM) and finite volume method (FVM) are well-known and widely used methods. The system of equations are then solved using efficient matrix solution algorithm.

Among all the three methods, FDM is one of the most effective and convenient numerical methods to solve the physical problems in various branches of continuum physics such as heat flow, diffusion, fluid dynamics, magnetohydrodynamic, electromagnetism, wave mechanism, radiation transfer, neutron transfer, elastic vibrations, medical fluid dynamics, bio engineering, soil physics, population dynamics etc. This method is relatively straight forward and can easily be applied to obtain the approximate solutions of boundary value problems. In finite difference scheme, the computational domain consists of the space-time grid and each variable is represented by its values at the grid points and the derivatives of the variable are approximated by the finite difference formula that uses values of the variable at a specified set of grid points. Error between the exact solution and the numerical solution appears due to the use of difference operator in

place of differential operator. This error is called the truncation error. This truncation error reflects the fact that a finite part of a Taylor series is used for approximations. The leading term in the truncation error determines the order of accuracy of the scheme. In lower order scheme, to get approximate solution one needs to take a finer grid which increases the computational costs. If the order of accuracy of a scheme is better than $O(h^2)$, where h is the distance between two successive grid points, the scheme is called a higher order scheme. These types of schemes are desirable because a coarser grid can be used to get a better approximated result for the higher order accuracy of the scheme which reduces the computational costs. In this context, it may be pointed out that a standard method to attain higher order scheme needs to use more number of grid points to approximate the derivatives present in the equation. Generally, a higher order scheme deals with non-compact stencils that utilizes a large number of grid points about which the differences are taken. So, the bandwidth of the resultant matrix increases. To avoid such difficulties, a concept of compact scheme centers the development of numerical scheme by using compact stencil, which utilizes the grid points directly adjacent to the grid point about which the differences are taken. So, compact higher order schemes are preferred to get approximate solutions of any differential equation. Several techniques are available to acquire higher order accuracy with compactness property. Among these schemes, the compact schemes described by Lele [43], Visbal [107] and others on compact stencils, are based on Padé approximation, which is an implicit relation between the derivatives and the functions at adjacent nodal points. They included information not only from the adjacent points to the node about which the differences are taken, but also included information from nodal points located at distance two or three steps away from that node. Very recently, Sen [90] has formulated fourth order compact scheme by discretizing each term in the PDE as fourth order accurate combining with Padé approximation.

There are compact schemes that use the original differential equation to replace the leading truncation error terms of the standard central difference approximation which are also popular higher order compact finite difference schemes, where the compactness is confined on a nine point compact stencil. Lax and Wendroff [42] first implemented this idea on transient hyperbolic PDEs to raise the temporal accuracy from one to two. Mackinnon and Johnson [48] then implemented this idea for higher order spatial accuracy on steady state convection-diffusion problems. Spotz and Carey [97] extended the idea of Mackinnon and Johnson to the steady state stream-function vorticity formulation of the two dimensional (2D) Navier-Stokes equations. Based on their ideas, Kalita *et al.* [36] developed a class of transient HOC schemes for the solution of unsteady 2D

convection-diffusion equations and extended their study to develop HOC schemes on non-uniform grids without transformation. To simulate fluid flow in a geometry beyond rectangular, Pandit *et al.*[68] developed HOC scheme on non-uniform orthogonal curvilinear grids. Some of the other useful techniques are, series expansion procedure of the differential equation by Gupta *et al* [23], exponential expansion of a definite integral of the convective coefficient of the PDE by Dennis and Hudson [15], weighted mean approximation by Gartland [19], weighted modified PDE method by Noye and Tan [61], and the high order upwind schemes of Yanwen [109] and Sesterhenn [91].

Recently, some HOC schemes are developed for problems with spherical geometries [86, 87, 88, 89]. These studies expand the applicability of the HOC schemes to a larger class of problems having complex geometries, particularly spherical in nature.

1.2 Convective heat transfer

The inclusion of heat transfer mechanism with fluid flow simulation is known as convective heat transfer. In this mechanism, heat transfer is affected by fluid flow in a system. In addition, convective heat transfer process predicts the amount of energy conveyed by the fluid. The convective heat transfer classifies into two branches: the natural convection [1, 6, 5, 7, 14, 50, 63, 65] and forced convection. Forced convection describes the heat transport by induced fluid motion which is forced to happen. This induced fluid flow motion requires consistent mechanical power. But in natural convection, the fluid is derived by a force generated naturally. Due to the presence of density gradient and gravitational field, buoyancy force is responsible for the fluid flows in natural convection. Buoyancy occurs due to the combined presence of the fluid density gradient and the body force. As the temperature distribution in the natural convection depends on the intensity of the fluid currents which is dependent on the temperature potential itself, the quantitative analysis of natural convection heat transfer is very difficult. In such cases, numerical investigation is much more essential in describing the flow physics. Two types of natural convective heat transfer phenomena can be observed in the nature. In the first type, external free convection is caused by the heat transfer interaction between a single wall and a very large fluid reservoir adjacent to the wall. The second type is the internal free convection which is confined within a channel or cavity. It is worthy to mention that the convective flow in which neither the free (natural) convection nor the forced convection effects are dominant and both modes are in a comparable level is known as combined or mixed convection [12, 52, 72, 84, 95]. Mixed convection in cavities is a topic of contemporary importance because cavities filled with

fluid are central components in a long list of engineering and geophysical systems. The flow and heat transfer induced in a cavity differs fundamentally from the external mixed convection boundary layer. Mixed convection in a cavity unlike the external mixed convection boundary layer that is caused by the heat transfer interaction between a single wall and a very large fluid reservoir is the result of the complex interaction between finite size fluid systems in thermal communication with all the walls that confine it. The complexity of this internal interaction is responsible for the diversity of flows that can exist inside the cavity. The phenomenon of mixed convection in cavities is varied by the geometry and the orientation of the cavity. Judging by the potential engineering applications, the cavity phenomenon can loosely be organized into two classes which are (i) vented cavity and (ii) lid-driven cavity. In a vented cavity, the interaction between the external forced stream provided by the inlet and the buoyancy driven flows induced by the heat source leads to the possibility of complex flows. Therefore, it is important to understand the fluid flow and heat transfer characteristics of mixed convection in a vented cavity. On the other hand, the fluid flow and heat transfer in a lid-driven cavity where the flow is induced by a shear force resulting from the motion of a lid combined with the buoyancy force due to non-homogeneous temperature of the cavity walls, provides another problem which is studied extensively by researchers to understand the interaction between buoyancy and shearing forces in such flow situation. The interaction between buoyancy driven and shear driven flows inside a closed cavity in a mixed convection regime is quite complex. Therefore, it is also important to understand the fluid flow and heat transfer characteristics of mixed convection in a lid-driven cavity.

1.3 Magnetohydrodynamics

A solid or fluid material moving in a magnetic field experiences an electromotive force. If the material is electrically conducting and a current path is available, electric current is ensured. The consequence is that an electromagnetic force due to the interaction of currents and field appears, perturbing the original motion. Therefore, magneto-hydrodynamics (MHD) is the science of the motion of electrically conducting fluids under the influence of applied magnetic forces. The word magnetohydrodynamics (MHD) include the terms magneto (magnetic field), hydro (water) and dynamics (movement). The field of MHD was developed by Hannes Alfven and he received the Nobel Prize in Physics for this in 1970. Examples of electrically conducting fluid are liquid metals such as mercury, liquid sodium, plasma (hot ionized gas containing free electrons and ions), etc. The symbiotic interaction between the fluid velocity field and

the electromagnetic forces gives rise to a flow scenario; the magnetic field affects the motion. Indeed MHD, like the low frequency electro-technology that developed in the later nineteenth century, is entirely pre-Maxwellian in spirit. Nevertheless MHD is usually regarded as a very contemporary subject. Applications of MHD are electromagnetic pump, the MHD generator using ionized gas as an armature, electro magnetic pumping of liquid metal coolants in nuclear reactors, stirring and levitation (to avoid contamination) in the metallurgical industries. Controlled thermonuclear fusion by confining hot ionized deuterium away from all walls by MHD forces led to intensive research on this branch of MHD and the related topic of plasma physics. One of the novelties of MHD is that a gas can have a free surface, not constrained by a rigid wall and prone to waves and instability. A related application is the use of MHD acceleration to shoot plasma into fusion devices or to produce high energy wind tunnels for simulating hypersonic flight. Other potential applications for MHD include electromagnets with fluid conductors, various energy conversion or storage devices, magnetically controlled lubrication by conducting fluids etc. The effect of electrical conductivity of the fluid and presence of magnetic field are: First, the motion of electrically conducting fluid across the magnetic lines of force generates currents according to Faraday's law of induction. This induced current according to Ampere's law gives rise to a second induced magnetic field. This induced magnetic field contributes to some change in the existing magnetic field. Second, the combined magnetic field interacts with the induced current density to produce a Lorentz force on the conductor.

1.4 Objectives

The main objective of the present thesis is to develop a HOC scheme on non-orthogonal curvilinear grids for linear, nonlinear convection-diffusion-reaction equations having non-homogeneous derivative source terms and with special emphasis to incompressible viscous flows governed by Navier-Stokes equations. Another objective is to examine the possibility of broadening the scope of applicability of HOC algorithms to heat transfer and magnetohydrodynamic problems. This scheme is capable of handling problems with complicated geometries with ease.

1.5 Motivation and thesis contribution

It is well-known that Navier-Stokes equations play an important role in several scientific and engineering fields. A small number of exact solutions of these equations are found. So, the required information by engineers/scientists can be provided only through numerical computations of these equations. In this study, the computational techniques

proposed are finite difference methods, the most widely used technique for engineering design and analysis. Despite significant progress in computational sciences, challenges persist in the accurate numerical simulation of a broad spectrum of dynamics such as fluid-structure interactions and technical applications such as solidification of castings, crude oil productions, geothermal reservoirs, grain storage etc. To resolve these complex flow phenomena more accurately, higher order accuracy of schemes are recommended. In addition to this, the fluid domain may not only contain several high gradient regions and boundary layers but also curvilinear boundaries. To resolve such flow phenomena accurately, non-uniform and non-orthogonal curvilinear grids could be of great help. This is where the motivation to develop HOC schemes on non-orthogonal curvilinear grids comes from, that can be used in irregular geometries with non-orthogonal curvilinear grid settings.

The present work is mainly concerned with the development of HOC finite difference schemes (time independent and time dependent) and application on non-uniform and non-orthogonal curvilinear grids. In addition, the robustness of these schemes are checked when applied in complex geometries.

The first work proposes a time independent HOC scheme that works equally efficiently on problems described on both rectangular as well as curvilinear domains. The scheme can be applied to steady-state convection-diffusion, reaction-diffusion, and convection-reaction-diffusion equations having mixed derivative as well as non-homogeneous source terms, and it can also be used to solve equations of N-S type with slight adjustment of the convection coefficients. It is fourth order accurate in space and can handle Dirichlet, Neumann and Robin type boundary conditions with ease. To validate the proposed scheme, it is first applied to problems having analytical solutions on non-uniform grids. Subsequently, it is applied to the lid driven cavity problem with bottom wavy wall on non-orthogonal grids and finally to the lid driven vase-shaped cavity problem using non-orthogonal curvilinear grids.

In the second work, an extension of the proposed HOC scheme to a transient one is made. It is implicit and of second order accurate in time and fourth order accurate in space. It handles Dirichlet, Neumann and Robin type boundary conditions with ease. Numerical results for the transient solutions of the fluid flow in the lid-driven cavity with the same geometries used as in the first work and their temporal variations are presented and discussed.

The third work deals with the numerical solutions of a natural convection problem in a both sided (left and right) wavy wall cavity with and without porous medium in presence of a magnetic field. For the problem without porous medium, two different

thermal boundary conditions (as two cases) are used. Case I: the bottom wall is heated while the two vertical walls are cold and the top wall is adiabatic. Case II: the bottom wall is heated, the top wall is cold and the left and right vertical walls are adiabatic. In the event of heated bottom wall, both uniform and non-uniform heating situations are considered. Numerical results are presented for variation of Prandtl number (Pr), Rayleigh number (Ra) and Hartmann number(Ha). In the case of porous medium the thermal boundary conditions are assumed to be the same as those of Case I, the computed results are discussed by varying the values of different parameters Pr, Ha and Darcy number (Da).

In the fourth work, a mixed convection problem in trapezoidal cavity is considered with the intuition that this type of geometry enhances the heat transfer rate. In this problem the bottom wall is heated, the two inclined sidewalls are cold while the extended moving top wall is adiabatic. First, the lid driven problem in a trapezoidal cavity has been solved for comparison with the results obtained by Mcquain [54]. Then numerical results are presented for mixed convection flow for different Grashof numbers (Gr) and Richardson numbers (Ri).

In the fifth work, flow in a rectangular vented cavity is studied. First, the results of a rectangular vented cavity problem are compared with those studied in [81] where the inlet is at the bottom portion of the left wall and the outlet is at the top portion of the right wall. Then the mixed convection results for the rectangular cavity with bottom wavy wall with the variation of Richardson number (Ri) and Reynolds number (Re) are computed and discussed.

In the final work, magnetohydrodynamic flow in a dilated channel is studied. A Hartmann profile is imposed at the inlet of the dilated channel, no-slip boundary conditions are used at bottom and top walls whereas at the outlet, a fully developed boundary condition is adopted. Streamline contours are presented for various Re to describe the flow phenomenon in the channel.

In case of the discretization of the Neumann boundary condition, one sided second order accurate finite difference approximation inside the flow region is considered.

The computed numerical results on a coarse grid are compared with both analytical and the established numerical results available in the literature, and excellent agreement is found in all the cases. It is to be noted that all of the computations were carried out on a Core i5 processor based PC.

1.6 Organization of the work

This thesis is organized in seven chapters. Chapter 1 contains the introduction of the thesis. In Chapter 2, an improved version of the higher order compact (HOC) finite difference scheme is proposed which is applicable on non-orthogonal curvilinear grid. Both the time independent and time dependent forms are discussed. Chapter 3 describes natural convection in presence of magnetic field in a wavy cavity with and without porous medium. In Chapter 4, mixed convection in a trapezoidal cavity is studied. Chapter 5 deals with the study of mixed convection in a vented wavy cavity. Magnetohydrodynamic flow in a dilated channel is discussed in Chapter 6. In Chapter 7, conclusions of the thesis work and future directions are presented.

भारतीय प्रौद्योगिकी संस्थान गुवाहाटी
Indian Institute of Technology Guwahati

2

Higher order compact schemes on non-uniform grids

This chapter contains the formulation of a higher order compact (HOC) scheme in cartesian coordinate systems with non-uniform and non-orthogonal curvilinear grids on complex geometries to solve two dimensional (2D) general second order partial differential equation having nonhomogeneous derivative source terms. The scheme is of fourth order accurate in space and second order accurate in time.

2.1 Introduction

During the last few decades, the development of numerical schemes for solving incompressible viscous flows achieved a great success in the field of computational fluid dynamics (CFD). But most of the schemes were either first or second order accurate in space. Since the order of accuracy of these schemes are 1 or 2, these schemes can not produce highly accurate results unless the mesh used in these schemes are fine enough. Moreover, if higher order scheme is used with large stencil, the bandwidth of the resulting matrix obtained from the scheme becomes larger which will not be computationally very efficient. For this reason, HOC schemes are preferable. Since the schemes are high order accurate, the grid length need not be very small, and due to compactness property, the stencil does not contain many points. Various variants of HOC schemes are available in the literature.

The approach for discretization of the equation considered here involves the nodal values of the variable along with the first derivative of the variable itself at a few nodal points. The first derivatives are discretized using Padé approximation. Idea of the use of derivatives of the variable along with the variable itself in the process of discretization is available in the works of Gupta, Manohar and Stephenson [23, 101]. Similar idea in deriving higher order mixed methods for elliptic PDE was used by Carey and Spotz [10].

The scheme considered here was initially proposed by Sen [90] but no analysis on its

strength and robustness was made. The scheme is generalized in this thesis by adding more number of terms in the source function by including the effects of heat transfer and magnetism, and the scheme is applied to various complex problems in order to study its strength and robustness. The governing equations considered to study in this thesis are second order partial differential equations having mixed derivative and source terms involving derivatives. For a problem with complex geometries having non-uniform curvilinear grid, transformation is used to solve the problem on a uniform grid. Lid driven cavity problems are solved in a square cavity with wavy wall and also in a vase-shaped geometry. A detailed discussion of the scheme in the transformed plane is presented in this chapter and successful applications of this scheme on non-uniform curvilinear grids are also demonstrated.

2.2 Mathematical Formulations and Discretization Procedure

2.2.1 Governing Equations

A general second order partial differential equation for a transport variable $\phi(x, y)$ defined in some continuous domain $\Omega \subset \mathbb{R}^2$ with nonhomogeneous derivative source terms and suitable boundary conditions on the boundary $\partial\Omega$ can be written as

$$\left.\begin{aligned} a\frac{\partial^2\phi}{\partial x^2} + g\frac{\partial^2\phi}{\partial x\partial y} + b\frac{\partial^2\phi}{\partial y^2} + c\frac{\partial\phi}{\partial x} + d\frac{\partial\phi}{\partial y} + r\phi = \chi + l_1\frac{\partial\epsilon_1}{\partial x} + l_2\frac{\partial\epsilon_1}{\partial y} \quad + l_3\frac{\partial\epsilon_2}{\partial x} + l_4\frac{\partial\epsilon_2}{\partial y}, \\ (x, y) \in \Omega, \\ \alpha_1(x, y)\phi + \alpha_2(x, y)\frac{\partial\phi}{\partial\bar{n}} = \alpha_3(x, y), \qquad (x, y) \in \partial\Omega, \end{aligned}\right\} \tag{2.1}$$

where a, b are diffusion coefficients, c and d are the convection coefficients, g is the coefficient in mixed derivative term, r is the coefficient in reaction term and right hand side of (2.1) are the source terms (it may include the derivative terms also which appear in the governing equations of heat transfer problems or magnetohydrodynamic problems). $\alpha_1(x, y)$, $\alpha_2(x, y)$ and $\alpha_3(x, y)$ are arbitrary coefficients used while describing Dirichlet, Neumann, or Robin type boundary conditions. It is assumed here that the functions $\phi(x, y), \chi(x, y), \epsilon_1(x, y), \epsilon_2(x, y)$, together with the coefficients $a, b, c, d, g, r, \alpha_1, \alpha_2, \alpha_3$, which are also functions of (x, y), are sufficiently smooth and l_1, l_2, l_3, l_4 are constants. The domain over which the aforementioned equation (2.1) may have curvilinear boundaries with non-orthogonal and non-uniform grid spacing is of our interest in this study. This

can be addressed efficiently by mapping the curvilinear non-uniform grid (x, y) in the physical domain to a transformed orthogonal uniform (ξ, η) computational grid, which is briefly discussed in the following subsection. The transformed equations now contain the transformation metrics which complicate the mathematical expressions in HOC methodology but the presence of analytical transformation function allows to obtain exact expression for the metrics.

2.2.2 Transformation of the equation:

In order to solve the fluid flow problem in geometries beyond rectangular, a transformation from the physical xy- plane to the computational $\xi\eta$- plane which is used to convert a complicated grid into a simple, uniform Cartesian grid is used. If the transformation is

$$x = x(\xi, \eta), y = y(\xi, \eta), \tag{2.2}$$

then the governing equation becomes

$$a_1 \frac{\partial^2 \hat{\phi}}{\partial \xi^2} + b_1 \frac{\partial^2 \hat{\phi}}{\partial \eta^2} + g_1 \frac{\partial^2 \hat{\phi}}{\partial \xi \partial \eta} + c_1 \frac{\partial \hat{\phi}}{\partial \xi} + d_1 \frac{\partial \hat{\phi}}{\partial \eta} + r_1 \hat{\phi} = f_1, \tag{2.3}$$

where

$$\begin{aligned}
a_1(\xi,\eta) &= \frac{a y_\eta^2 + b x_\eta^2 - g x_\eta y_\eta}{J^2}, \\
b_1(\xi,\eta) &= \frac{a y_\xi^2 + b x_\xi^2 - g x_\xi y_\xi}{J^2}, \\
g_1(\xi,\eta) &= \frac{-2a y_\xi y_\eta - 2b x_\xi x_\eta + g(x_\xi y_\eta + x_\eta y_\xi)}{J^2}, \\
c_1(\xi,\eta) &= \frac{c y_\eta - d x_\eta}{J} + \frac{a(y_\eta y_{\xi\eta} - y_\xi y_{\eta\eta}) + b(x_\eta x_{\xi\eta} - x_\xi x_{\eta\eta}) + g(y_\xi x_{\eta\eta} - y_\eta x_{\xi\eta})}{J^2} \\
&+ \frac{a(y_\xi y_\eta J_\eta - y_\eta^2 J_\xi) + b(x_\xi x_\eta J_\eta - x_\eta^2 J_\xi) + g(x_\eta y_\eta J_\xi - x_\eta y_\xi J_\eta)}{J^3}, \\
d_1(\xi,\eta) &= \frac{-c y_\xi + d x_\xi}{J} + \frac{a(y_\xi y_{\xi\eta} - y_\eta y_{\xi\xi}) + b(x_\xi x_{\xi\eta} - x_\eta x_{\xi\xi}) + g(y_\eta x_{\xi\xi} - y_\xi x_{\xi\eta})}{J^2} \\
&+ \frac{a(y_\xi y_\eta J_\xi - y_\xi^2 J_\eta) + b(x_\xi x_\eta J_\xi - x_\xi^2 J_\eta) + g(x_\xi y_\xi J_\eta - x_\xi y_\eta J_\xi)}{J^3}, \\
r_1(\xi,\eta) &= r(x,y), \\
f_1(\xi,\eta) &= \widehat{\chi} + \left(\frac{l_1 y_\eta - l_2 x_\eta}{J}\right)\frac{\partial \widehat{\epsilon_1}}{\partial \xi} + \left(\frac{-l_1 y_\xi + l_2 x_\xi}{J}\right)\frac{\partial \widehat{\epsilon_1}}{\partial \eta} \\
&+ \left(\frac{l_3 y_\eta - l_4 x_\eta}{J}\right)\frac{\partial \widehat{\epsilon_2}}{\partial \xi} + \left(\frac{-l_3 y_\xi + l_4 x_\xi}{J}\right)\frac{\partial \widehat{\epsilon_2}}{\partial \eta},
\end{aligned}$$

with $J = x_\xi y_\eta - x_\eta y_\xi \neq 0$.
The boundary condition becomes
$\hat{\alpha_1}(\xi,\eta)\hat{\phi} + \hat{\alpha_2}(\xi,\eta)(\hat{\phi}_\xi \xi_{\bar{n}} + \hat{\phi}_\eta \eta_{\bar{n}}) = \hat{\alpha_3}(\xi,\eta),\ (\xi,\eta) \in \partial\hat{\Omega}$,
where $\partial\hat{\Omega}$ is the boundary of the domain $(\hat{\Omega})$ in the computational plane, $\bar{n}$ is the normal to the boundary $\partial\hat{\Omega}$.

2.2.3 Discretization of the equation

The equation (2.3) can be written in the form

$$a_1\hat{\phi}_{\xi\xi} + b_1\hat{\phi}_{\eta\eta} + g_1\hat{\phi}_{\xi\eta} + c_1\hat{\phi}_\xi + d_1\hat{\phi}_\eta + r_1\hat{\phi} = f_1, \tag{2.4}$$

For convenience hat sign ˆ is omitted now onwards. We denote δ_ξ, δ_ξ^2, δ_η, δ_η^2 and $\delta_\xi\delta_\eta$ by the approximations

$$\begin{aligned}
\delta_\xi\phi_{i,j} &= \frac{1}{2h}(\phi_{i+1,j} - \phi_{i-1,j}),\\
\delta_\xi^2\phi_{i,j} &= \frac{1}{h^2}(\phi_{i+1,j} - 2\phi_{i,j} + \phi_{i-1,j}),\\
\delta_\eta\phi_{i,j} &= \frac{1}{2k}(\phi_{i,j+1} - \phi_{i,j-1}),\\
\delta_\eta^2\phi_{i,j} &= \frac{1}{k^2}(\phi_{i,j+1} - 2\phi_{i,j} + \phi_{i,j-1}),\\
\delta_\xi\delta_\eta\phi_{i,j} &= \frac{1}{4hk}(\phi_{i+1,j+1} - \phi_{i+1,j-1} - \phi_{i-1,j+1} + \phi_{i-1,j-1}),
\end{aligned}$$

where $\phi_{i,j}$ is the value of ϕ at the (i,j)-th point in the discretized domain, h and k are the uniform rectangular mesh steps constructed in the ξ- and η-directions respectively. Now using Taylor expansion at (i,j)-th point, we have

$$\phi_{\xi\xi} = \delta_\xi^2\phi - \frac{h^2}{12}\phi_{\xi\xi\xi\xi} + O(h^4) \tag{2.5}$$

and

$$\phi_\xi = \delta_\xi\phi - \frac{h^2}{6}\phi_{\xi\xi\xi} + O(h^4). \tag{2.6}$$

From the above equations, it is seen that in equation (2.5), $\phi_{\xi\xi}$ can be approximated to $O(h^4)$ if second order approximation for $\phi_{\xi\xi\xi\xi}$ is used. But to use compact finite difference scheme, first derivative of the variable is also used instead of the variable only.

From equation (2.6), we can write

$$\phi_{\xi\xi} = \delta_\xi\phi_\xi - \frac{h^2}{6}\phi_{\xi\xi\xi\xi} + O(h^4). \tag{2.7}$$

Now from equations (2.5) and (2.7), it can be written that

$$\phi_{\xi\xi} = 2\delta_\xi^2\phi - \delta_\xi\phi_\xi + O(h^4). \tag{2.8}$$

Now the first order derivative is approximated by using the Padé approximation:

$$\phi_\xi = \delta_\xi\phi - \frac{h^2}{6}\delta_\xi^2\phi_\xi + O(h^4). \tag{2.9}$$

Similarly, $\phi_{\eta\eta}$ can be written as

$$\phi_{\eta\eta} = 2\delta_\eta^2\phi - \delta_\eta\phi_\eta + O(k^4), \tag{2.10}$$

where ϕ_η can be approximated using the Padé approximation as

$$\phi_\eta = \delta_\eta\phi - \frac{k^2}{6}\delta_\eta^2\phi_\eta + O(k^4). \tag{2.11}$$

Now, the mixed derivative $\phi_{\xi\eta}$, is approximated as

$$\phi_{\xi\eta} = \delta_\xi\phi_\eta + \delta_\eta\phi_\xi - \delta_\xi\delta_\eta\phi + O(h^4, k^4). \tag{2.12}$$

To obtain a fourth order spatial compact formulation for (2.4), each of the derivatives is compactly approximated to $O(h^4, k^4)$. At the (i, j)-th node, the 4-th (fourth) order spatial approximation of the equation (2.4) can be written as

$$\begin{aligned} a_1\left(2\delta_\xi^2\phi_{i,j} - \delta_\xi\phi_{\xi_{i,j}}\right) + b_1\left(2\delta_\eta^2\phi_{i,j} - \delta_\eta\phi_{\eta_{i,j}}\right) \quad + \\ g_1\left(\delta_\xi\phi_{\eta_{i,j}} + \delta_\eta\phi_{\xi_{i,j}} - \delta_\xi\delta_\eta\phi_{i,j}\right) + c_1\phi_{\xi_{i,j}} + d_1\phi_{\eta_{i,j}} + r_1\phi_{i,j} \quad = \quad f_{1i,j}. \end{aligned} \tag{2.13}$$

The above equations can be written in the form

$$\sum_{s_1=-1}^{1}\sum_{s_2=-1}^{1} w_{i+s_1,j+s_2}\phi_{i+s_1,j+s_2} = F_{i,j}, \tag{2.14}$$

where

$$\begin{aligned} w_{i+1,j+1} &= -\frac{g_1}{4hk}, & w_{i+1,j} &= \frac{2a_1}{h^2}, & w_{i+1,j-1} &= \frac{g_1}{4hk}, \\ w_{i,j+1} &= \frac{2b_1}{k^2}, & w_{i,j} &= -(\frac{4a_1}{h^2} + \frac{4b_1}{k^2}) + r_1, & w_{i,j-1} &= \frac{2b_1}{k^2}, \\ w_{i-1,j+1} &= \frac{g_1}{4hk}, & w_{i-1,j} &= \frac{2a_1}{h^2}, & w_{i-1,j-1} &= -\frac{g_1}{4hk}, \end{aligned}$$

and

$$\begin{aligned} F_{i,j} &= f_{1i,j} + (\frac{a_1}{2h}\phi_{\xi i+1,j} - c_1\phi_{\xi i,j} - \frac{a_1}{2h}\phi_{\xi i-1,j} - \frac{g_1}{2k}\phi_{\xi i,j+1} + \frac{g_1}{2k}\phi_{\xi i,j-1} \\ &- \frac{g_1}{2h}\phi_{\eta i+1,j} + \frac{g_1}{2h}\phi_{\eta i-1,j} - d_1\phi_{\eta i,j} + \frac{b_1}{2k}\phi_{\eta i,j+1} - \frac{b_1}{2k}\phi_{\eta i,j-1}). \end{aligned}$$

2.3 Solutions of algebraic systems

The system of equations (2.14) can be written in matrix form as

$$A\Phi = F \tag{2.15}$$

where the coefficient matrix A is considered to be an asymmetric sparse matrix due to the proposed transformation. For a grid of size $m_1 \times m_2$, A is of size $m_1 m_2 \times m_1 m_2$ and Φ and F are $m_1 m_2$ component vectors.

To solve the algebraic system of equations (2.14), biconjugate gradient stabilized method (BiCGSTAB) is applied. Since the matrix is sparse, the iterative method is preferable rather than any direct method. The coefficient matrix A is not generally diagonally dominant, so the conventional iterative method such as Gauss-Seidel, SOR can not be used. On uniform grid, the associated matrices may be symmetric and positive definite, where conjugate-gradient (CG) algorithm can be used. Since the scheme is related to non-uniform grid, the matrix A associated with this scheme is generally non-symmetric. So, biconjugate gradient stabilized method (BiCGSTAB) without preconditioning is used to solve the system of equations.

2.4 Numerical test cases

2.4.1 Comparison with analytic solutions

To test the high order accuracy of the scheme and to compare the numerical solutions obtained using the scheme with analytic solutions, two test problems are considered as follows:

Test Problem I:

For the test problem I, the equation is of the form (2.1) with the following coefficients:

$$\begin{aligned} a(x,y) &= -1, & b(x,y) &= -1, \\ c(x,y) &= -Re\ x, & d(x,y) &= Re\ y, \\ g(x,y) &= (1-x)(1-y)e^{x+y}, & r(x,y) &= 0, \end{aligned}$$

on a unit square with the Dirichlet boundary conditions using uniform grid length h along x- and y- directions.

$$\begin{aligned} \phi(x,0) &= 0, & 0 \le x \le 1, \\ \phi(x,1) &= x(1+x^2), & 0 \le x \le 1, \\ \phi(0,y) &= 0, & 0 \le y \le 1, \\ \phi(1,y) &= y(1+y^2), & 0 \le y \le 1. \end{aligned}$$

The exact solution of this problem is

$$\phi_{ex} = xy(x^2 + y^2).$$

For this problem, no transformation is taken. The problem is solved in uniform cartesian grid.

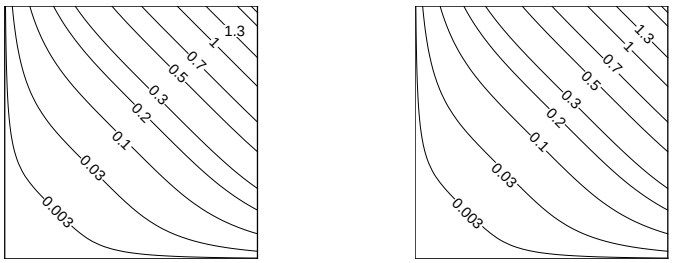

Figure 2.1: Test problem I: The left side is exact and the right side is numerical.

Fig 2.1, reveals a comparison between the exact and numerical solutions graphically for $Re = 100$ with grid size 41×41. This figure shows the perfect match of the numerical solution with the exact solution.

Test Problem II:

For the test problem II, the equation is of the form (2.1) with the coefficients as follows:

$$a(x,y) = -1, \qquad b(x,y) = -1,$$
$$c(x,y) = -Re\ (1-x)(1-2y), \qquad d(x,y) = 4xyRe\ (1-y),$$
$$g(x,y) = \cos(\pi x)\sin(\pi y), \qquad r(x,y) = 0,$$

on a unit square with the boundary conditions

$$\begin{aligned} \phi(x,0) &= \sin(\pi x), & 0 \le x \le 1,\\ \phi(x,1) &= \sin(\pi x), & 0 \le x \le 1,\\ \phi(0,y) &= \sin(\pi y), & 0 \le y \le 1,\\ \phi(1,y) &= \sin(\pi y), & 0 \le y \le 1. \end{aligned}$$

The exact solution of this problem is

$$\phi_{ex} = \sin(\pi x) + \sin(\pi y) + \sin(\pi x)\sin(\pi y).$$

For this problem, non-uniform grid is considered for the physical plane and a transformation is applied to transform it into a uniform cartesian one. The transformation considered here is

$$x = \xi + \frac{\lambda}{2\pi}\sin 2\pi\xi,$$
$$y = \eta + \frac{\lambda}{2\pi}\sin 2\pi\eta.$$

Fig 2.2 shows the non-uniform grids and the uniform grids for $\lambda = 0.2$ related to Problem II.

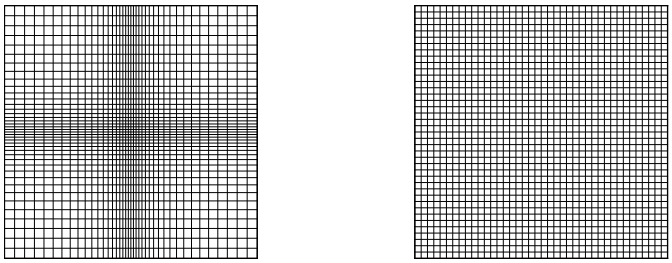

Figure 2.2: Non-uniform and uniform grid.

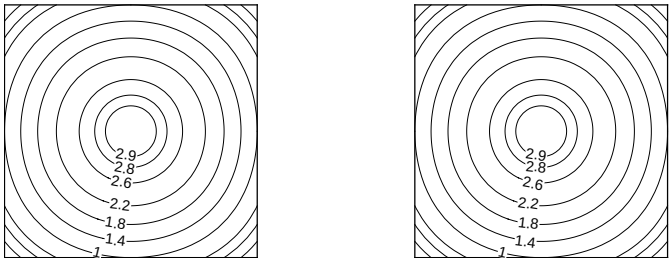

Figure 2.3: Test problem II: The left side is exact and the right side is numerical.

Fig 2.3, indicates the numerical solution and exact solution of problem II and the numerical results match with the exact solution perfectly for $Re = 100$ with grid size 41×41, which is clear from this figure.

Table 2.1 shows maximum errors in ϕ for $0 \leq Re \leq 100$ on different meshes, e.g. 21×21, 41×41 with different $\lambda = 0.2, 0.4$. The last column shows the estimated orders of accuracy (O(A)), which is calculated by the following formula

$$O(A) = \frac{ln(E_1/E_2)}{ln2}, \tag{2.16}$$

Table 2.1: *Problem 1: maximum absolute errors and convergence rates of ϕ for different Re ($0 \leq Re \leq 100$), stretching ratio λ ($\lambda = 0.2$, and 0.4), and mesh size (21×21 and 41×41).*

Re	λ	Maximum absolute errors		Rate
		21× 21	41× 41	
0.0	0.2	2.897018(-4)	2.024837(-5)	3.839
	0.4	6.334755(-4)	5.087878(-5)	3.638
10.0	0.2	3.035219(-4)	2.045013(-5)	3.892
	0.4	6.676944(-4)	5.112793(-5)	3.707
50.0	0.2	3.005237(-4)	2.038555(-5)	3.882
	0.4	6.621022(-4)	5.109302(-5)	3.696
100.0	0.2	2.982825(-4)	1.987872(-5)	3.907
	0.4	6.632180(-4)	5.008973(-5)	3.727

where

$E_1 = \phi - \phi_C$; $E_2 = \phi - \phi_F$.

Here ϕ, ϕ_C, ϕ_F respectively stand for exact solution, the solution on a coarse grid and the solution on a fine grid with double of the numbers of points in each direction. From Table 2.1, it can be seen that the order of accuracy of the scheme is close to 4.

From the above two tests cases it is ensured that the proposed HOC scheme is capable of producing correct and accurate results on a reasonable grid. Next, the following two problems having complex geometries are solved using the proposed scheme.

2.4.2 Lid-driven problem in wavy wall geometry

Problem I: Here, the lid driven cavity problem is solved in a square cavity with the wavy bottom wall. The geometry of the problem is shown in Fig 2.4.

The required transformation used for this geometry is

$$x = \xi \ ,$$

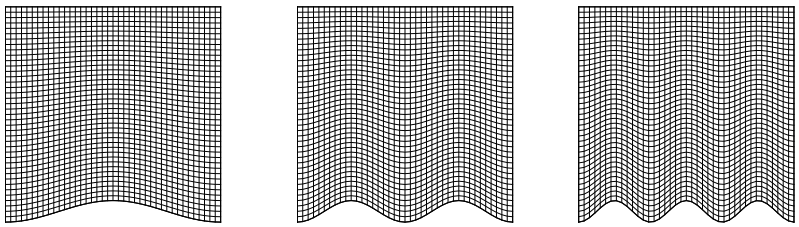

Figure 2.4: Geometry of the lid driven cavity problem

$$y = \eta + 0.05(1 - \cos 2\pi M\xi)(1 - \eta),$$

where the undulation of the geometry depends on the values of M. For case $M = 1$, it corresponds the first geometry (left side) in Fig 2.4 and $M = 2$ and $M = 3$ refer to the second and third geometry in Fig 2.4 respectively. No-slip boundary conditions are applied for all boundaries of the cavity except the top wall which is moving with a constant velocity.

The non-dimensional form of the governing equations to be solved are

$$\frac{\partial U}{\partial X} + \frac{\partial V}{\partial Y} = 0 \tag{2.17}$$

$$U\frac{\partial U}{\partial X} + V\frac{\partial U}{\partial Y} = -\frac{\partial P}{\partial X} + \frac{1}{Re}\left(\frac{\partial^2 U}{\partial X^2} + \frac{\partial^2 U}{\partial Y^2}\right), \tag{2.18}$$

$$U\frac{\partial V}{\partial X} + V\frac{\partial V}{\partial Y} = -\frac{\partial P}{\partial Y} + \frac{1}{Re}\left(\frac{\partial^2 V}{\partial X^2} + \frac{\partial^2 V}{\partial Y^2}\right), \tag{2.19}$$

where U and V are the velocity components along the X and Y directions respectively, Re is the Reynolds number, P is the pressure.

Stream-function ϕ and vorticity ζ are introduced as:

$$U = \frac{\partial \psi}{\partial Y}, V = -\frac{\partial \psi}{\partial Y} \tag{2.20}$$

and

$$\zeta = \frac{\partial V}{\partial X} - \frac{\partial U}{\partial Y}. \tag{2.21}$$

The stream-function and vorticity formulations of the governing equations can be written as:

$$-\frac{\partial^2 \psi}{\partial X^2} - \frac{\partial^2 \psi}{\partial Y^2} = \zeta, \tag{2.22}$$

$$-\frac{\partial^2 \zeta}{\partial X^2} - \frac{\partial^2 \zeta}{\partial Y^2} + URe\frac{\partial \zeta}{\partial X} + VRe\frac{\partial \zeta}{\partial Y} = 0. \tag{2.23}$$

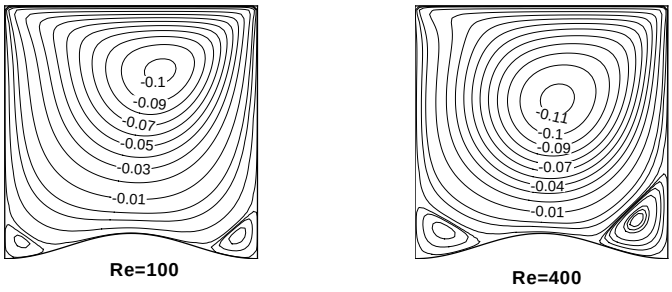

Figure 2.5: Streamline contour for Re=100 and 400.

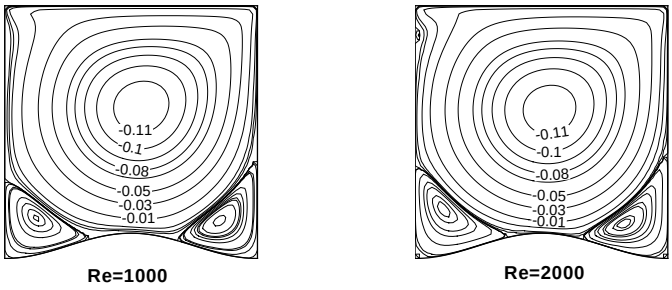

Figure 2.6: Streamline contour for Re=1000 and 2000.

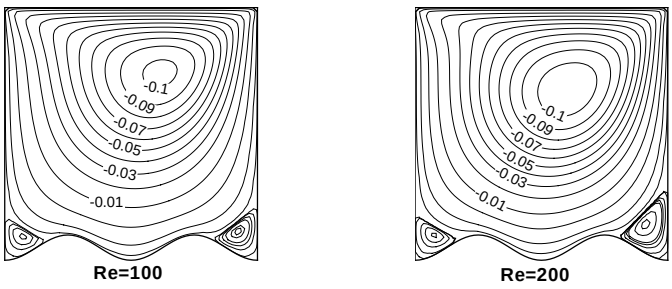

Figure 2.7: Streamline contour for Re=100 and 200.

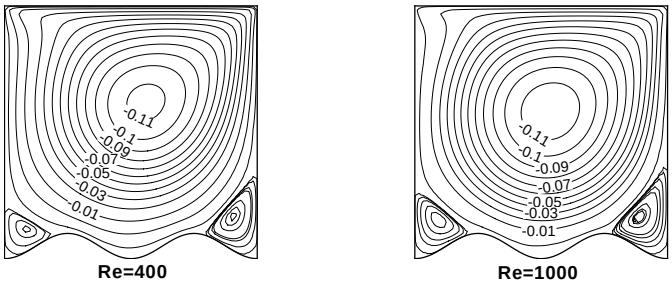

Figure 2.8: Streamline contour for Re=400 and 1000.

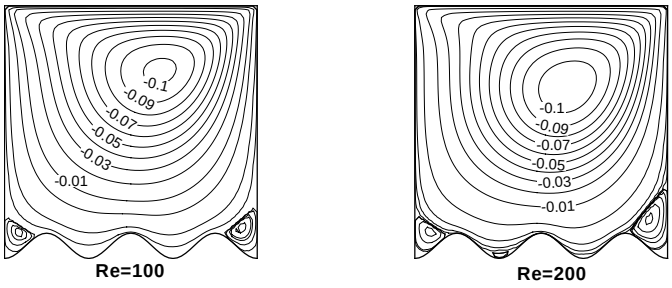

Figure 2.9: Streamline contour for Re=100 and 200.

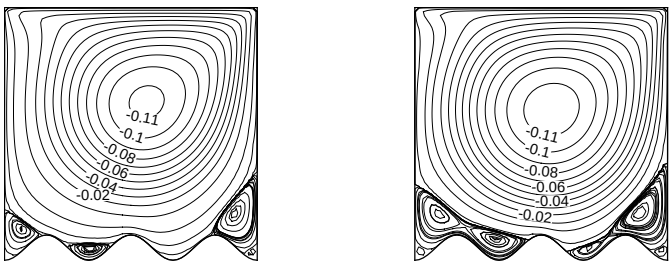

Figure 2.10: Streamline contour for Re=400 and 1000.

In Fig 2.5 and Fig 2.6, the streamline contours for Re=100, 400, 1000 and 2000 are plotted for $M = 1$. For $M = 2$, the streamline contours are shown in Fig 2.7 and Fig 2.8 and for $M = 3$, the streamline contours are presented in Fig 2.9 and Fig 2.10. From Figs 2.5 and 2.6, effects of the increase in Reynolds number are shown and it is seen that when $Re = 100$ and $M = 1$, there are two secondary vortices near the bottom corners of the wavy wall along with a primary vortex centered at a point near the upper wall. When $Re = 400$, the secondary vortices become larger in size and the primary vortex changes slightly its position towards the middle of the cavity. With the increase of Re to 2000, the size of the secondary vortices becomes even larger in size and the primary vortex is almost at the center of the cavity and one additional small vortex is found near the left top corner of the cavity. For $M = 2$ or 3, same kind of flow characteristics are exhibited with the increase of the Reynolds number Re. For $Re = 400$, it is seen that when $M = 1$, there are two secondary vortices with one primary vortex while when M increases to 3, there are three secondary vortices with the primary vortex.

The other problem considered here is having a geometry of vase-like cavity with a moving lid.

Problem 2: Lid-driven-cavity problem in one complicated geometry. The geometry of the problem is complicated (vase-like) as shown in Fig 2.11. The boundary conditions are same as those of the previous problem (i,e., lid driven cavity problem with wavy bottom wall).

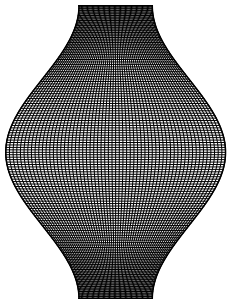

Figure 2.11: Vase-shaped-geometry.

The streamline contours for Re=100, 400,1000 and 2000 are shown in Fig 2.12 and Fig 2.13. From these figures, it is shown that in all the cases two vortices are there in the streamline contour, for $Re = 100$, the center of the secondary vortex is at the middle right side of the cavity. When Re increases to 200, the secondary vortex gets enlarged

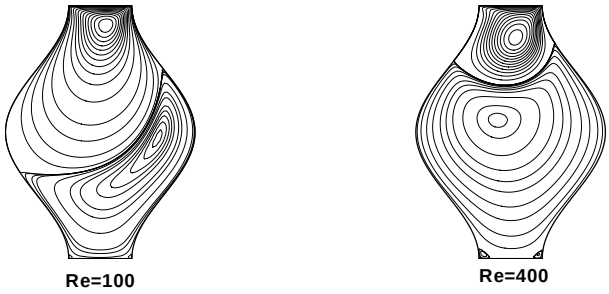

Figure 2.12: Streamline contour for Re=100 and 400.

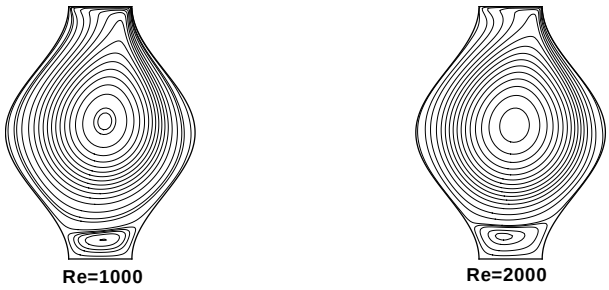

Figure 2.13: Streamline contour for Re=1000 and 2000.

and it moves towards the left side of the cavity. For $Re = 1000$, the primary vortex covers almost the entire part of the cavity and the secondary vortex becomes smaller in size and is pushed down at the bottom part of the enclosure. For $Re = 2000$, the secondary vortex becomes slightly larger than that in the case of $Re = 1000$.

2.5 Time dependent form of the scheme on non uniform grid

The general form of the time dependent convection-diffusion-reaction equation having mixed derivative on a domain $(0,\infty)\times\Omega$ with the boundary conditions on the boundary $\partial\Omega$ can be written as

$$l\frac{\partial\phi}{\partial t}+a\frac{\partial^2\phi}{\partial x^2}+b\frac{\partial^2\phi}{\partial y^2}+g\frac{\partial^2\phi}{\partial x\partial y}+c\frac{\partial\phi}{\partial x}+d\frac{\partial\phi}{\partial y}+r\phi=\chi+l_1\frac{\partial\epsilon_1}{\partial x}+l_2\frac{\partial\epsilon_1}{\partial y}+l_3\frac{\partial\epsilon_2}{\partial x}+l_4\frac{\partial\epsilon_2}{\partial y}, \quad (2.24)$$

with the initial condition

$$\phi(x,y,0)=\phi_0(x,y), \text{ in}\,\Omega \quad (2.25)$$

and boundary condition

$$\alpha_1(x,y,t)\phi+\alpha_2(x,y,t)\frac{\partial\phi}{\partial\bar{n}}=\alpha_3(x,y,t), \text{ on}\,\partial\Omega \quad (2.26)$$

where $\phi(x,y,t)$ is the unknown variable, l, l_1, l_2, l_3, l_4 are constants, $a<0$, $b<0$, g, c, d, r, χ, ϵ_1, ϵ_2 are sufficiently smooth functions of (x,y,t); $\alpha_1(x,y,t)$, $\alpha_2(x,y,t)$ and $\alpha_3(x,y,t)$ are arbitrary coefficients used for describing as Dirichlet, Neumann, or Robin type boundary conditions. It is noted that the set of time dependent Navier-Stokes equations is a particular case of (2.24).

2.5.1 Transformation of the equation:

In order to solve the fluid flow problem in geometry beyond rectangular, a transformation from the physical xy- plane to the computational $\xi\eta$- plane which is used to convert a complicated grid into a simple, uniform Cartesian grid is considered. The transformation can symbolically be written as,

$$x=x(\xi,\eta), y=y(\xi,\eta). \quad (2.27)$$

Under this transformation the equation becomes

$$l\frac{\partial\hat{\phi}}{\partial t}+a_1\frac{\partial^2\hat{\phi}}{\partial\xi^2}+b_1\frac{\partial^2\hat{\phi}}{\partial\eta^2}+g_1\frac{\partial^2\hat{\phi}}{\partial\xi\partial\eta}+c_1\frac{\partial\hat{\phi}}{\partial\xi}+d_1\frac{\partial\hat{\phi}}{\partial\eta}+r_1\hat{\phi}=f_1, \quad (2.28)$$

where

$$
\begin{aligned}
a_1(\xi,\eta) &= \frac{ay_\eta^2 + bx_\eta^2 - gx_\eta y_\eta}{J^2},\\
b_1(\xi,\eta) &= \frac{ay_\xi^2 + bx_\xi^2 - gx_\xi y_\xi}{J^2},\\
g_1(\xi,\eta) &= \frac{-2ay_\xi y_\eta - 2bx_\xi x_\eta + g(x_\xi y_\eta + x_\eta y_\xi)}{J^2},\\
c_1(\xi,\eta) &= \frac{cy_\eta - dx_\eta}{J} + \frac{a(y_\eta y_{\xi\eta} - y_\xi y_{\eta\eta}) + b(x_\eta x_{\xi\eta} - x_\xi x_{\eta\eta}) + g(y_\xi x_{\eta\eta} - y_\eta x_{\xi\eta})}{J^2}\\
&+ \frac{a(y_\xi y_\eta J_\eta - y_\eta^2 J_\xi) + b(x_\xi x_\eta J_\eta - x_\eta^2 J_\xi) + g(x_\eta y_\eta J_\xi - x_\eta y_\xi J_\eta)}{J^3},\\
d_1(\xi,\eta) &= \frac{-cy_\xi + dx_\xi}{J} + \frac{a(y_\xi y_{\xi\eta} - y_\eta y_{\xi\xi}) + b(x_\xi x_{\xi\eta} - x_\eta x_{\xi\xi}) + g(y_\eta x_{\xi\xi} - y_\xi x_{\xi\eta})}{J^2}\\
&+ \frac{a(y_\xi y_\eta J_\xi - y_\xi^2 J_\eta) + b(x_\xi x_\eta J_\xi - x_\xi^2 J_\eta) + g(x_\xi y_\xi J_\eta - x_\xi y_\eta J_\xi)}{J^3},\\
r_1(\xi,\eta) &= r(x,y),\\
f_1(\xi,\eta) &= \widehat{\chi} + \left(\frac{l_1 y_\eta - l_2 x_\eta}{J}\right)\frac{\partial\widehat{\epsilon_1}}{\partial\xi} + \left(\frac{-l_1 y_\xi + l_2 x_\xi}{J}\right)\frac{\partial\widehat{\epsilon_1}}{\partial\eta}\\
&+ \left(\frac{l_3 y_\eta - l_4 x_\eta}{J}\right)\frac{\partial\widehat{\epsilon_2}}{\partial\xi} + \left(\frac{-l_3 y_\xi + l_4 x_\xi}{J}\right)\frac{\partial\widehat{\epsilon_2}}{\partial\eta},
\end{aligned}
$$

with $J = x_\xi y_\eta - x_\eta y_\xi \neq 0$,
with the initial condition

$$\hat{\phi}(\xi,\eta,0) = \hat{\phi}_0(\xi,\eta), \text{ in } \hat{\Omega} \tag{2.29}$$

and boundary condition
$\hat{\alpha_1}(\xi,\eta,t)\hat{\phi} + \hat{\alpha_2}(\xi,\eta,t)(\hat{\phi}_\xi \xi_{\bar{n}} + \hat{\phi}_\eta \eta_{\bar{n}}) = \hat{\alpha_3}(\xi,\eta,t),\ (\xi,\eta,t) \text{ on } \partial\hat{\Omega}$,
where $\partial\hat{\Omega}$ is the boundary of the domain $(\hat{\Omega})$ in the computational plane, $\bar{n}$ is the normal to the boundary $\partial\hat{\Omega}$.

2.5.2 Discretization of the equation

At the (i,j)-th node, the 4-th order spatial approximation of equation (2.28) at the n-th time level, can be written as:

$$
\begin{aligned}
l\frac{\partial\phi}{\partial t}\Big|_{i,j}^{n} + a_1\left(2\delta_\xi^2\phi_{i,j}^n - \delta_\xi\phi_{\xi_{i,j}}^n\right) + b_1\left(2\delta_\eta^2\phi_{i,j}^n - \delta_\eta\phi_{\eta_{i,j}}^n\right) \quad + \qquad (2.30)\\
g_1\left(\delta_\xi\phi_{\eta_{i,j}}^n + \delta_\eta\phi_{\xi_{i,j}}^n - \delta_\xi\delta_\eta\phi_{i,j}^n\right) + c_1\phi_{\xi_{i,j}}^n + d_1\phi_{\eta_{i,j}}^n + r_1\phi_{i,j}^n \quad = \quad f_{1_{i,j}}^n,
\end{aligned}
$$

where hat sign ˆ is omitted for convenience, and the derivatives are approximated using the following formulae:

$$\phi_{\xi\xi_{i,j}} = 2\delta_\xi^2\phi_{i,j} - \delta_\xi\phi_{\xi_{i,j}} + O(h^4), \tag{2.31}$$

$$\phi_{\eta\eta_{i,j}} = 2\delta_\eta^2\phi_{i,j} - \delta_\eta\phi_{\eta_{i,j}} + O(k^4), \tag{2.32}$$

$$\phi_{\xi\eta_{i,j}} = \delta_\xi\phi_{\eta_{i,j}} + \delta_\eta\phi_{\xi_{i,j}} - \delta_\xi\delta_\eta\phi_{i,j} + O(h^4, k^4), \tag{2.33}$$

$$\phi_{\xi_{i,j}} = \delta_\xi\phi_{i,j} - \frac{h^2}{6}\delta_\xi^2\phi_{\xi_{i,j}} + O(k^4), \tag{2.34}$$

$$\phi_{\eta_{i,j}} = \delta_\eta\phi_{i,j} - \frac{k^2}{6}\delta_\eta^2\phi_{\eta_{i,j}} + O(k^4), \tag{2.35}$$

where

$$\delta_\xi\phi_{i,j} = \frac{1}{2h}(\phi_{i+1,j} - \phi_{i-1,j}),$$

$$\delta_\xi^2\phi_{i,j} = \frac{1}{h^2}(\phi_{i+1,j} - 2\phi_{i,j} + \phi_{i-1,j}),$$

$$\delta_\eta\phi_{i,j} = \frac{1}{2k}(\phi_{i,j+1} - \phi_{i,j-1}),$$

$$\delta_\eta^2\phi_{i,j} = \frac{1}{k^2}(\phi_{i,j+1} - 2\phi_{i,j} + \phi_{i,j-1}),$$

$$\delta_\xi\delta_\eta\phi_{i,j} = \frac{1}{4hk}(\phi_{i+1,j+1} - \phi_{i+1,j-1} - \phi_{i-1,j+1} + \phi_{i-1,j-1}).$$

For the approximation of time derivative term, let the time step length be denoted by Δt. Now a weighted average parameter μ is introduced through the approximation of the time derivative $\frac{\partial\phi}{\partial t}$ such that $t_\mu = \mu t^{(n+1)} + (1-\mu)t^{(n)}$ where $0 \le \mu \le 1$ ((n) and $(n+1)$ denote the n-th and $(n+1)$-th time level respectively). When $\mu = 0.5$, second order accuracy in time is obtained.

Now equation (2.31) can be expressed in the form as:

$$\begin{aligned}\sum_{s_1=-1}^{1}\sum_{s_2=-1}^{1} w_{i+s_1,j+s_2}\phi_{i+s_1,j+s_2}^{(n+1)} &= \sum_{s_1=-1}^{1}\sum_{s_2=-1}^{1} w'_{i+s_1,j+s_2}\phi_{i+s_1,j+s_2}^{(n)} \\ &+ \Delta t\left(\mu F_{i,j}^{(n+1)} + (1-\mu)F_{i,j}^{(n)}\right),\end{aligned} \tag{2.36}$$

where

$$\begin{aligned} w_{i+s_1,j+s_2} &= \mu\Delta t\, e_{i+s_1,j+s_2} + q_{i+s_1,j+s_2}\ , \\ w'_{i+s_1,j+s_2} &= (\mu-1)\Delta t\, e_{i+s_1,j+s_2} + q_{i+s_1,j+s_2}, \\ e_{i+1,j+1} &= -\tfrac{g_1}{4hk}, & q_{i+1,j+1} &= 0, \\ e_{i+1,j} &= \tfrac{2a_1}{h^2}, & q_{i+1,j} &= 0, \\ e_{i+1,j-1} &= \tfrac{g_1}{4hk}, & q_{i+1,j-1} &= 0, \end{aligned}$$

$$\begin{aligned} e_{i,j+1} &= \tfrac{2b_1}{k^2}, & q_{i,j+1} &= 0, \\ e_{i,j} &= -(\tfrac{4a_1}{h^2} + \tfrac{4b_1}{k^2}) + r_1, & q_{i,j} &= l, \\ e_{i,j-1} &= \tfrac{2b_1}{k^2}, & q_{i,j-1} &= 0, \\ e_{i-1,j+1} &= \tfrac{g_1}{4hk}, & q_{i-1,j+1} &= 0, \\ e_{i-1,j} &= \tfrac{2a_1}{h^2}, & q_{i-1,j} &= 0, \\ e_{i-1,j-1} &= -\tfrac{g_1}{4hk}, & q_{i-1,j-1} &= 0, \end{aligned}$$

and

$$\begin{aligned} F_{i,j} &= f_{1i,j} + (\frac{a_1}{2h}\phi_{\xi i+1,j} - c_1\phi_{\xi i,j} - \frac{a_1}{2h}\phi_{\xi i-1,j} - \frac{g_1}{2k}\phi_{\xi i,j+1} + \frac{g_1}{2k}\phi_{\xi i,j-1} \\ &- \frac{g_1}{2h}\phi_{\eta i+1,j} + \frac{g_1}{2h}\phi_{\eta i-1,j} - d_1\phi_{\eta i,j} + \frac{b_1}{2k}\phi_{\eta i,j+1} - \frac{b_1}{2k}\phi_{\eta i,j-1}). \end{aligned}$$

2.6 Stability of the Scheme

Throughout this thesis, the value of μ is considered as $\mu = 0.5$ for second order accuracy in time. For stability analysis, von Neumann stability analysis is performed for the proposed scheme (with constant coefficients) and the following conditions are obtained (as it is a standard procedure, the detailed calculations are not included):
When $\mu \geq 0.5$ and $\mid g \mid^2 \leq 4ab$:
the scheme is unconditionally stable for $r \geq 0$ and conditionally stable for $r < 0$ with the condition $\Delta t < -\dfrac{1}{\mu r}$.

2.6.1 Solutions of algebraic systems

The algebraic system of equations (2.36) can be written in the matrix form as:

$$A\mathbf{\Phi}^{n+1} = \mathbf{F}(\mathbf{\Phi}^n), \tag{2.37}$$

where the coefficient matrix A is an asymmetric sparse matrix. Here the steady-state solutions are defined through time marching process. The convergence criteria for time marching steady-state solutions is, for all the grid points,

$$\max|\Phi^{n+1} - \Phi^n| < Tol, \tag{2.38}$$

where Φ^{n+1} and Φ^n are solutions at $(n+1)$-th and n-th time step respectively, and Tol is the limit for convergence.

As the obtained matrix is a sparse matrix, so the biconjugate-gradient stabilized method without preconditioning is used to solve the system of equations.

2.6.2 Lid-driven problem in wavy wall geometry

Problem I: For Problem I, a lid driven square cavity problem with a bottom wavy wall is considered (the geometry is shown in Fig 2.14). No slip boundary conditions are applied for all the boundaries except at the top boundary. The top wall is moving with a constant velocity.

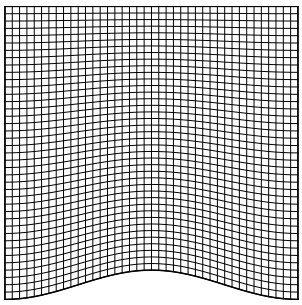

Figure 2.14: Bottom wavy cavity-geometry.

The chosen transformation for this problem is

$$x = \xi,$$
$$y = \eta + 0.05(1 - \cos 2\pi M\xi)(1 - \eta),$$

where the value of M is considered as 1 for this time dependent case.

The stream-function (ψ) and vorticity (ζ) formulations of the governing equations in non-dimensional form for time dependent case can be written as:

$$-\frac{\partial^2\psi}{\partial X^2} - \frac{\partial^2\psi}{\partial Y^2} = \zeta, \tag{2.39}$$

$$Re\frac{\partial\zeta}{\partial t} - \frac{\partial^2\zeta}{\partial X^2} - \frac{\partial^2\zeta}{\partial Y^2} + URe\frac{\partial\zeta}{\partial X} + VRe\frac{\partial\zeta}{\partial Y} = 0, \tag{2.40}$$

where U and V are the velocity components along the X and Y directions respectively, t is time, Re is the Reynolds number.

Figs 2.15-2.17 show the streamline contours for $Re = 100$ at different times. Initially, only a primary vortex is observed in the cavity and subsequently two secondary vortices along with the primary vortex appear at bottom corners of the cavity . With time, the secondary vortices get larger in size. Finally, at the steady state, there is one primary vortex along with two corner secondary vortices at the bottom of the cavity . For

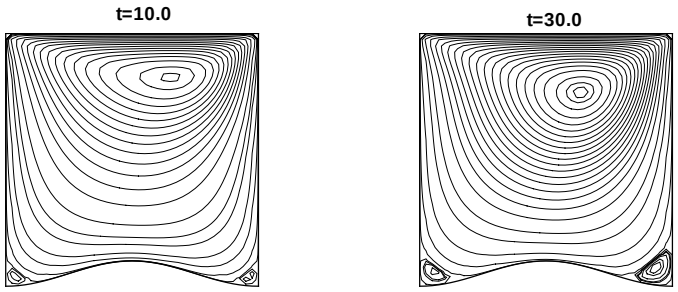

Figure 2.15: Streamline contour for Re=100 at different time

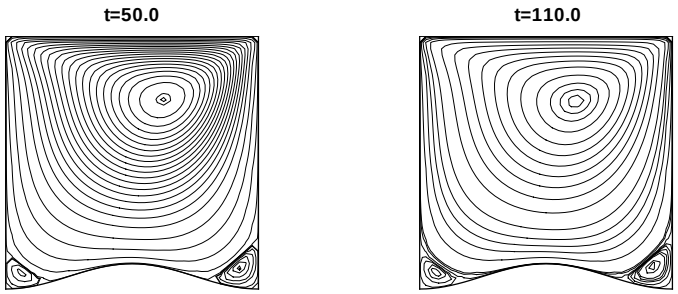

Figure 2.16: Streamline contour for Re=100 at different time

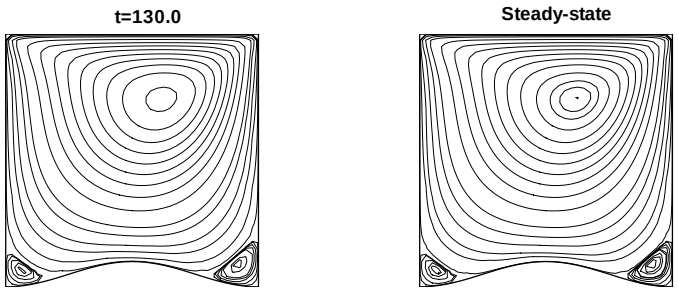

Figure 2.17: Streamline contour for Re=100 at different time

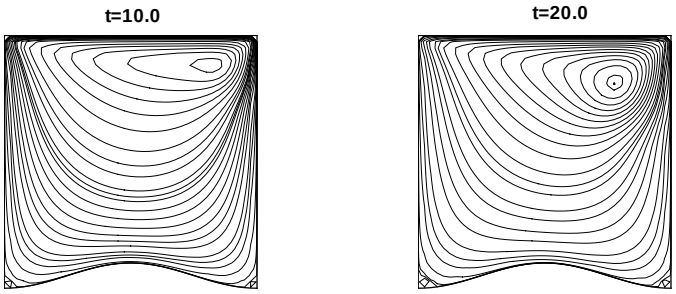

Figure 2.18: Streamline contour for Re=400 at different time

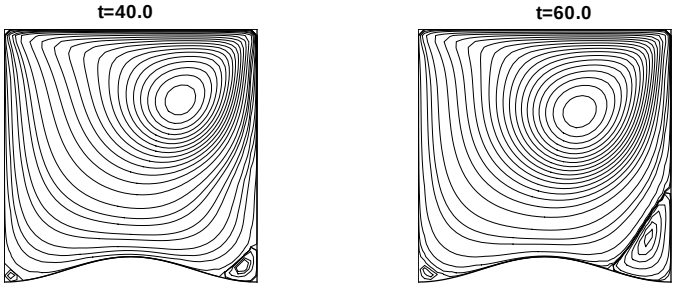

Figure 2.19: Streamline contour for Re=400 at different time

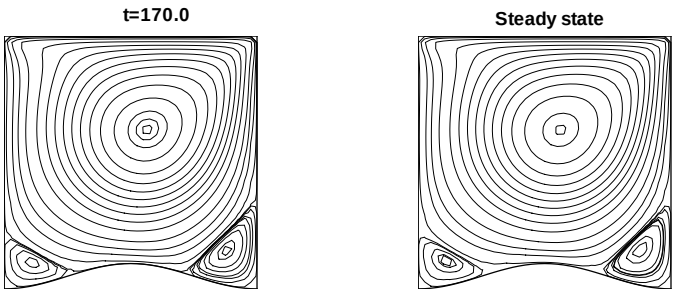

Figure 2.20: Streamline contour for Re=400 at different time

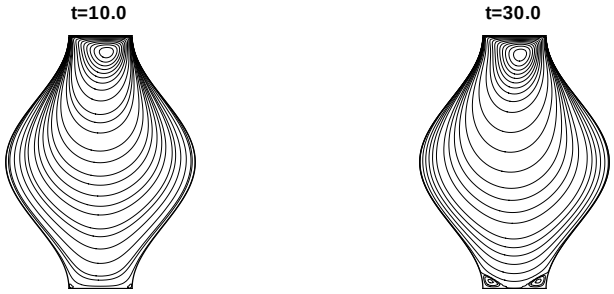

Figure 2.21: Streamline contour for Re=100 at different time

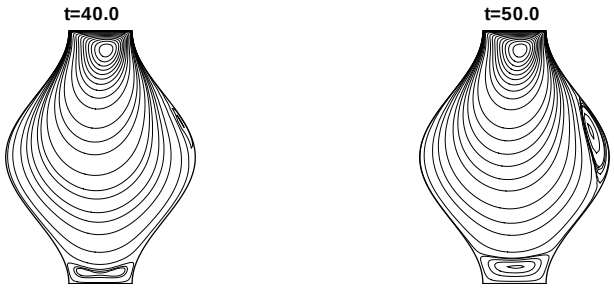

Figure 2.22: Streamline contour for Re=100 at different time

$Re = 400$, the streamline contours are presented at different time in the Figs (2.18)-(2.20). In this case, initially one vortex appears near the right top corner of the cavity. Then the vortex moves towards the center of the cavity. Like the previous case, two vortices appear at the bottom corners, the vortex at the right bottom corner is larger than the vortex at the left bottom corner. With time, both the secondary vortices get larger.

Problem II:

For problem II, another lid driven cavity (vase-shaped) problem is considered where the physical plane for this case is of curvilinear type. The geometry is shown in Fig 2.11 with grids. The associated boundary conditions are: at all the rigid walls, no-slip boundary conditions are applied whereas the top wall is moving with a constant velocity. The governing equations for this case in stream-function vorticity formulation are equations (2.39) and (2.40).

Figs 2.21-2.24 show the streamlines contours for $Re = 100$ at different time levels. At the initial stage there is one vortex near the top moving wall and subsequently two

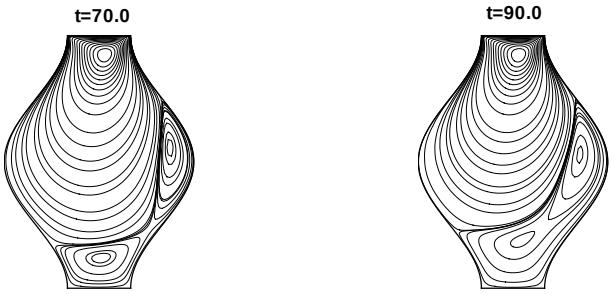

Figure 2.23: Streamline contour for Re=100 at different time

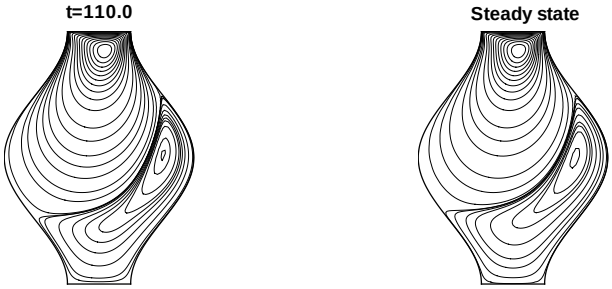

Figure 2.24: Streamline contour for Re=100 at different time

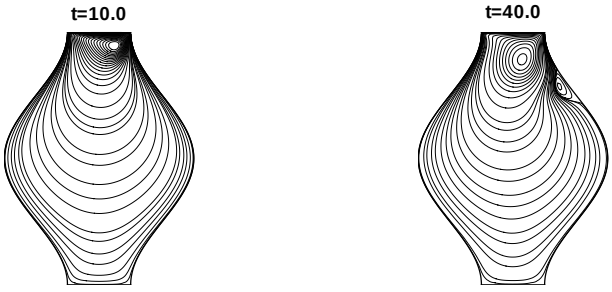

Figure 2.25: Streamline contour for Re=500 at different time

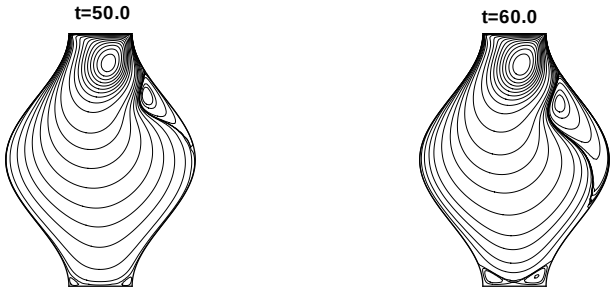

Figure 2.26: Streamline contour for Re=500 at different time

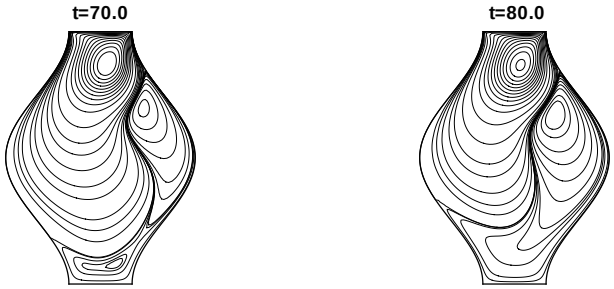

Figure 2.27: Streamline contour for Re=500 at different time

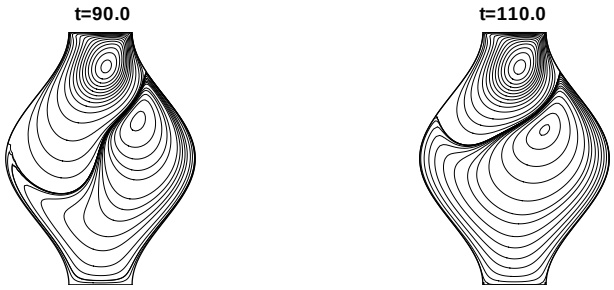

Figure 2.28: Streamline contour for Re=500 at different time

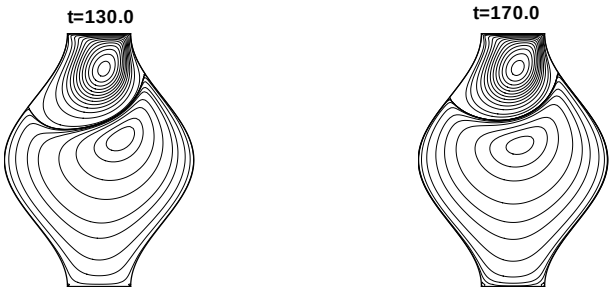

Figure 2.29: Streamline contour for Re=500 at different time

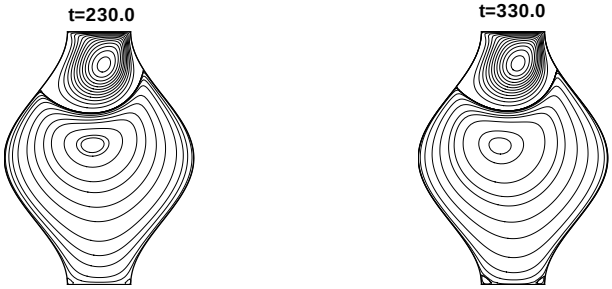

Figure 2.30: Streamline contour for Re=500 at different time

secondary vortices become visible at the bottom wall, at a larger time, these secondary vortices merge into a single secondary vortex near the bottom wall with the primary vortex. As time elapses, another new secondary vortex gradually appears near the center of the right wall. Then the two existing secondary vertices merge again with each other and gets larger with time and finally, at the steady-state situation, there are two vortices, the primary one at the top portion and the secondary one at the right lower portion of the cavity.

Figs 2.25-2.30 present the streamline contours for $Re = 500$ at different time levels. In this case, initially there is only one vortex near the top portion of the cavity, then a secondary vortex appears in the right side of the primary vortex. This secondary vortex gets larger in size and two more secondary vortices appear at the bottom part, then these two secondary vortices at the bottom part merge with each other with time and there are one primary vortex and two secondary vortices inside the cavity. At the next time levels, the secondary vortices again merge with each other and gets larger and at the final stage, there are two vortices, the primary vortex at the top part of the cavity and the secondary vortex occupies rest of the part of the cavity which is larger compared to the primary one.

3

Natural convection of an incompressible flow in a cavity with vertical wavy walls in presence of magnetic field and porous medium

Flow can be generated by creating density variations in the fluid. Natural convection is a mechanism in which the fluid motion takes place solely due to the density difference in the fluid.

The classical problem of natural convection in square enclosures has many engineering applications such as the cooling systems of electronic components, the building and thermal insulation systems, the built-in-storage solar collectors, the nuclear reactor systems, the food storage industry and the geophysical fluid mechanics [63]. The study of magnetohydrodynamic (MHD) flow and heat transfer for an electrically conducting fluid are usually encountered in electrical power generation, astrophysical flows, solar power technology and space vehicle re-entry. The application of magnetic field to convection processes will play as a control factor in the convection by damping both the flow and temperature oscillations in material manufacturing fields. In several energy conversion processes, strong external magnetic fields are applied to flowing liquid. There has been an increasing interest to understand the flow behaviour and the heat transfer mechanism in enclosures that are filled with electrically conducting fluids and are in the influence of a magnetic field [2, 18, 64, 106], The common finding of all these studies is that the fluid within the enclosure, which is under the magnetic effects, experiences a Lorentz force. This force, in turn, affects the buoyant flow field and the heat transfer rate.

Rudraiah et al.[85] numerically studied natural convection of an electrically conducting fluid in presence of a magnetic field in a rectangular enclosure using the modified two-step ADI (Alternating Direction Implicit) method and SLOR (Successive Line Over

Relaxation) method. They showed the effect of magnetic field to decrease the rate of convective heat transfer and mentioned that the average Nusselt number decreases with an increase in the Hartmann number. Natural convection in presence of a magnetic field is of great importance in many industrial applications such as crystal growth, metal casting and liquid metal cooling blankets for fusion reactors. The effect of magnetic field on convection heat transfer inside a tilted square enclosure heated from below and cooled from top where the inclined vertical walls are adiabatic was considered by Pirmohammadi and Ghassemi [78] using a finite volume code based on PATANKAR's SIMPLER method. They pointed out that the value of Nusselt number depends upon the inclination angle as well as the strength of the magnetic field. The problem of laminar viscous flow in a semi-porous channel in the presence of a magnetic field was studied by Sheikholeslami et al.[94] using Optimal Homotopy Asymptotic method. They investigated the effects of some parameters such as Hartmann number, Reynolds number on the fluid behavior.

The study of natural convection of liquid metal in presence of magnetic field in a vertical cylindrical container with a sinusoidal temperature distribution at the upper wall, other surfaces being adiabatic was investigated by Kakarantzas et al. [35]. Their results showed that the increase in Rayleigh number stimulates heat transfer by convection while the increase of Hartmann number damps the fluid motion and favors heat conduction. Various devices are applied for enhancing the heat transfer rate and mass transfer efficiency in natural convection problem. The use of wavy enclosure is one of them. Heat transfer inside annular space, air-filled cavity or annular sector has wide applications in many engineering problems like electronic packages, micro-electronic devices etc. The change in flow field with the changes in surface waviness is a special feature of the complex corrugated-duct geometry that is not encountered in conventional ducts such as circular and annular pipes and rectangular ducts. In addition to the electronic packages and heat exchanger design, wavy geometry has also some geophysical applications like flows in the earths crust. Geometrical complexity of such cavity or duct affects largely the flow pattern. Their fabrication depends on many parameters like amplitude, wavelength, phase angle, inter-wall spacing etc. Each of the parameter significantly affects the hydrodynamic and thermal behavior of fluid inside it. A laminar natural convection in an inclined square cavity with hot wavy wall was performed by Adjlout et al.[1]. The influence of the hot wavy wall on the local heat transfer rate was described and mentioned that the average heat transfer decreases with the waviness of the surface compared with flat wall. Das et al [14] solved numerically the natural convection inside a wavy enclosure for incompressible Newtonian fluid using finite volume method. Rate

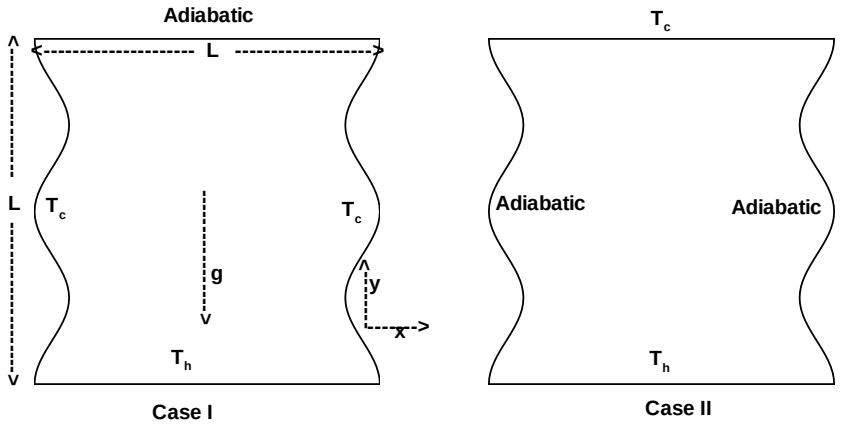

Figure 3.1: Geometrical sketch of the problem

of heat transfer in terms of local and global Nusselt numbers were presented for different amplitude-wavelength ratios and Grashof numbers, respectively.

This chapter deals with the work to study natural convection flow inside a square cavity with vertical wavy walls in the presence of magnetic field and also in the presence of porous medium. The governing equations are numerically solved by using the proposed HOC finite difference scheme, and effects of Rayleigh number, Prandtl number, Hartmann number and Darcy number on natural convection are discussed.

3.1 The Problem and the Governing Equations:

A two-dimensional incompressible flow of a Boussinesq fluid in a square cavity of length L, where both left and right vertical walls are wavy, is considered in this study. Two different cases are studied. In case I, the vertical walls are at temperature T_c and the bottom wall is at temperature T_h ($> T_c$), while the top wall is insulated. In case II, the bottom wall is heated with temperature T_h, the wavy vertical walls are adiabatic while the top wall is at temperature T_c. Fig 3.1 shows the schematic diagram of the problem.

From a physical point of view, the crucial features of the Boussinesq approximation in the case of a non-homogeneous, heat-conducting viscous, weakly expansible liquid in a gravity field, are: (i) density variations are neglected except in the buoyancy term, (ii) the influence of the pressure difference on the buoyancy and in the temperature equation can be neglected, (iii) the rate of viscous dissipation is neglected in the temperature equation. In fact, Boussinesq approximation works well only for thermal convective viscous motion with an insignificant temperature difference.

It is assumed that the fluid is Newtonian and the properties of the fluid is constant with the exception of that of the density. The Boussinesq approximation is used for the fluid properties to relate that the density changes with the change in the temperature.

A uniform magnetic field B is applied in the vertical direction of the cavity with the following assumptions:

(a) Electrical conductivity σ of the fluid is assumed to be constant and no external electric field is considered.

(b) The induced magnetic field produced by the motion of the fluid in presence of the external magnetic field is assumed to be negligible in comparison to the applied magnetic field.

The governing equations for natural convection in presence of magnetic field in porous media using the conservation of mass, momentum and energy can be written as

$$\frac{\partial u}{\partial x} + \frac{\partial v}{\partial y} = 0, \tag{3.1}$$

$$\frac{\partial u}{\partial t} + u\frac{\partial u}{\partial x} + v\frac{\partial u}{\partial y} = -\frac{1}{\rho}\frac{\partial p}{\partial x} + \nu\left(\frac{\partial^2 u}{\partial x^2} + \frac{\partial^2 u}{\partial y^2}\right) - \mathcal{S}\frac{\nu}{K}u - \frac{\sigma B^2 u}{\rho}, \tag{3.2}$$

$$\frac{\partial v}{\partial t} + u\frac{\partial v}{\partial x} + v\frac{\partial v}{\partial y} = -\frac{1}{\rho}\frac{\partial p}{\partial y} + \nu\left(\frac{\partial^2 u}{\partial x^2} + \frac{\partial^2 u}{\partial y^2}\right) - \mathcal{S}\frac{\nu}{K}v + g\beta(T - T_c), \tag{3.3}$$

$$\frac{\partial T}{\partial t} + u\frac{\partial T}{\partial x} + v\frac{\partial T}{\partial y} = \alpha\left(\frac{\partial^2 T}{\partial x^2} + \frac{\partial^2 T}{\partial y^2}\right), \tag{3.4}$$

where x and y are the axes along the horizontal and vertical directions respectively, u and v are the velocities along the x and y directions respectively, t is time, T is the temperature, ν and α are the kinematic viscosity and the thermal diffusivity respectively, p is the pressure, ρ is the density, g is the acceleration due to gravity, β is the volume expansion coefficient, K is the permeability of the porous media and a parameter $\mathcal{S}$ is introduced to write the general form of governing equations of fluid in an enclosure with porous media in presence of magnetic field.

In non-dimensional form, the equations can be written as:

$$\frac{\partial U}{\partial X} + \frac{\partial V}{\partial Y} = 0, \tag{3.5}$$

$$\frac{\partial U}{\partial \tau} + U\frac{\partial U}{\partial X} + V\frac{\partial U}{\partial Y} = -\frac{\partial P}{\partial X} + Pr\left(\frac{\partial^2 U}{\partial X^2} + \frac{\partial^2 U}{\partial Y^2}\right) - \mathcal{S}\frac{Pr}{Da}U - Ha^2 PrU, \tag{3.6}$$

$$\frac{\partial V}{\partial \tau} + U\frac{\partial V}{\partial X} + V\frac{\partial V}{\partial Y} = -\frac{\partial P}{\partial Y} + Pr\left(\frac{\partial^2 V}{\partial X^2} + \frac{\partial^2 V}{\partial Y^2}\right) - \mathcal{S}\frac{Pr}{Da}V + RaPr\theta, \tag{3.7}$$

$$\frac{\partial \theta}{\partial \tau} + U\frac{\partial \theta}{\partial X} + V\frac{\partial \theta}{\partial Y} = \frac{\partial^2 \theta}{\partial X^2} + \frac{\partial^2 \theta}{\partial Y^2}, \tag{3.8}$$

where $X = \frac{x}{L}$, $Y = \frac{y}{L}$, $U = \frac{uL}{\alpha}$, $V = \frac{vL}{\alpha}$, $\tau = \frac{t\alpha}{L^2}$, $\theta = \frac{T - T_c}{T_h - T_c}$, $P = \frac{pL^2}{\rho\alpha^2}$, i.e., X, Y, U, V, τ, θ are the dimensionless forms of x, y, u, v, t and T respectively.
$Pr = \frac{\nu}{\alpha}$, is the Prandtl number, $Ra = \frac{g\beta(T_h - T_c)L^3 Pr}{\nu^2}$ is the Rayleigh number,
$Ha = BL\sqrt{\frac{\sigma}{\nu\rho}}$ is the Hartmann number, $Da = \frac{K}{L^2}$ is the Darcy number.

Now, stream-function vorticity formulation is considered to solve the problem. The stream-function $\psi(X, Y)$ is defined in such a way that it satisfies the continuity equation. It is defined as

$$U = \frac{\partial \psi}{\partial Y}, \qquad V = -\frac{\partial \psi}{\partial X}$$

and vorticity $\zeta(X, Y)$ as $\zeta = \frac{\partial V}{\partial X} - \frac{\partial U}{\partial Y}$.

The stream-function vorticity formulation in presence of magnetic field with porous media can be written as

$$-\frac{\partial^2 \psi}{\partial X^2} - \frac{\partial^2 \psi}{\partial Y^2} = \zeta, \tag{3.9}$$

$$\frac{\partial \zeta}{\partial \tau} - Pr\frac{\partial^2 \zeta}{\partial X^2} - Pr\frac{\partial^2 \zeta}{\partial Y^2} + U\frac{\partial \zeta}{\partial X} + V\frac{\partial \zeta}{\partial Y} + \mathcal{S}\frac{Pr}{Da}V = RaPr\frac{\partial \theta}{\partial X} + Ha^2 Pr\frac{\partial U}{\partial Y}, \tag{3.10}$$

$$\frac{\partial \theta}{\partial \tau} - \frac{\partial^2 \theta}{\partial X^2} - \frac{\partial^2 \theta}{\partial Y^2} + U\frac{\partial \theta}{\partial X} + V\frac{\partial \theta}{\partial Y} = 0. \tag{3.11}$$

with the boundary conditions:
For case I: At the top wall, $U = 0$, $V = 0$, $\frac{\partial \theta}{\partial Y} = 0$.

At the bottom wall, $U = 0$, $V = 0$, $\theta = 1$ or $\theta = \sin(\pi X)$.
At the left and right vertical wall, $U = 0$, $V = 0$, $\theta = 0$.

For case II: At the top wall, $U = 0$, $V = 0$, $\theta = 0$.
At the bottom wall $U = 0$, $V = 0$, $\theta = 1$ or $\theta = \sin(\pi X)$.
At the left and right vertical wall, $U = 0$, $V = 0$, $\frac{\partial \theta}{\partial \bar{N}} = 0$.
where $\bar{N}$ is the non-dimensional normal to the boundaries.

In both the cases, $\psi = 0$ at all the boundaries and values of ζ are calculated using the the stream function equation (3.9). For Neumann boundary conditions, fourth order one-sided difference approximations are used.

Nusselt number (Nu) is the ratio of convective and conductive heat transfer normal to the boundary. The heat transfer coefficient in terms of local Nusselt number (Nu) is defined as:

$$Nu = -\frac{\partial \theta}{\partial \bar{N}}, \tag{3.12}$$

where $\bar{N}$ is the non dimensional normal to the boundary.

When $\mathcal{S} = 0$ and $Ha = 0$, the equations (3.9), (3.10), (3.11) represent the governing equations for flow problems without porous media and without magnetic field.
When $\mathcal{S} = 0$ but $Ha \neq 0$, the equations are for problems without porous media but in presence of magnetic field.
When $\mathcal{S} = 1$ but $Ha = 0$, the equations are for problems with porous media without magnetic field.
When $\mathcal{S} = 1$ but $Ha \neq 0$, the equations are for problems with porous media in presence of magnetic field.

In this chapter, two types of problems are discussed.
Problem I: $\mathcal{S} = 0$ and $Ha \neq 0$, i.e., the problems when there is no porous media but a magnetic field is applied in the vertical direction of the wavy wall cavity and two cases are studied for this problem
Case I: when the bottom wall is heated uniformly and non-uniformly both, with the cold wavy vertical walls while the top wall is kept at cold temperature,
Case II: when the bottom wall is heated, the top wall is cold and the vertical wavy walls are adiabatic.
Problem II:: $\mathcal{S} = 1$ and $Ha \neq 0$, i.e., the problem that deals with the situation when porous media is present and a magnetic field is also applied in the vertical direction of

the enclosure.

3.2 Numerical methods and Discretizations:

To solve this natural convection problem in presence of magnetic field and also porous media, the stream-function vorticity formulation of the governing equations is considered and solved. Since, the geometry considered here is not a regular geometry and both the left and right walls are wavy, a transformation is applied for this problem so that this geometry gets transformed to a square cavity with a uniform grid and the problem is solved.

The transformation used for this problem from (X, Y) to (ξ, η) plane is

$$X = \xi(1 - 2\lambda + 2\lambda\cos(2\pi M\eta)) + \lambda(1 - \cos(2\pi M\eta)),$$
$$Y = \eta.$$

The value of λ taken here is 0.05 and $M = 2$, the number of undulations.

Using this transformation, the governing equations with time derivative term (3.11) and (3.10) for this problem which is of this type

$$l\frac{\partial\phi}{\partial t}+a\frac{\partial^2\phi}{\partial x^2}+g\frac{\partial^2\phi}{\partial x\partial y}+b\frac{\partial^2\phi}{\partial y^2}+c\frac{\partial\phi}{\partial x}+d\frac{\partial\phi}{\partial y}+r\phi = \chi+l_1\frac{\partial\epsilon_1}{\partial x}+l_2\frac{\partial\epsilon_1}{\partial y}+l_3\frac{\partial\epsilon_2}{\partial x}+l_4\frac{\partial\epsilon_2}{\partial y}, \quad (3.13)$$

may be written as:

$$l\frac{\partial\hat{\phi}}{\partial t} + a_1\frac{\partial^2\hat{\phi}}{\partial\xi^2} + b_1\frac{\partial^2\hat{\phi}}{\partial\eta^2} + g_1\frac{\partial^2\hat{\phi}}{\partial\xi\partial\eta} + c_1\frac{\partial\hat{\phi}}{\partial\xi} + d_1\frac{\partial\hat{\phi}}{\partial\eta} + r_1\hat{\phi} = f_1, \quad (3.14)$$

where the coefficients are obtained using the relations available in (2.3) in Chapter 2.

After discretization, using the same procedure discussed in Chapter 2 for time dependent case, the equation can be written in algebraic form, as:

$$\sum_{s_1=-1}^{1}\sum_{s_2=-1}^{1} w_{i+s_1,j+s_2}\phi^{(n+1)}_{i+s_1,j+s_2} = \sum_{s_1=-1}^{1}\sum_{s_2=-1}^{1} w'_{i+s_1,j+s_2}\phi^{(n)}_{i+s_1,j+s_2} + \Delta t\left(\mu F^{(n+1)}_{i,j} + (1-\mu)F^{(n)}_{i,j}\right). \quad (3.15)$$

For equation (3.11), $\phi = \theta$, $l = 1$, $a = -1$, $b = -1$, $c = U$, $d = V$, $g = 0$, $r = 0$, $\chi = 0$, $l_1 = 0$, $l_2 = 0$, $l_3 = 0$, $l_4 = 0$ and for equation (3.10), $\phi = \zeta$, $a = -Pr$, $b = -Pr$, $c = U$, $d = V$, $g = 0$, $r = \mathcal{S}\dfrac{Pr}{Da}$, $\chi = 0$, $l_1 = RaPr$, $l_2 = 0$, $l_3 = 0$, $L_4 = Ha^2Pr$, $\epsilon_1 = \theta$ and $\epsilon_2 = U$.

The equation (3.9) is of the type

$$a\frac{\partial^2\phi}{\partial x^2} + g\frac{\partial^2\phi}{\partial x\partial y} + b\frac{\partial^2\phi}{\partial y^2} + c\frac{\partial\phi}{\partial x} + d\frac{\partial\phi}{\partial y} + r\phi = \chi + l_1\frac{\partial\epsilon_1}{\partial x} + l_2\frac{\partial\epsilon_1}{\partial y} + l_3\frac{\partial\epsilon_2}{\partial x} + l_4\frac{\partial\epsilon_2}{\partial y}, \quad (3.16)$$

which after taking the transformation, becomes

$$a_1\frac{\partial^2\hat{\phi}}{\partial\xi^2}+b_1\frac{\partial^2\hat{\phi}}{\partial\eta^2}+g_1\frac{\partial^2\hat{\phi}}{\partial\xi\partial\eta}+c_1\frac{\partial\hat{\phi}}{\partial\xi}+d_1\frac{\partial\hat{\phi}}{\partial\eta}+r_1\hat{\phi}=f_1, \tag{3.17}$$

where the coefficients are obtained using the relations available in 2.3 in Chapter 2.

After discretization, using the same procedure discussed in Chapter 2 for time independent case, the equation can be written in algebraic form

$$\sum_{s_1=-1}^{1}\sum_{s_2=-1}^{1} w_{i+s_1,j+s_2}\phi_{i+s_1,j+s_2}=F_{i,j}. \tag{3.18}$$

For equation (3.9), $\phi=\psi$, $a=-1$, $b=-1$, $c=0$, $d=0$, $g=0$, $r=0$, $\chi=\zeta$, $l_1=0$, $l_2=0$, $l_3=0$, $l_4=0$.

Biconjugate-Gradient stabilized methods without preconditioning are applied for solving the system of equations in all the cases whenever it appears during the process of solving the equations after discretizations.

3.3 Problem 1: Natural convection in presence of magnetic field without porous media:

In this problem $\mathcal{S}=0$ but $Ha\neq 0$.

3.3.1 Results and discussions:

Several grid size results for ψ_{max} (maximum value of ψ) and the position of the vortex are compared for $Ra=1000$, $Pr=0.7$, $Ha=1$ for case I.

It is seen from the tabular values of ψ_{max} and the position of the vortex that the result of 61×61 slightly changes from the other grid size results. So, 61×61 grid size results are considered throughout this chapter.

Case I:

Here the bottom wall is heated, the top wall is adiabatic and the vertical walls are cold. Because of the cold vertical wall on the left and right side, the fluid rises up from the middle portion of the bottom wall and flows down through the cold vertical

Table 3.1: ψ_{max} and its position for different grid sizes for natural convection problem

Grid size	ψ_{max}	Position of the vortex(x, y)
21×21	0.112875	(0.3138, 0.4)
41×41	0.11351	(0.2975, 0.375)
61×61	0.113904	(0.3027, 0.3833)
81×81	0.114033	(0.3054, 0.3875)

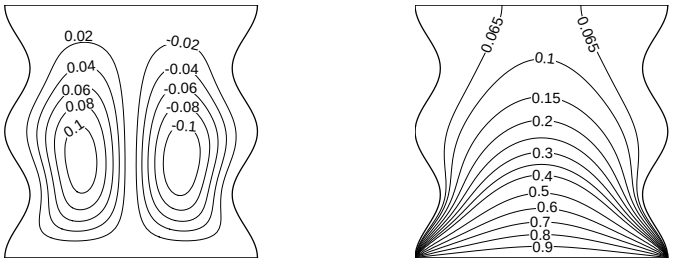

Figure 3.2: Streamlines and isotherms for uniform heating with Ra=1000, Ha=1, Pr=0.71

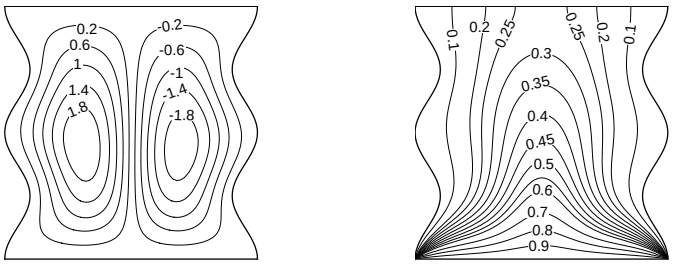

Figure 3.3: Streamlines and isotherms uniform heating with Ra=10000, Ha=1, Pr=0.71

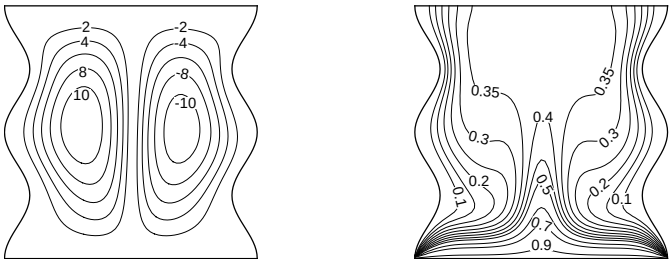

Figure 3.4: Streamlines and isotherms for uniform heating with Ra=100000, Ha=1, Pr=0.71

walls. Two symmetric rolls appear for this, one with clockwise and other with anti clockwise rotation. From Fig 3.2, one can see that at $Ra = 1000$, the magnitude of the streamlines are low. From the isotherm contours, it can be seen that there is a symmetric temperature distribution about the vertical center line.

Fig 3.3 shows the streamline and isotherm contours for $Ra = 10000$. One can easily observe that contour values are much higher in the case of $Ra = 10000$ compared to $Ra = 1000$ which indicates that circulations become much stronger with the increase in Rayleigh number. It is also seen that contour values in isotherms increase with the increase of Rayleigh number. It is clear from the Fig 3.3 that at $Ra = 10000$, temperature contour with $\theta = 0.1$ starts getting shifted towards the side wall and break into two symmetric contour lines whereas in the case of $Ra = 1000$ from Fig 3.2, it is seen that the temperature contour at $\theta = 0.1$, the contour is smooth and span the whole enclosure. The other temperature contours also start getting deformed and pushed towards the top wall compared to the case of $Ra = 1000$ in Fig 3.2. This indicates that the temperature in the whole domain rises due to stronger circulations.

Fig 3.4 shows that, at $Ra = 100000$, the circulation inside the cavity becomes more stronger as the magnitude of the streamline increases very much, maximum near the center and weak near the wall due to no slip boundary conditions at the wall. The temperature gradient near the bottom and side walls become significant and develop a thermal boundary layer .

From Fig 3.2 and Fig 3.5, the effects of uniform and non-uniform heating at the bottom wall are very much clear. When the bottom wall is heated uniformly, there are finite discontinuities at the bottom corners, but when non-uniform heating is applied no discontinuity at the bottom corners is noticed. For the non-uniform heating, it is seen

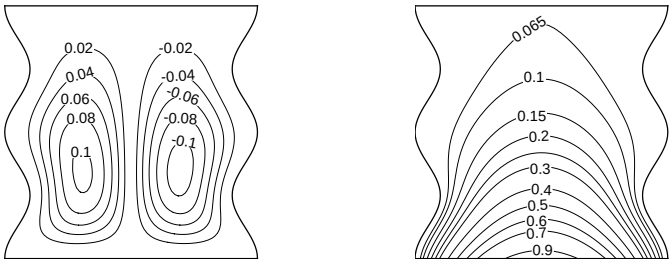

Figure 3.5: Streamlines and isotherms for non-uniform heating with Ra=1000, Ha=1, Pr=0.71

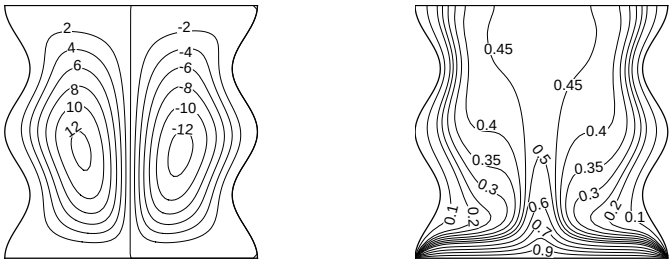

Figure 3.6: Streamlines and isotherms for uniform heating with Ra=100000, Ha=1, Pr=7

that the temperature distribution is smooth through the entire enclosure.

With the increase of Pr from 0.71 to 7, the Fig 3.6 depicts that the magnitude of the streamlines and isotherm increase for $Ra = 100000$, which means the circulations increase in the cavity.

From Figs 3.3, 3.7 and 3.8, it can be shown that with the increase in Hartmann number, the magnitude of the streamlines and isotherms decrease, which means that the circulations inside the cavity becomes weaker for $Ra = 10000$ and $Pr = 0.71$.

Fig 3.9 and 3.10 depicts the local heat transfer rate at the bottom wall for uniform and non-uniform heating for $Ra = 1000$ and $Ra = 10000$ respectively for fixed values of $Ha = 1$ and $Pr = 0.71$. It shows that heat transfer rate is maximum at the bottom left and bottom right corners for uniform heating. The cause for this could be that there are sudden change in temperature at the corners as the bottom wall is at high temperature throughout whereas vertical sidewalls are at low temperature. Heat transfer

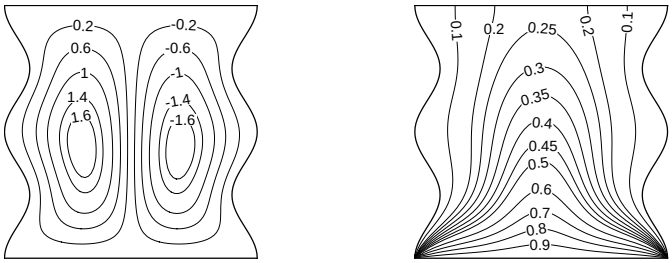

Figure 3.7: Streamlines and isotherms for uniform heating with Ra=10000, Ha=10, Pr=0.71

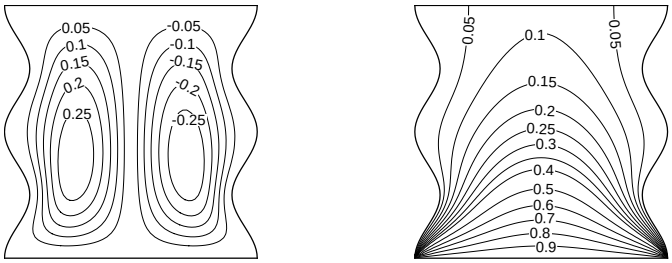

Figure 3.8: Streamlines and isotherms for uniform heating with Ra=10000, Ha=50, Pr=0.71

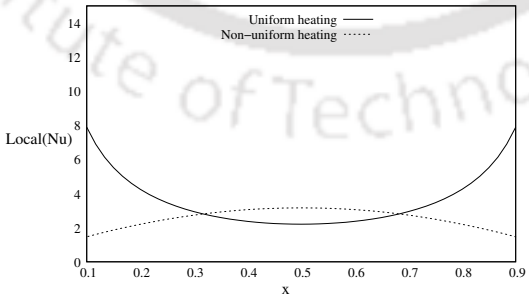

Figure 3.9: Local Nusselt number at the bottom wall for uniform and non-uniform heating with Ra=1000 and Pr=0.71

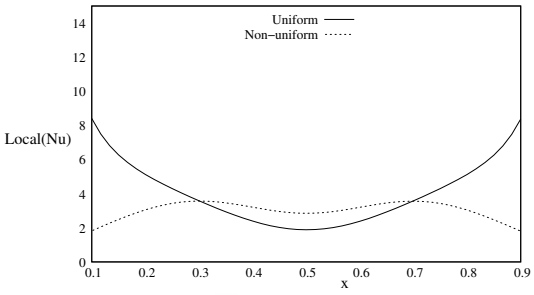

Figure 3.10: Local Nusselt number at the bottom wall for uniform and non-uniform heating with Ra=10000 and Pr=0.71

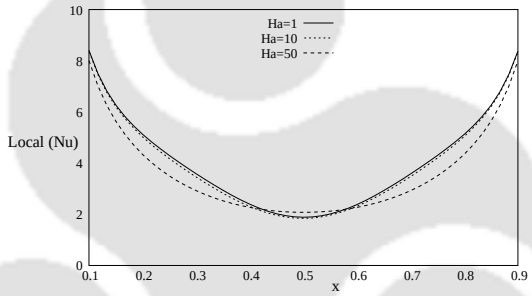

Figure 3.11: Local Nusselt number at the bottom wall for different Ha for uniform heating with Ra=10000 and Pr=0.71

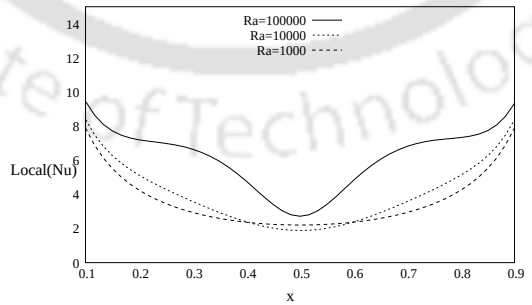

Figure 3.12: Local Nusselt number at the bottom wall for different Ra for uniform heating with Ha=1 and Pr=0.71

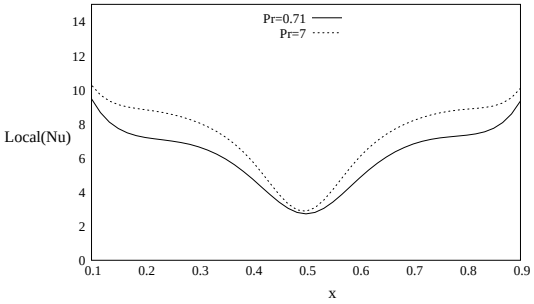

Figure 3.13: Local Nusselt number at the bottom wall for different Pr for uniform heating with Ra=100000, Ha=1

rate decreases as it moves towards the middle of the bottom wall and is minimum at the center of the bottom wall. For non-uniform heating, a temperature profile is considered as $\sin(\pi x)$, $0 \leq x \leq 1$. So, the temperature at the bottom corner points becomes zero, no matter what way one approaches (horizontally or vertically) towards the bottom corner points. So, the heat transfer rate near the corners is minimum (i.e., zero). Temperature increases as one moves towards the middle of the bottom wall and at the center of the bottom wall, the heat transfer rate is maximum. The non-uniform heating enhances the heat transfer rate at the center of the bottom wall with comparison to that in the case of uniform heating. For different profiles of non-uniform heating at the bottom wall, the heat transfer rate distribution also changes accordingly.

The effects of Rayleigh number are shown in Fig 3.12 for uniform heating with fixed $Ha = 1$ and $Pr = 0.71$. With the increase in Rayleigh number (i.e., with the increase in temperature difference between the cold and hot walls), the hotter fluid will be replaced by the colder one rapidly due to stronger convection, as a result, the heat transfer rate at the hotter wall is increased. At $Ra = 1000$, the streamline contours show that there are two symmetric convective cells at the left and right halves of the cavity, the circulation is higher at the center of the convective cell and is reduced near the wall boundary. The heat transfer rate at the bottom wall is influenced by the flow pattern in the cavity and a slight waviness is noticed in the plot of Nusselt number for $Ra = 10000$ compared to that for $Ra = 1000$. As Ra increases to 100000, the same pattern in streamline contour is observed but the magnitude of the streamline contours increases, hence the heat transfer rate increases. From the isotherm contour, it is seen that as the Ra increases, the isotherm contour shows some complexity in its patterns. For this reason as Ra increases to 100000, the wavy like nature is seen in the local Nusselt number along the bottom hot wall.

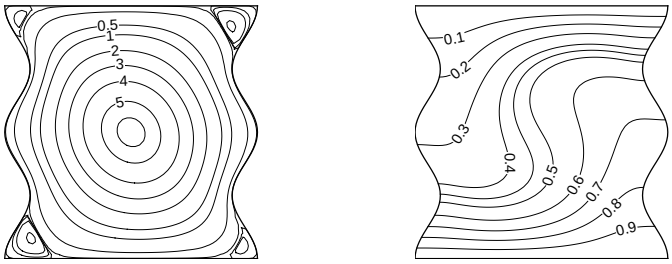

Figure 3.14: Streamlines and isotherms for uniform heating with Ra=10000, Ha=1, Pr=0.7 for Case II

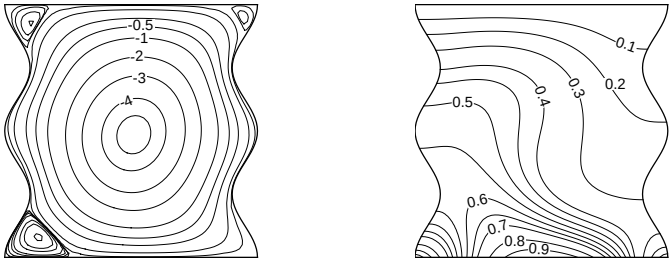

Figure 3.15: Streamlines and isotherms for non-uniform heating with Ra=10000, Ha=1, Pr=0.7 for Case II

Fig 3.13 shows the effects of Prandtl number on the Nusselt number at the bottom wall heated uniformly with fixed $Ra = 100000$ and $Ha = 1$. With the increase of Pr from 0.71 to 7, the heat transfer rate increases at the bottom wall. $Pr = 0.71$ and $Pr = 7$ represent, respectively, the air and water media at some temperature (around 20^0C). For comparison between air and water, the thermal conductivity of water is higher than that of air. So, the momentum diffusivity of water is also higher compared to that of air. So, the heat transfer rate is higher in water medium.

Fig 3.11 shows the effect of Hartmann number Ha for uniform heating with fixed $Ra = 10000$ and $Pr = 0.71$. Since with the increase of Hartmann number, the velocity becomes weaker, the figure also shows that the heat transfer rate decreases with the increase in Hartmann number, as expected.

Case II:

In this case the bottom wall is heated, while the vertical side walls are adiabatic and the top wall is cold. The effect of uniform and non-uniform heating is discussed for $Ra = 10000$ and $Ha = 1$. For $Ra = 10000$, it is seen from Fig 3.14 that only one roll is formed in the cavity and smaller rolls are formed at every corner of the cavity. Whereas, for non-uniform heating, Fig 3.15 shows that there is no roll at the right bottom corner of the cavity and the temperature contours are different from the uniform heating case. Near the bottom wall, nice temperature distribution (seen in the case of uniform heating) is influenced and disturbed by the non-uniform distribution of temperature at the bottom wall.

3.4 Problem 2: Natural convection in presence of magnetic field in cavity filled with fluid-saturated porous medium:

The study of natural convection in a two-dimensional enclosure filled with fluid-saturated porous media has received significant attention in recent years and plays important roles in many applications. The problem has been studied in various types of shapes of the enclosure such as cylindrical, rectangular, trapezoidal, triangular etc. with different boundary conditions due to its applications in geophysics, geothermal reservoirs, insulation of buildings, crude oil production, separation processes in industries etc.

The study of natural convection flows in a trapezoidal enclosure due to uniform and non-uniform heating of the bottom wall and cold vertical walls is made by Basak *et. al* [7]. They also have investigated a similar problem in a triangular geometry in [5]

Oztop *et. al* [65] studied the natural convection problem in a wavy enclosure containing internal heat sources at different wave ratios using finite volume method.

In [96], Sompong and Witayangkurn studied the flow field, temperature distribution and heat transfer due to natural convection in a square enclosure having two wavy vertical walls numerically. However, they didn't consider any magnetic field in their study.

The objective of this part of this chapter is to investigate the flow field, temperature distribution due to heat transfer for natural convection inside a square enclosure having two wavy vertical walls in the presence of a magnetic field. The problem is solved

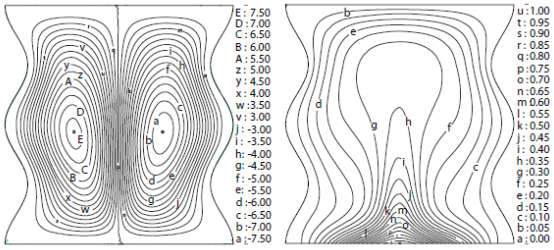

Figure 3.16: Streamlines and isotherms for Da=0.01 and Ra=100000 obtained from [96]

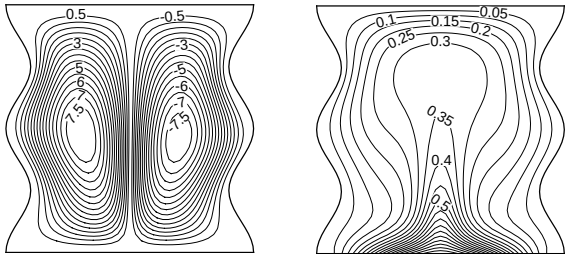

Figure 3.17: Streamlines and isotherms for Da=0.01 and Ra=100000 obtained from the proposed scheme

numerically by using the fourth order accurate scheme proposed in Chapter 2. The enclosure is filled with fluid-saturated porous media. A magnetic field B is applied in the vertical direction of the enclosure. The bottom wall is heated (T_h) uniformly while the vertical walls are adiabatic and the top one is maintained at temperature T_c ($T_h > T_c$).

3.5 Validation of the numerical results:

In this problem $\mathcal{S} = 1$ and $Ha \neq 0$.

A grid independent study for this problem is performed and a grid size of 61×61 is found to be good enough for grid independent results. In order to validate the numerical results of this problem obtained through the proposed HOC scheme, a comparison is made between the present results and the results obtained by Sompong and Witayangkurn [96].

Figs 3.16 and 3.18 show the streamline and isotherm contours for $Da = 0.0001$ and $Da = 0.01$ respectively, for fixed $Ra = 100000$ mentioned in [96] whereas Fig 3.17

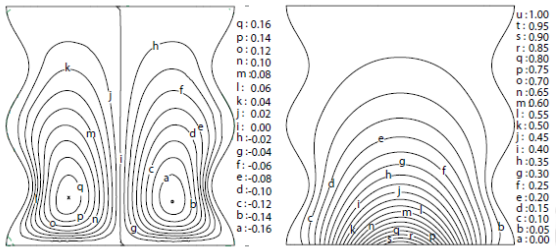

Figure 3.18: Streamlines and isotherms for Da=0.0001 and Ra=100000 obtained from [96]

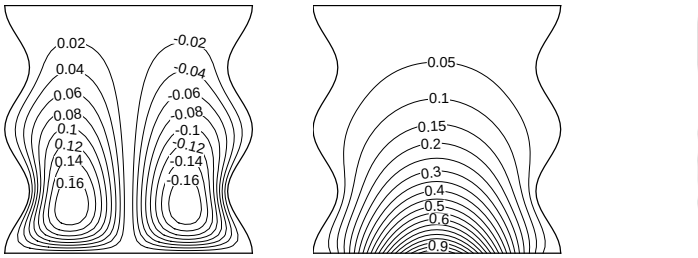

Figure 3.19: Streamlines and isotherms for Da=0.0001 and Ra=100000 obtained from the proposed scheme

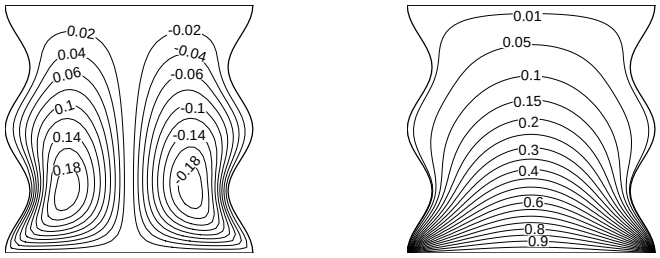

Figure 3.20: Streamlines and isotherms for Da=0.0001 $Ha = 1$ and Ra=100000

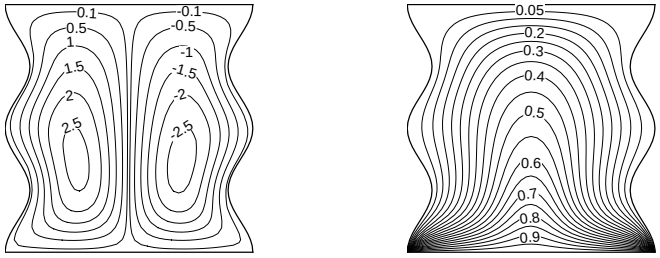

Figure 3.21: Streamlines and isotherms for Da=0.001, Ha=1 and Ra=100000

and 3.19 show the streamline and isotherm contours for $Da = 0.0001$ and $Da = 0.01$ respectively, where the solutions are obtained using the proposed HOC scheme discussed in Chapter 2. A good agreement is found.

3.6 Results and Discussions:

Results are numerically obtained using the proposed HOC scheme for the following values of parameters. Rayleigh number (Ra) ranging from 10 to 100000, Darcy number (Da) from 0.0001 to 0.1 and Hartmann number (Ha) from 1 to 50 for fixed $Pr = 0.71$. Results are discussed through streamlines and isotherm contours and variations in Nusselt number at the bottom wall.

Figs 3.20-3.22 represent streamlines and isotherm contours for $Ha = 1$, $Ra = 100000$ and Da varies from 0.0001 to 0.01. It is clear from the contours that circulations are symmetric with respect to the vertical center line and two convective roles are observed, one in clockwise and other one in anti-clockwise directions. With the increase of Da, the flow strength increases. It is observed from the isotherms of these figures that

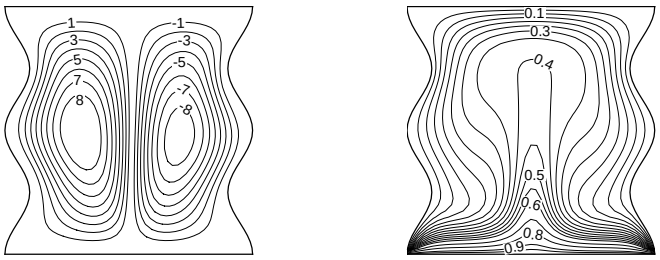

Figure 3.22: Streamlines and isotherms for Da=0.01, Ha=1 and Ra=100000

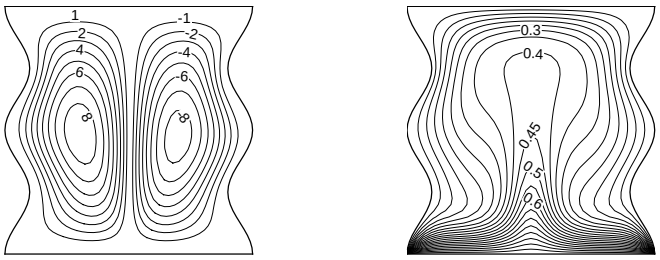

Figure 3.23: Streamlines and isotherms for Da=0.01, Ha=10 and Ra=100000

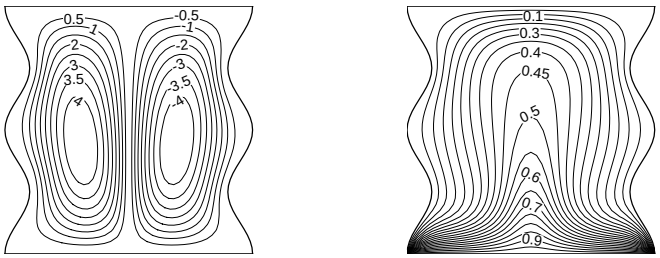

Figure 3.24: Streamlines and isotherms for Da=0.01, Ha=50 and Ra=100000

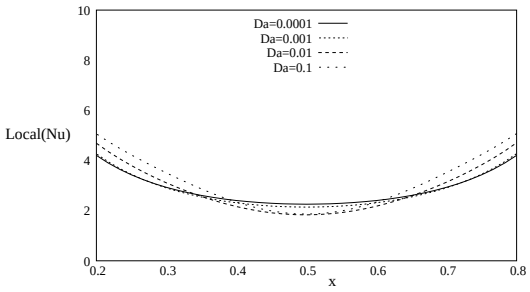

Figure 3.25: Local Nusselt number for Da with Ha=1, Pr=0.71 and Ra=100000

the temperature increases in the cavity as Da increases. The temperature distribution is observed from the isotherm contour. Figs 3.22-3.24 reveal the effects of Hartmann number Ha on streamlines and isotherms for $Da = 0.01$ and $Ra = 100000$. It is clear from the streamline contours that with the increase in Hartmann number, the strength of the flow decreases, as the magnitude of the streamlines become smaller.

Fig 3.25 shows the effects of Da on the heat transfer rate (i.e., Nusselt number at the bottom wall) for $Ra = 100000$, $Ha = 1$ and $Pr = 0.71$. It shows that with the increase of Darcy number Da, the heat transfer rate increases at the edges of the bottom wall, but towards its center, the heat transfer rate decreases with the increase in Da.

3.7 Conclusions:

In this chapter, the natural convection in two-dimensional wavy enclosure in presence of magnetic field has been studied numerically. The left and right walls of the enclosure are wavy. The bottom wall is heated either uniformly or non-uniformly ($T(x) = \sin(\pi x)$). In this study, Rayleigh number varies from 1000 to 100000, Hartmann number from 1 to 50. Two Pandtl numbers are considered as 0.71 and 7. The number of undulation is kept fixed at $M = 2$. High order compact finite difference scheme proposed in Chapter 2 is used to solve the non-dimensional governing equations. The important results obtained from this study are as follows:

(1) When the Rayleigh number is higher (> 1000), the local Nusselt number shows an oscillatory behaviour along the bottom wall due to the presence of multiple vortices in the cavity. However, it attains its maximum value at the corner points of the bottom wall and the minimum one at the center.

(2) Local heat transfer rate at the center of the bottom wall is higher in the case of non-uniform heating in comparison to that of uniform heating.

(3) When Ra is 1000, there is no difference in the local heat transfer rate at the bottom

wall for the Prandlt number 0.71 and 7, but as Ra increases to 100000, a noticeable difference in local Nusselt numbers at the bottom wall for these two Prandlt numbers is observed.

(4) With the increase in Hartmann number, the velocity as well as the heat transfer rate decreases.

4

Mixed convection in trapezoidal cavity

Mixed convection flow in an enclosure occurs because of two competing mechanisms. The first one is due to shear flow caused by the movement of one of the walls of the cavity while the second one is due to buoyancy flow produced by thermal non homogeneity of the cavity boundaries. Mixed convection in cavities or channels due to temperature difference between the walls or with the fluids and walls is important from both theoretical and practical points of view. This type of configuration is encountered in various engineering applications.

Flow and heat transfer analysis in lid-driven cavities is one of the most widely studied problems in the thermo-fluid area. A sizeable number of different configurations and combinations of thermal boundary conditions have been considered and analyzed by various investigators. This is because the driven cavity configuration has a lot of applications in practical engineering and industrial field.

For the cooling of computer systems and other electronic equipments, air cooling is one of the important methods because of its simplicity and low cost. It is a general requirement that the cooling systems should be designed in such a way that the power requirement for such cooling systems should be minimized. The electronic equipments are considered as the heat sources inserted on flat surfaces. In this system, a small fan blows air at a low speed over the heat sources. In this situation, a forced convection due to shear driven flow and a natural convection due to buoyancy driven flow happen in the system and these heat transfer processes result in mixed convection. Mixed convection flow and heat transfer occur often in many engineering and natural situations.

One important configuration is a lid-driven (or shear-driven) flow in a differentially heated/cooled cavity, which has applications in crystal growth, flow and heat transfer in solar ponds [11], dynamics of lakes [29], thermal-hydraulics of nuclear reactors [28], industrial processes such as food processing, and float glass production [77]. The inter-

action of the shear driven flow due to the lid motion and natural convective flow due to the buoyancy effect is quite complex and warrants comprehensive analysis to understand the physics of the resulting flow and heat transfer process.

In 1972, Torrance et al.[103] numerically studied the fluid motion driven by the combined effect of the moving wall and natural convection. Papaniclaou and Jaluria [69, 70, 71, 72, 73] carried out a series of numerical studies to investigate the combined forced and natural convective cooling of heat dissipating electronic components, located in rectangular enclosures, and cooled by an external through flow of air. Khanafer and Chamakha [37] numerically examined mixed convection flow in a lid-driven enclosure filled with a fluid saturated porous medium and reported on the effects of the Darcy and Richardson numbers on the flow and heat transfer characteristics. The two vertical walls of the square enclosure are insulated while the horizontal walls are kept at constant temperatures with the top surface moving at a constant speed. G. A. Holtzman et. al [25] studied laminar natural convection in isosceles triangular enclosures heated from below and symmetrically cooled from above. This problem is examined over aspect ratios ranging from 0.2 to 1.0 and Grashoff numbers from 10^3 to 10^5.

The phenomenon of natural convection in trapezoidal enclosures where upper and lower walls are not parallel, in particular a triangular geometry, is examined by H. Asan, L. Namli [4] over a parameter domain in which the aspect ratio of the enclosure ranges from 0.1 to 1.0, the Rayleigh number varies between 10^2 to 10^5 and Prandtl numbers correspond to air and water. It is found that the numerical experiments verify the flow features that are known from theoretical asymptotic analysis of this problem (valid for shallow spaces) only over a certain range of the parametric domain. Moallemi and Jang [57] numerically studied mixed convective flow in a bottom heated square driven cavity and investigated the effect of Prandtl number on the flow and heat transfer process. They found that the effects of buoyancy are more pronounced for higher values of Prandtl number. They also derived a correlation for the average Nusselt number in terms of the Prandtl number, Reynolds number, and Richardson number. Mohammad and Viskanta [58] performed numerical investigation and flow visualization study on two and three-dimensional laminar mixed convection flow in a bottom heated shallow driven cavity filled with water having a Prandtl number of 5.84. They concluded that the lid motion destroyed all types of convective cells due to heating from below for finite size cavities. They also implicated that the two-dimensional heat transfer results compared favorably with those based on a three-dimensional model for $Gr/Re < 1$. Later, Mohammad and Viskanta [59] experimentally and numerically studied mixed convection in shallow rectangular bottom heated cavities filled with liquid Gallium having a low

Prandtl number of 0.022. They found that the heat transfer rate was rather insensitive to the lid velocity and an extremely thin shear layer existed along the major portion of the moving lid. The flow structure consists of an elongated secondary circulation that occupies a third of the cavity. Mansour and Viskanta [53] studied mixed convective flow in a tall vertical cavity where one of the vertical sidewalls, maintained at a colder temperature than the other one, was moving up or downward thus assisting or opposing the buoyancy. They observed that when shear assisted the buoyancy a shear cell developed adjacent to the moving wall while the buoyancy cell filled the rest of the cavity. When shear opposed buoyancy, the heat transfer rate reduced below that for purely natural convection. Iwatsu et al. [32] and Iwatsu and Hyun [31] conducted two-dimensional and three-dimensional numerical simulation of mixed convection in square cavities heated from the top moving wall. Mohammad and Viskanta [60] conducted three-dimensional numerical simulation of mixed convection in a shallow driven cavity filled with a stably stratified fluid heated from the top moving wall and cooled from below for a range of Rayleigh number and Richardson number. Prasad and Koseff [79] reported experimental results for mixed convection in deep lid driven cavities heated from below. In a series of experiments which were performed on a cavity filled with water, the heat flux was measured at different locations over the hot cavity floor for a range of Re and Gr. Their results indicated that the overall (i.e. area-averaged) heat transfer rate was a very weak function of Gr for the range of Re examined ($2200 < Re < 12000$). The data were correlated by Nusselt number vs Reynolds number, as well as Stanton number vs Reynolds number relations. They observed that the heat transfer is rather insensitive to the Richardson number. Hsu and Wang [26] investigated the mixed convective heat transfer where the heat source was embedded on a board mounted vertically on the bottom wall at the middle in an enclosure. The cooling air flow enters and exits the enclosure through the openings near the top of the vertical sidewalls. The results showed that both the thermal field and the average Nusselt number depended strongly on the governing parameters, position of the heat source, as well as the property of the heat-source-embedded board. Aydin and Yang [108] numerically studied mixed convection heat transfer in a two dimensional square cavity having moving cooled sidewalls and locally heated bottom wall whereas the remaining parts of the bottom surface and the upper wall were considered to be adiabatic.

Shankar et al. [92] presented analytical solution for mixed convection in cavities with very slow lid motion. The convection process has been seen to be governed by an inhomogeneous biharmonic equation for the stream function. Oztop and Dagtekin [66] performed numerical analysis of mixed convection in a square cavity with moving and

differentially heated sidewalls. Sharif [93] investigates heat transfer in a two-dimensional shallow rectangular driven cavity of aspect ratio 10 and Prandtl number 6.0 with hot moving lid at the top and cooled from bottom. They investigated the effect of Richardson number and inclination angle. G. Guo and M. A. R. Sharif [22] studied mixed convection in rectangular cavities at various aspect ratios with moving isothermal sidewalls and constant heat source at the bottom wall. They plotted the streamlines and isotherms for different values of Richardson number and also studied the variation of the average Nusselt number and maximum surface temperature at the heat source with Richardson number with different heat source length. They simulated streamlines and isotherms for asymmetric placements of the heat source and also the effects of asymmetry of heating elements on the average Nusselt number and the maximum source length temperature.

Heat transfer in a tilted enclosure has received considerable attention due to its application to solar collector technology. The angle of tilt has a greater impact on the flow housed by the enclosure. In [51], investigation is carried out in a two-dimensional lid-driven trapezoidal enclosure filled with air. The inclined side walls are kept adiabatic and the bottom wall of the cavity is kept at uniform heat flux. The cooled top wall having constant temperature will move with a constant velocity. The variation of average heat transfer in terms of Nusselt number with the variation of Richardson number at different aspect ratios of the rectangular enclosure, the optimum configuration by changing the inclination angle of the side walls of the trapezoidal cavity by analyzing the maximum heat transfer, the variation of average heat transfer in terms of Nusselt number with the variation of Richardson number of the optimum trapezoidal cavity, the variation of average heat transfer in terms of Nusselt number with the variation of Richardson number at different aspect ratios of the optimum trapezoidal enclosure by changing the rotation angle for both aiding and opposing flow conditions are studied.

In the present chapter, flow and heat transfer are studied in a two dimensional lid driven trapezoidal enclosure filled with fluid. The inclined side walls are kept at lower temperature and the bottom wall of the cavity is heated. The adiabatic top wall having constant temperature moves with a constant velocity.

4.1 The Problem formulation and Governing equations

Mixed convection within two-dimensional trapezoidal enclosure with moving top lid is considered and the physical model is depicted in Fig 4.1. In this figure, the cavity is heated from bottom wall with temperature T_h and the temperature of inclined walls

are lower than those of bottom wall with the temperature T_c where $T_h > T_c$. The top wall is adiabatic which moves from left to right at a constant speed of U_0. The length of bottom heated wall is shown by L and the adiabatic top wall is H. The cavity is filled with a fluid whose flow is assumed to be Newtonian, incompressible and viscous.

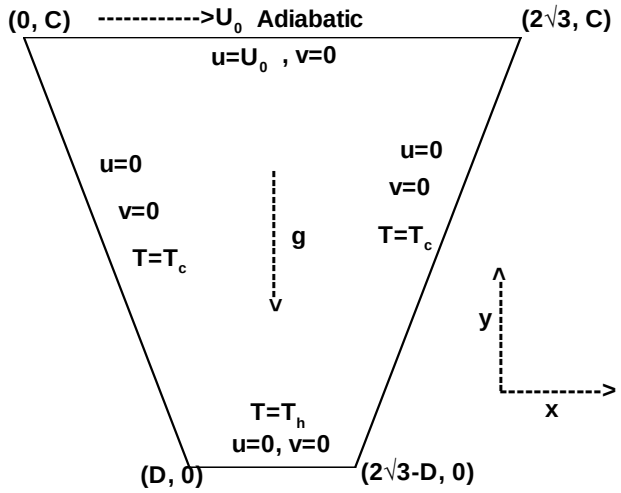

Figure 4.1: Geometry of the problem with boundary conditions

The flow is assumed to be laminar and the fluid properties are invariant except for the density. The density variation is treated according to the Boussinesq approximation. Viscous dissipation effects are considered to be negligible.

The governing Navier-Stokes equations for fluid flow and energy equation for temperature distribution for the present configuration can be written as

$$\frac{\partial u}{\partial x} + \frac{\partial v}{\partial y} = 0, \tag{4.1}$$

$$u\frac{\partial u}{\partial x} + v\frac{\partial u}{\partial y} = -\frac{1}{\rho}\frac{\partial p}{\partial x} + \nu\left(\frac{\partial^2 u}{\partial x^2} + \frac{\partial^2 u}{\partial y^2}\right), \tag{4.2}$$

$$u\frac{\partial v}{\partial x} + v\frac{\partial v}{\partial y} = -\frac{1}{\rho}\frac{\partial p}{\partial y} + \nu\left(\frac{\partial^2 u}{\partial x^2} + \frac{\partial^2 u}{\partial y^2}\right) + g\beta(T - T_c), \tag{4.3}$$

$$u\frac{\partial T}{\partial x} + v\frac{\partial T}{\partial y} = \alpha\left(\frac{\partial^2 T}{\partial x^2} + \frac{\partial^2 T}{\partial y^2}\right), \tag{4.4}$$

with the following boundary conditions:
at the heated bottom wall $u = 0$, $v = 0$, $T = T_h$,

at the two inclined left and right walls $u = 0$, $v = 0$, $T = T_c$,
at the top adiabatic moving wall $u = U_0$, $v = 0$, $\dfrac{\partial T}{\partial y} = 0$,
where x and y indicate horizontal and vertical axes respectively, u is the velocity along x direction, v is the velocity along y direction, T is the temperature, ρ is the density of the fluid, p is the pressure, g is the gravitational acceleration, ν is the kinematic viscosity, β is the volume expansion coefficient, α is the thermal diffusivity.

In dimensionless form the equations can be written as

$$\frac{\partial U}{\partial X} + \frac{\partial V}{\partial Y} = 0, \tag{4.5}$$

$$U\frac{\partial U}{\partial X} + V\frac{\partial U}{\partial Y} = -\frac{\partial P}{\partial X} + \frac{1}{Re}\left(\frac{\partial^2 U}{\partial X^2} + \frac{\partial^2 U}{\partial Y^2}\right), \tag{4.6}$$

$$U\frac{\partial V}{\partial X} + V\frac{\partial V}{\partial Y} = -\frac{\partial P}{\partial Y} + \frac{1}{Re}\left(\frac{\partial^2 V}{\partial X^2} + \frac{\partial^2 V}{\partial Y^2}\right) + \frac{Gr}{Re^2}\theta, \tag{4.7}$$

$$U\frac{\partial \theta}{\partial X} + V\frac{\partial \theta}{\partial Y} = \frac{1}{Re\,\mathrm{Pr}}\left(\frac{\partial^2 \theta}{\partial X^2} + \frac{\partial^2 \theta}{\partial Y^2}\right). \tag{4.8}$$

with the boundary conditions:
at the heated bottom wall : $U = 0$, $V = 0$, $\theta = 1$,
at the inclined left and right walls: $U = 0$, $V = 0$, $\theta = 0$,
at the top wall: $U = 1$, $V = 0$, $\dfrac{\partial \theta}{\partial Y} = 0$.

We use the following change of variables:
$X = \dfrac{x}{L}$, $Y = \dfrac{y}{L}$, $U = \dfrac{u}{U_0}$, $V = \dfrac{v}{U_0}$, $\theta = \dfrac{T - T_c}{T_h - T_c}$, $P = \dfrac{p}{\rho U_0^2}$, where X, Y, U, V,θ,P are the dimensionless form of x, y, u, v, T and p respectively.
$Pr = \dfrac{\nu}{\alpha}$ is the Prandtl number, $Re = \dfrac{U_0 L}{\nu}$ is the Reynolds number, and $Gr = \dfrac{g\beta L^3(T_h - T_c)}{\nu^2}$ is the Grashof number. $Ri = Gr/Re^2$ is the Richardson number. If $Ri \ll 1$, the forced convection is dominant while if $Ri \gg 1$, then natural convection is dominant. For problems with $Ri \sim 1$, the natural convection effects are comparable to the forced convection effects.

Now, stream-function vorticity formulation is used to solve the problem. The stream-function $\psi(X, Y)$ is defined in such a way that it satisfies the continuity equation. It is defined as

$$U = \frac{\partial \psi}{\partial Y}, \qquad V = -\frac{\partial \psi}{\partial X}$$

and vorticity $\zeta(X,Y)$ as $\zeta = \dfrac{\partial V}{\partial X} - \dfrac{\partial U}{\partial Y}$.

In terms of stream-function and vorticity, the above equations (4.5), (4.6), (4.7) and (4.8) can be written as

$$-\frac{\partial^2\psi}{\partial X^2} - \frac{\partial^2\psi}{\partial Y^2} = \zeta, \tag{4.9}$$

$$-\frac{\partial^2\zeta}{\partial X^2} - \frac{\partial^2\zeta}{\partial Y^2} + URe\frac{\partial\zeta}{\partial X} + VRe\frac{\partial\zeta}{\partial Y} = \frac{Gr}{Re}\frac{\partial\theta}{\partial X}, \tag{4.10}$$

$$-\frac{\partial^2\theta}{\partial X^2} - \frac{\partial^2\theta}{\partial Y^2} + URe\,\mathrm{Pr}\,\frac{\partial\theta}{\partial X} + VRe\,\mathrm{Pr}\,\frac{\partial\theta}{\partial Y} = 0. \tag{4.11}$$

Nusselt number (Nu) is the ratio of convective and conductive heat transfer normal to the boundary. The heat transfer coefficient in terms of local Nusselt number (Nu) is defined as:

$$Nu = -\frac{\partial\theta}{\partial\bar{N}}, \tag{4.12}$$

where $\bar{N}$ is the non-dimensional normal to the boundary.

4.2 Discretization method for the governing equations

The shape of the trapezoidal cavity is smoothly mapped into a unit square by the following transformation [54] :

$$\xi = \frac{DY + CX - CD}{2(DY + C\sqrt{3} - CD)} \text{ and } \eta = \frac{Y}{C} \text{ where } D < \sqrt{3},$$

so that the geometry in the computational domain becomes a unit square with lower left corner as $(0,0)$. Here ξ and η are the coordinates in the computational region, X and Y are the coordinates in the physical region. C denotes the vertical height of the trapezoidal cavity and the values of C are considered here as $1, 2$ and 3, whereas D relates to the width of the cavity at the bottom wall and the values of D considered are $1/\sqrt{3}, 1.5/\sqrt{3}$ and $2/\sqrt{3}$.

In order to solve this mixed convection problem in a trapezoidal cavity, stream-function vorticity formulation of the governing equations is considered. The governing equations (4.11), (4.10) and (4.9) are of the type

$$a\frac{\partial^2\phi}{\partial x^2} + g\frac{\partial^2\phi}{\partial x\partial y} + b\frac{\partial^2\phi}{\partial y^2} + c\frac{\partial\phi}{\partial x} + d\frac{\partial\phi}{\partial y} + r\phi = \chi + l_1\frac{\partial\epsilon_1}{\partial x} + l_2\frac{\partial\epsilon_1}{\partial y} + l_3\frac{\partial\epsilon_2}{\partial x} + l_4\frac{\partial\epsilon_2}{\partial y} \tag{4.13}$$

considered in Chapter 2. For the equation (4.11), $a = -1$, $b = -1$, $g = 0$, $c = URePr$, $d = VRePr$, $r = 0$, $\chi = 0$, $l_1 = 0$, $l_2 = 0$, $l_3 = 0$, $l_4 = 0$ and $\phi = \theta$.
Using the above mentioned transformation, equation (4.13) becomes

$$a_1\frac{\partial^2\hat{\phi}}{\partial\xi^2} + b_1\frac{\partial^2\hat{\phi}}{\partial\eta^2} + g_1\frac{\partial^2\hat{\phi}}{\partial\xi\partial\eta} + c_1\frac{\partial\hat{\phi}}{\partial\xi} + d_1\frac{\partial\hat{\phi}}{\partial\eta} + r_1\hat{\phi} = f_1, \tag{4.14}$$

where the coefficients a_1, b_1, g_1, c_1, d_1, r_1, f_1 are calculated using the relations available in equation (2.3) in Chapter 2. After discretization, using the same procedure discussed in Chapter 2 for the time independent case, the equation can be written in algebraic form, as:

$$\sum_{s_1=-1}^{1}\sum_{s_2=-1}^{1} w_{i+s_1,j+s_2}\phi_{i+s_1,j+s_2} = F_{i,j}. \tag{4.15}$$

To solve the algebraic system of equations (4.15), biconjugate gradient stabilized method without preconditioning is used.

Similarly, for equation (4.10), $a = -1$, $b = -1$, $g = 0$, $c = URe$, $d = VRe$, $r = 0$, $\chi = 0$, $l_1 = \dfrac{Gr}{Re}$, $l_2 = 0$, $l_3 = 0$, $l_4 = 0$, $\phi = \zeta$ and $\epsilon_1 = \theta$ and for equation (4.9), $a = -1$, $b = -1$, $g = 0$, $c = 0$, $d = 0$, $r = 0$, $\chi = \zeta$, $l_1 = 0$, $l_2 = 0$, $l_3 = 0$, $l_4 = 0$ and $\phi = \psi$.
Equations (4.10) and (4.9) are solved following the similar discretizations and solution procedures.

The equations are solved in the computational plane on a 41×41 grid as this grid is verified to be sufficient to produce grid independent results for this problem. Numerical results obtained are transformed back into the physical domain for the purpose of discussion.

4.3 Results and discussion

4.3.1 Validation of Results

In order to validate the scheme, the lid driven cavity problem is solved in the trapezoidal cavity where the top lid is moving with a constant velocity and all other walls are at no-slip conditions. The results of this problem are compared with the existing results [54] of the same problem. Let (X_c, Y_c) be the location of the primary eddy with the stream-function value ψ_c. Comparisons are performed with the ψ_c values and their corresponding locations for different Reynolds numbers. Table 4.1 shows the compared results and a sufficiently good agreement of the results is seen.

Table 4.1: *Comparison of the location*(X_c, Y_c) *of the primary eddy with the stream function value* ψ_c *between the present scheme and [54]*

Re	(X_c, Y_c) Present	(X_c, Y_c)[54]	ψ_c Present	ψ_c[54]
1	(1.73205, 2.4)	(1.747, 2.382)	0.266732	0.267
50	(2.10011, 2.325)	(2.110, 2.319)	0.275846	0.276
100	(2.01495, 2.175)	(2.023, 2.193)	0.289212	0.290
200	(1.9399, 2.1)	(1.907, 2.105)	0.299649	0.305

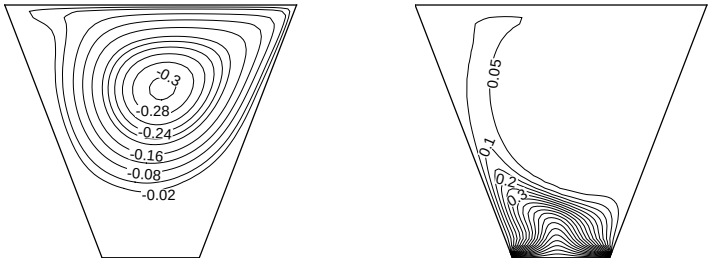

Figure 4.2: Streamline and isotherm contours for Ri=0.1, Pr=0.71, Gr=10000 ($C = 3, D = 2/\sqrt{3}$)

For this problem, the following ranges of values of different parameters are chosen and their effects are discussed in terms of figures. Richardson number Ri varies from $0.1-10$, Grashof number Gr varies from $1000-100000$ and Prandlt numbers used for results are 0.71 and 7.

Figs (4.2)-(4.5), show the effects of Richardson number Ri (by changing its values such as $Ri = 0.1, 1, 5, 10$) on velocity and temperature distributions for fixed $Gr = 10000$ and $Pr = 0.71$.

Fig(4.6), Fig(4.3) and Fig(4.7) represent the the streamlines and isotherm contours for fixed $Ri = 1$, $Pr = 0.71$ where Gr varies from 1000 to 100000.

Fig 4.6) and Fig(4.8 show the streamlines and isotherm contours for $Gr = 1000$, $Ri = 1$ when the values of Pr are 0.71 and 7 respectively.

Figs 4.9-4.14 represent the streamlines and isotherm contours for different Richardson number and Grashof number for Pr=0.71 for trapezoidal cavities where the vertical

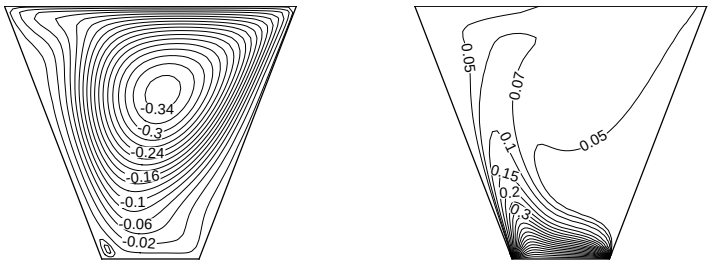

Figure 4.3: Streamline and isotherm contours for Ri=1, Pr=0.71, Gr=10000 ($C = 3, D = 2/\sqrt{3}$)

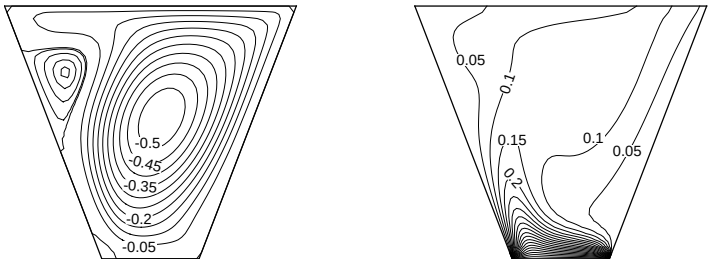

Figure 4.4: Streamline and isotherm contours for Ri=5, Pr=0.71, Gr=10000 ($C = 3, D = 2/\sqrt{3}$)

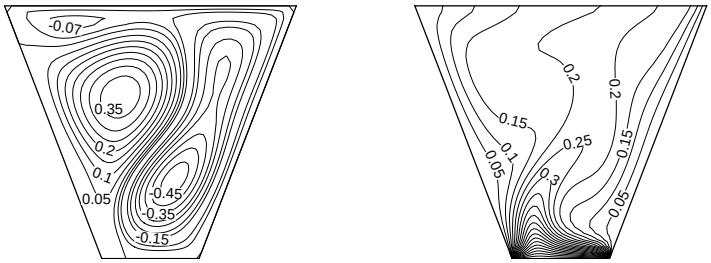

Figure 4.5: Streamline and isotherm contours for Ri=10, Pr=0.71, Gr=10000 ($C = 3, D = 2/\sqrt{3}$)

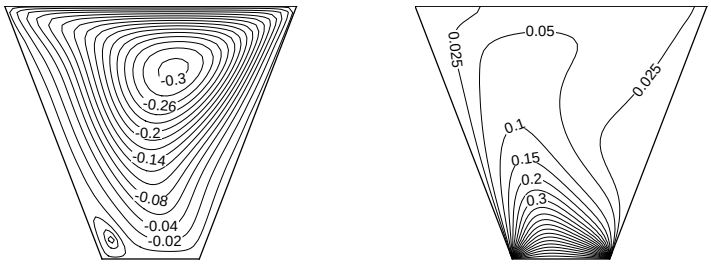

Figure 4.6: Streamline and isotherm contours for Ri=1, Pr=0.71, Gr=1000 ($C = 3, D = 2/\sqrt{3}$)

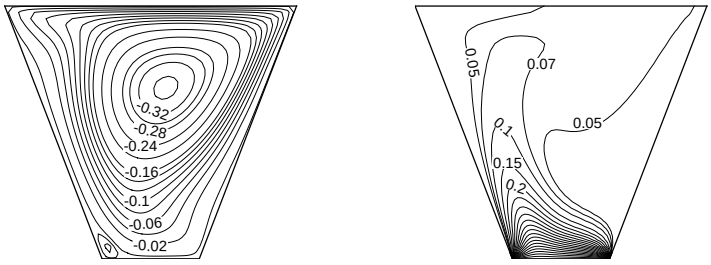

Figure 4.7: Streamline and isotherm contours for Ri=1,Pr=0.71,Gr=5000 ($C = 3, D = 2/\sqrt{3}$)

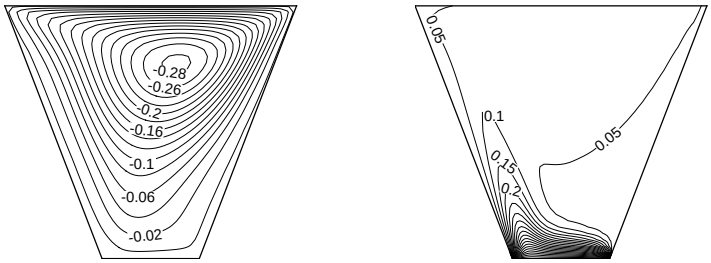

Figure 4.8: Streamline and isotherm contours for Ri=1,Pr=7,Gr=1000 ($C = 3, D = 2/\sqrt{3}$)

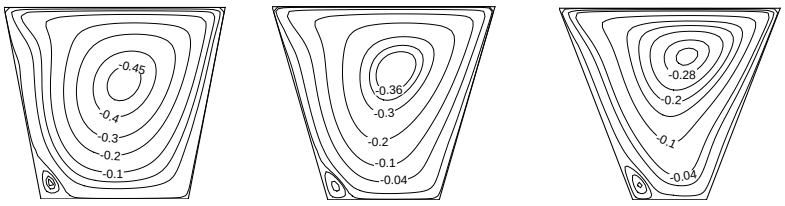

Figure 4.9: Streamline contour for cavities having bottom of different widths of the bottom wall for Gr=1000 and Ri=1 ($C = 3, D = 1/\sqrt{3}, 1.5/\sqrt{3}, 2/\sqrt{3}$)

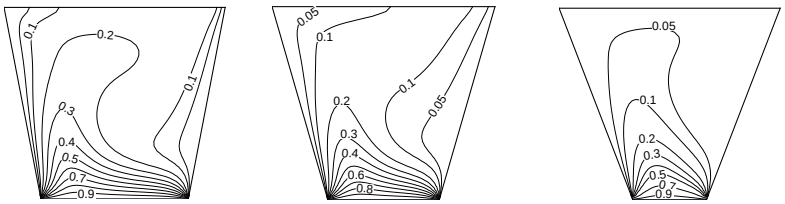

Figure 4.10: Isotherm contour for cavities having bottom of different widths of the bottom wall for Gr=1000 and Ri=1 ($C = 3, D = 1/\sqrt{3}, 1.5/\sqrt{3}, 2/\sqrt{3}$)

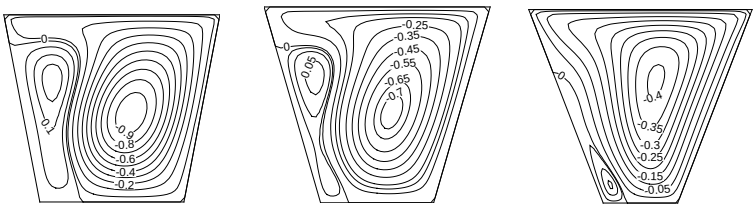

Figure 4.11: Streamline contour for cavities having bottom of different widths for Gr=1000 and Ri=10 ($C = 3, D = 1/\sqrt{3}, 1.5/\sqrt{3}, 2/\sqrt{3}$)

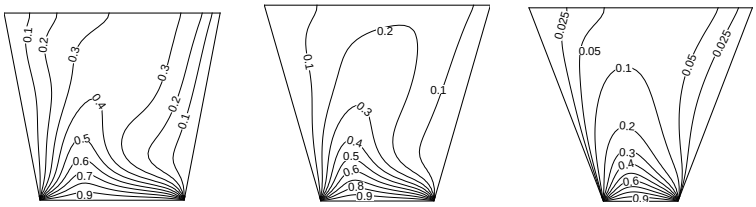

Figure 4.12: Isotherm contour for cavities having bottom of different widths for Gr=1000 and Ri=10 ($C = 3, D = 1/\sqrt{3}, 1.5/\sqrt{3}, 2/\sqrt{3}$)

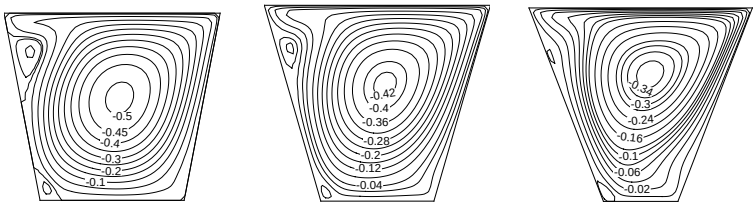

Figure 4.13: Streamline contour for cavities having bottom of different widths for Gr=10000 and Ri=1 ($C = 3, D = 1/\sqrt{3}, 1.5/\sqrt{3}, 2/\sqrt{3}$)

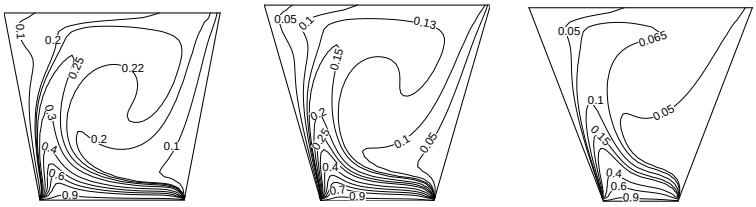

Figure 4.14: Isotherm contour for cavities having bottom of different widths for Gr=10000 and Ri=1 ($C = 3, D = 1/\sqrt{3}, 1.5/\sqrt{3}, 2/\sqrt{3}$)

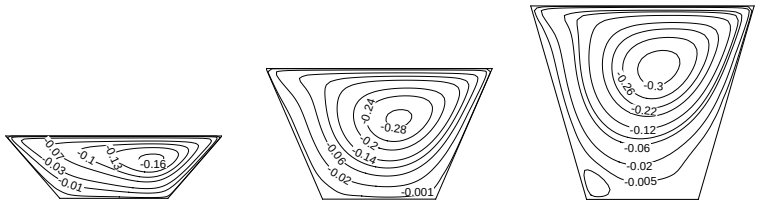

Figure 4.15: Streamline contour for different height for Gr=1000 and Ri=0.1 ($C = 1, 2, 3, D = 1.5/\sqrt{3}$)

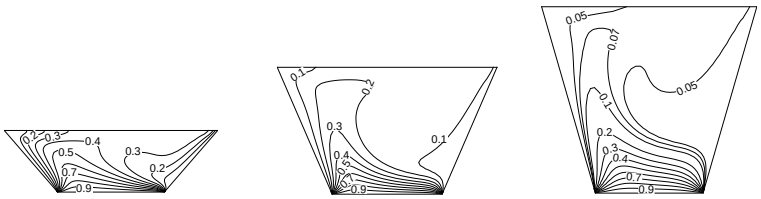

Figure 4.16: Isotherm contour for different height for Gr=1000 and Ri=0.1 ($C = 1, 2, 3, D = 1.5/\sqrt{3}$)

height is fixed but the width of the bottom wall varies.

Figs 4.15-4.18 represent effects of Ri for $Gr = 1000$, $Pr = 0.71$ where the lengths of the horizontal walls are fixed but the vertical height changes.

4.3.2 Effects of Richardson number,Ri

The value of the Richardson number, $Ri = \dfrac{Gr}{Re^2}$ provides a measure of the importance of buoyancy driven natural convection relative to the lid driven forced convection. When the buoyancy effects are relatively small, $Ri < 1$, the gross flow features are similar to the comparable values of Re. The effects of Ri can be seen from Figs 4.2, 4.3, 4.4 and 4.5. The main circulation fills almost the entire cavity generated by the movement of the top wall. Minor cells are visible near the bottom left corner. The streamlines and isotherms indicates that the hydrodynamic and thermal boundary layers are not developed fully at low Richardson number. The isothermal lines are mostly undistorted except the large recirculating area inside the cavity at low Richardson number. In the large recirculating

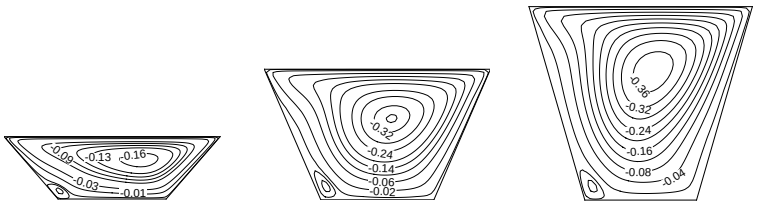

Figure 4.17: Streamline contour for different height of the trapezoid for Gr=1000 and Ri=1 ($C = 1, 2, 3, D = 1.5/\sqrt{3}$)

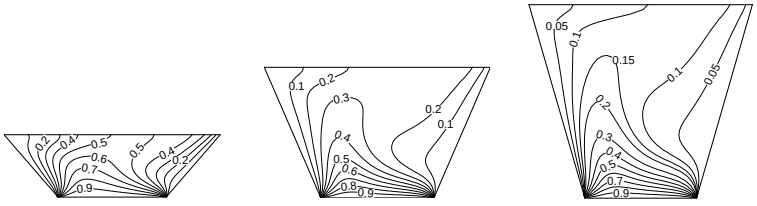

Figure 4.18: Isotherm contour for different height for Gr=1000 and Ri=1 ($C = 1, 2, 3, D = 1.5/\sqrt{3}$)

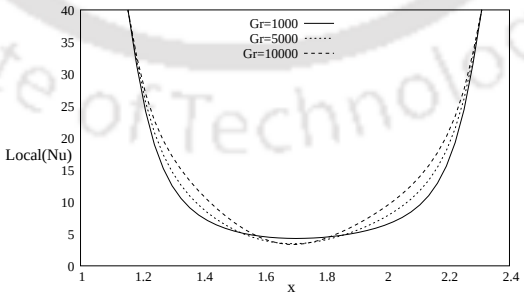

Figure 4.19: Variation of local Nusselt number at the bottom boundary for Ri=0.1 and different Gr

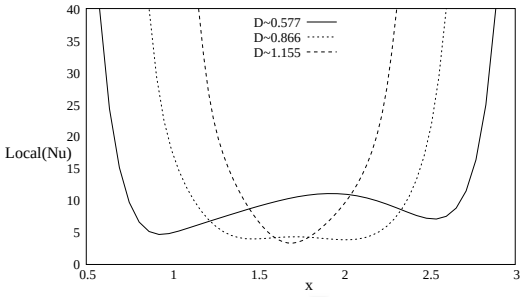

Figure 4.20: Variation of local Nusselt number at the bottom boundary for Ri=0.1 and Gr=1000 with different width of the bottom boundary

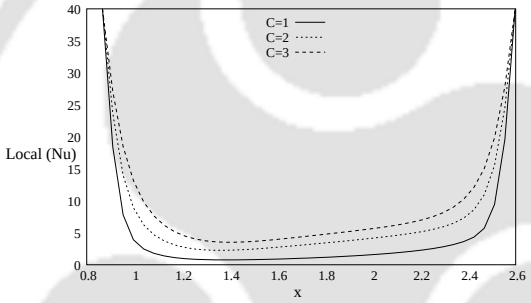

Figure 4.21: Variation of local Nusselt number at the bottom boundary for Ri=1 and Gr=1000 with different height of the cavity

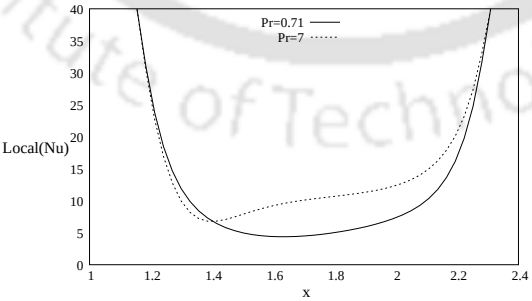

Figure 4.22: Variation of local Nusselt number at the bottom boundary for Ri=1 and Gr=1000 with Pr=0.71 and Pr=7

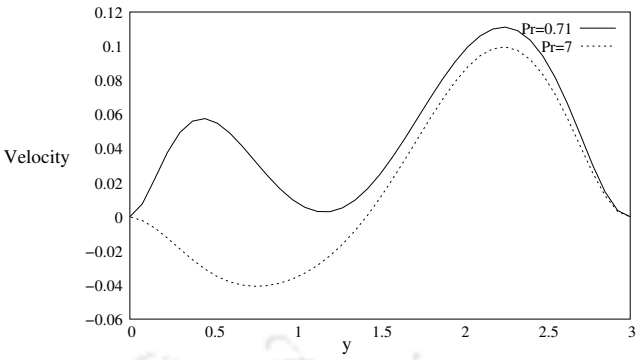

Figure 4.23: Variation of centerline velocity for Ri=1 and Gr=1000 with Pr=0.71 and Pr=7

zone, temperature gradients are very weak. This implies that, due to the vigorous actions of the mechanically driven circulations, fluids are well mixed. Consequently, temperature differences in much of this interior region are very small. When $Ri > 1$, natural convection begins to dominate the forced convection. The buoyancy assists the core flow and thus the convection current becomes much more stronger with increasing Richardson number. As Richardson number increases, the main circulation occupies the whole cavity and it becomes more symmetrical inside the cavity. From the isothermal plots, one can see that as the Richardson number increases, the isothermal lines become more and more denser at the inclined cold walls. The crowded isothermal lines indicate that the thermal boundary layers are developed along the hot wall and cold walls.

4.3.3 Effects of Grashof number, Gr

Since $Ri = \dfrac{Gr}{Re^2}$, Gr is square proportional to the Reynolds number Re for fixed Ri. Gr increases the buoyancy force. As buoyancy force is increased, the heat transfer rate becomes very high. As Gr increases, from Fig 4.6, Fig 4.7 and Fig 4.3, it may be seen that strength of the streamlines increases towards the center of the primary cell. At $Gr = 1000$, it is seen that a minor cell is formed at the bottom left corner of the cavity with the primary cell. As Gr increases to 10000, the minor cell at the bottom left corner almost disappears and the primary cell occupies the whole cavity. From the isotherm contours, it is seen that with the increase of Gr, thermal boundary layers are developed near the inclined cold walls and hot bottom wall.

4.3.4 Effects of Prandtl number, Pr

Prandtl number is the ratio of momentum diffusivity and thermal conductivity. Fig 4.6 and Fig 4.8 represent the streamlines and isotherm contours for Prandtl numbers $Pr = 0.71$ and $Pr = 7$ respectively, for fixed $Gr = 1000$ and $Ri = 1$. It may be seen that for $Pr = 0.71$, a minor cell appears near the bottom left corner of the cavity along with the primary cell but when Prandtl number increases to $Pr = 7$, the minor cell disappears and with the increase of Prandtl number, the magnitude of streamline contours become lesser. This could be due to the increase in viscous force leading to retardation in the fluid velocity. The isotherm contours become more dense along the cold and hot walls for $Pr = 7$ compared to $Pr = 0.71$ and heat transfer rate increases.

4.3.5 Effects of bottom width with fixed vertical length of the trapezoidal cavity

Figs 4.9-4.14 represent the streamlines and isotherm contours for different Richardson number and Grashof number for fixed Prandtl number $Pr = 0.71$ in trapezoidal cavities where the vertical heights of the cavities are fixed but bottom widths vary. Three different cases are considered in this study. Fig 4.9 and Fig 4.10 show the streamlines and isotherm contours respectively for $Gr = 1000$ and $Ri = 1$. Fig(4.11) and Fig 4.12 show the streamlines and isotherm contours for $Gr = 1000$ and $Ri = 10$. Fig 4.13 and Fig 4.14 show these contour lines for $Gr = 10000$ and $Ri = 1$. The streamlines in Fig 4.9 for $Gr = 1000$, $Ri = 1$ show that a primary cell appears that covers almost the whole of the cavity with a minor cell at the bottom left corner. With the increase of the width of the hot bottom wall, magnitudes of the streamlines increase, which implies that the circulations become stronger. Also from the isotherm contours, it may be seen that the heat transfer rate increases with the increase in width of the bottom wall. When Ri increases to 10, the streamlines show that the minor cells get enlarged and the center of the primary cells move towards the bottom wall slightly (Fig 4.11) from its previous position at $Ri = 1$ (Fig 4.9). As width increases, the position of the minor cell changes, the center of the minor cell tends towards the top of the cavity (Figs 4.9, 4.11,4.13). As Gr increases to 10000, the two minor cells become prominent with the increase of the width and also the strength of the primary cell increases. With the increase in width at the bottom wall, fluid temperature in the whole cavity goes up. When the width of the bottom wall is less, as the contact area between the hot wall and the fluid is reduced, over all temperature in the cavity goes down. This is clear from the isotherm contours.

4.3.6 Effects of vertical height of the trapezoidal cavity

Figs 4.15 and 4.16 show the streamlines and isotherms for different vertical heights set by $C = 1, 2$ and 3 for $Ri = 0.1$, $Gr = 1000$ and $Pr = 0.71$. There is only one primary convective cell for $C = 1$ and 2, whereas for $C = 3$, a secondary cell appears at the bottom left corner of the enclosure along with the primary cell. The magnitude of the streamline contours also increases with the increase of the vertical height C. This may be the reason that when the height is minimum, the boundary layer affects the velocity of the fluid much than the case when the height is more. Similarly, Fig 4.17 and 4.18 show the contours for these vertical heights for $Ri = 1$ for $Gr = 1000$ and $Pr = 0.71$. Here, the streamline contours show that for all three vertical heights, a secondary cell appears at the left bottom corner along with the primary cell but the flow becomes stronger with the increase in height of the cavity. When the height of the vertical wall increases, the volume of the cavity increases. So, the same amount of heat gets distributed throughout the cavity, which in turn reduce the overall temperature inside the cavity, which is clear from the isotherm contours.

4.3.7 Heat transfer rate at the bottom boundary

Heat transfer rates at the bottom boundary of the cavity are discussed for different situations in the form of local Nusselt number and results are presented in Figs 4.19-4.23. A general trend in Nusselt number variation noticed in these figures is that near the vertical walls its values are much higher compared to that in the middle part of the bottom boundary and makes a parabolic shape. The reason could be that the vertical walls are cooler and the bottom one is hotter. Because of large temperature difference near the vertical walls, the heat transfer rates are quite high and as profiles move towards the middle, the temperature difference gradually reduces so as the Nusselt number. In Fig 4.19 the effects of Grashof number on the local Nusselt number for $Ri = 0.1$ and $Pr = 0.71$ at the bottom hot wall are observed. The local Nusselt number near the corner points is high and as it comes to the center of the bottom wall, the Nusselt number decreases and a parabolic type of profile can be found. With the increase of Grashof number, the local Nusselt number near the center of the bottom wall decreases. Fig 4.20 shows effects of the width of the bottom wall on the local heat transfer rate at that wall. At $D = 1/\sqrt{3}(\approx 0.577)$ (for a wider cavity), the heat transfer rate along the bottom wall shows a bimodal trend. As D increases ($0.577 \rightarrow 0.866 \rightarrow 1.155$), the bimodal trend gradually becomes a unimodal parabolic profile at $D = 2/\sqrt{3}(\approx 1.155)$.

From Fig 4.21, it is observed that with the increase of the vertical heights of the cavity the local Nusselt number towards the center of the bottom hot wall increases. Fig 4.22 shows that with the increase of Prandtl number from 0.71 to 7, the local heat transfer increases. Fig 4.23 shows the centerline velocity along y direction. It shows that the centerline velocity for $Pr = 0.71$ is higher than that for $Pr = 7$.

4.4 Conclusions

In this chapter, a mixed convection problem in a trapezoidal cavity is considered. The bottom wall is heated uniformly while the inclined side walls are cold and the moving top wall is adiabatic. The proposed fourth order accurate HOC finite difference scheme is used to solve the problem. The Grashof number Gr varies from 1000 to 100000, Prandtl numbers are considered as 0.71 and 7. Some significant observations of this study are listed as:

(1) Local heat transfer rate at the edges of the heated wall is very high and a parabolic type profile is observed for the Nusselt number along the bottom wall.

(2) With the increase of Gr, heat transfer rate increases.

(3) With the increase of vertical height of the trapezoidal cavity, enhancement in the local heat transfer rate is observed.

(4) At $D = 1/\sqrt{3}$, the heat transfer rate along the bottom wall shows a bimodal trend. As D increases, the bimodal trend gradually becomes a unimodal parabolic profile at $D = 2/\sqrt{3}$.

5

Mixed Convection Problem in a vented cavity

The study of natural and mixed convection in an enclosure is important from theoretical as well as practical point of view. Thermal design of building, energy storage systems, solar collectors, circulation of fluid in electronic equipment are well known examples of applications of convection.

Effects of mixed convective flows in enclosures are investigated by many researchers using analytical, experimental and numerical methods. An analytical solution of the mixed convection heat transfer in tall cavities is presented by Arpaci and Larsen [3]. Cha and Jaluria [11, 33] considered mixed convection in a long horizontal cavity where inlet and outlet are placed on the vertical walls to understand heat energy extraction process in a solar pond.

Kumar and Yuan [41] studied a laminar, two-dimensional mixed convection flow in a rectangular enclosure with inlet and outlet ports. Papanicolaou and Jaluria [69, 71, 73] investigated mixed convection in a cavity with a localized heat source. Papanicolaou and Jaluria [69, 71] reported that flow patterns generally consisted of recirculating cells due to buoyancy forces generated by the heat source. An improvement in cooling can also be obtained when the outlet flow opening is placed near the bottom of the vertical wall. The results obtained in an inclined channel for turbulent flow showed that the best performance in heat transfer was observed when the channel was in a vertical location and this was investigated by Papanicolaou and Jaluria [73] .

Hsu et al. [27] studied numerically the mixed convection in a rectangular enclosure with a dividing partition . The simulation was carried out for wide range of Reynolds and Grashof numbers. It was found that the flow phenomena and the heat transfer of the enclosure depended on the location and height of the divider. Choi and Ortega [13] studied the mixed convection in an inclined channel and they observed that the best performance in heat transfer occurred when the channel was in a vertical location.

Experimental investigations of mixed convective flows have also been performed by many researchers. Gau et al. [20] studied a mixed convection flow experimentally, in a horizontal rectangular channel with side heating whereas Joye [34] made an experimental study on convective heat transfer with opposing flow inside a vertical tube.

Raji and Hasnaoui [82] numerically studied mixed convection heat transfer in a ventilated cavity subjected to a uniform heat flux from a side using the Navier-Stokes equations with Boussinesq approximation. Flow fields, temperature fields, and heat transfer rates are examined for different values of Rayleigh (Ra) and Reynolds (Re) numbers $10^3 \leq Ra \leq 5 \times 10^6$ and $5 \leq Re \leq 5,000$. They considered air as the working fluid. Two types of configurations were considered, BB (inlet is at the bottom portion of the left vertical wall and outlet is also at the bottom portion of the right vertical wall) and BT (inlet is at the bottom part of the left side of the cavity and outlet is at the top part of the right side of the cavity) and finally concluded that BB configuration was not useful for heat evacuation. Later, they [83, 84] reported the results of a numerical study of mixed convection of air in a rectangular cavity, including radiation for $1000 \leq Ra \leq 5,1000000$ and $5 \leq Re \leq 5,000$.

A control-volume finite-element method, using triangular elements, was used to study transient mixed convection in an air-cooled cavity by Omri and Nasrallah [62], for $0.1 \leq Ri \leq 18$, $10 \leq Re \leq 500$, including radiation.

Later on, Singh and Sharif [95] extended their works by considering six types of configurations of the inlet and outlet of a differentially heated rectangular enclosure whereas the previous work was limited to only two different configurations of inlet and outlet. They concluded that the configuration with the inlet near the bottom and the outlet near the top of the opposite vertical wall, the forced and natural convection assist each other in the heat removal process, producing more effective cooling.

Mixed convection in an open cavity with a heated wall bounded by horizontal adiabatic walls was studied numerically by Manca et al. [52]. Three different cases of mixed convection in a channel with an open cavity for various ratios of channel opening and cavity height were solved and the range of governing parameters were $0.1 \leq Ri \leq 100$, and $Re = 100$ and 1000.

Rahman et al. [80] studied the effects of Prandtl, Richardson and Reynolds numbers on the heat transfer characteristics of laminar mixed convection. The influence of the location of the inlet on the surface heat transfer for a range of Richardson number, Prandtl number and Reynolds number in a square cavity was analyzed.

Mahmodi et al. [49] studied mixed convection flow and temperature fields in a vented square cavity subjected to an external copper water nanofluid numerically. In order to

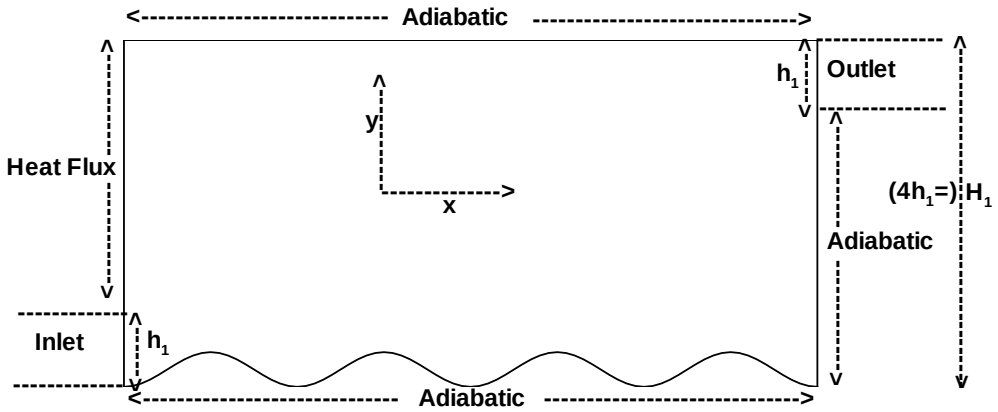

Figure 5.1: Geometrical sketch of the problem

investigate the effects of inlet and outlet positions in the vented cavity, four different types of configurations were considered in this work. It was concluded that the presence of nano particles was more effective in BT configuration in comparison with other configurations (TT, TB, BB) where TT represents the situation when the inlet is at the top portion of the left side and outlet is at also at the top portion of the right side, for TB, the inlet is at the top portion of the left vertical wall and outlet is at the bottom portion of the right vertical wall.

In this chapter, the mixed convection is studied in a rectangular enclosure where the bottom wall of the enclosure is considered to be wavy. The inlet is situated at the bottom part of the vertical wall where as the outlet is fixed at the top of the opposite vertical wall of the enclosure. Openings of the inlet and the outlet are kept as 1/4-th time of the wall height of the enclosure. A colder fluid enters the enclosure through the inlet and a constant heat flux is applied at the portion of the wall above inlet at the left vertical wall. The other walls are adiabatic.

5.1 Problem and the governing equations

A schematic representation of the cavity is shown in Fig 5.1. This is a rectangular enclosure with its left wall equipped with a constant heat flux, whereas all other walls are considered to be adiabatic. The cavity presented in this figure is subjected to an external cold flow which enters the cavity through the bottom of the heated left vertical wall and leaves the cavity through the top of the opposite vertical wall. Bottom wall is wavy.

All the physical properties of the fluid are considered to be constant except the density

in the buoyancy term, which obeys Boussinesq approximation. It is assumed that the third dimension of the cavity is large enough so that the flow and heat transfer can be treated as two-dimensional. Governing equations for this problem can be expressed as:

$$\frac{\partial u}{\partial x} + \frac{\partial v}{\partial y} = 0, \tag{5.1}$$

$$u\frac{\partial u}{\partial x} + v\frac{\partial u}{\partial y} = -\frac{1}{\rho}\frac{\partial p}{\partial x} + \nu\left(\frac{\partial^2 u}{\partial x^2} + \frac{\partial^2 u}{\partial y^2}\right), \tag{5.2}$$

$$u\frac{\partial v}{\partial x} + v\frac{\partial v}{\partial y} = -\frac{1}{\rho}\frac{\partial p}{\partial y} + \nu\left(\frac{\partial^2 u}{\partial x^2} + \frac{\partial^2 u}{\partial y^2}\right) + g\beta(T - T_c), \tag{5.3}$$

$$u\frac{\partial T}{\partial x} + v\frac{\partial T}{\partial y} = \alpha\left(\frac{\partial^2 T}{\partial x^2} + \frac{\partial^2 T}{\partial y^2}\right), \tag{5.4}$$

with the boundary conditions:
$u = U_0$, $v = 0$ and $T = T_c$ at the inlet,
$\frac{\partial u}{\partial x} = 0$, $\frac{\partial v}{\partial x} = 0$, $\frac{\partial T}{\partial x} = 0$ at the outlet,
$u = 0$, $v = 0$ and $q = -k_c\frac{\partial T}{\partial x}$ along the heated wall,
$u = 0$, $v = 0$ and $\frac{\partial T}{\partial x} = 0$ along the vertical adiabatic wall,
$u = 0$, $v = 0$ and $\frac{\partial T}{\partial \bar{n}} = 0$ along the horizontal adiabatic walls,
where x and y are the distances along the horizontal and vertical directions respectively, u and v are the velocities along the x- and y- directions respectively, T is the temperature, ν and α are the kinematic viscosity and the thermal diffusivity of the fluid respectively, p is the pressure, ρ is the density, g is the acceleration due to gravity, β is the coefficient of volume expansion, k_c is the thermal conductivity, q is the heat flux from the source, $\bar{n}$ is the normal to the boundary.

In order to get the non-dimensional form the governing equations, the following change of variables are used:
$X = \frac{x}{L}$, $Y = \frac{y}{L}$, $U = \frac{u}{U_0}$, $V = \frac{v}{U_0}$, $\theta = \frac{T - T_c}{qL/k_c}$, $P = \frac{p}{\rho U_0^2}$,
$Re = \frac{U_0 L}{\nu}$, $Pr = \frac{\nu}{\alpha}$, $Ra = \frac{g\beta q L^4 Pr}{\nu^2 k_c}$.
The non-dimensional governing equations are:

$$\frac{\partial U}{\partial X} + \frac{\partial V}{\partial Y} = 0, \tag{5.5}$$

$$U\frac{\partial U}{\partial X} + V\frac{\partial U}{\partial Y} = -\frac{\partial P}{\partial X} + \frac{1}{Re}\left(\frac{\partial^2 U}{\partial X^2} + \frac{\partial^2 U}{\partial Y^2}\right), \tag{5.6}$$

$$U\frac{\partial V}{\partial X}+V\frac{\partial V}{\partial Y}=-\frac{\partial P}{\partial Y}+\frac{1}{Re}\left(\frac{\partial^2 V}{\partial X^2}+\frac{\partial^2 V}{\partial Y^2}\right)+\frac{Ra}{RePr}\theta, \tag{5.7}$$

$$U\frac{\partial \theta}{\partial X}+V\frac{\partial \theta}{\partial Y}=\frac{1}{Re\,\mathrm{Pr}}\left(\frac{\partial^2 \theta}{\partial X^2}+\frac{\partial^2 \theta}{\partial Y^2}\right), \tag{5.8}$$

with the boundary conditions:
$U=1$, $V=0$ and $\theta=0$ at the inlet,
$\frac{\partial U}{\partial X}=0$, $\frac{\partial V}{\partial X}=0$, $\frac{\partial \theta}{\partial X}=0$ at the outlet,
$U=0$, $V=0$ and $\frac{\partial \theta}{\partial X}=-1$ along the heated wall,
$U=0$, $V=0$ and $\frac{\partial \theta}{\partial X}=0$ along the vertical adiabatic wall,
$U=0$, $V=0$ and $\frac{\partial \theta}{\partial \bar{N}}=0$ along the horizontal adiabatic walls where $\bar{N}$ is the non-dimensional normal to the boundaries.
Here X and Y are dimensionless coordinates along the horizontal and vertical directions respectively, U and V are the non dimensional velocity components along the $X-$ and $Y-$ directions respectively, θ is the dimensionless temperature, P is the dimensionless pressure, Re is the Reynolds number, Pr is the Prandtl number and Ra is the Rayleigh number.

In order to solve this problem, stream function-vorticity formulation of the governing equations are used to reduce the number of equations to be solved and to get rid of the pressure term, where the stream function ψ is defined as

$$U=\frac{\partial \psi}{\partial Y}, \qquad V=-\frac{\partial \psi}{\partial X}$$

and vorticity ζ as $\zeta=\frac{\partial V}{\partial X}-\frac{\partial U}{\partial Y}$.

The stream function-vorticity $(\psi-\zeta)$ formulation of the governing equations can be expressed as:

$$-\frac{\partial^2 \psi}{\partial X^2}-\frac{\partial^2 \psi}{\partial Y^2}=\zeta, \tag{5.9}$$

$$-\frac{\partial^2 \zeta}{\partial X^2}-\frac{\partial^2 \zeta}{\partial Y^2}+URe\frac{\partial \zeta}{\partial X}+VRe\frac{\partial \zeta}{\partial Y}=\frac{Ra}{RePr}\frac{\partial \theta}{\partial X}, \tag{5.10}$$

$$-\frac{\partial^2 \theta}{\partial X^2}-\frac{\partial^2 \theta}{\partial Y^2}+URe\,\mathrm{Pr}\,\frac{\partial \theta}{\partial X}+VRe\,\mathrm{Pr}\,\frac{\partial \theta}{\partial Y}=0. \tag{5.11}$$

The hydrodynamical boundary conditions are characterized by the impermeability of the rigid boundary and the no-slip of the fluid particles on the boundaries. At the inlet of the cavity $\theta=0$, $U=1$, $V=0$, $\psi=Y$.

We have the stream function $\psi = 0$ on the bottom wall and portion of the right wall below the outlet. For the remaining walls, $\psi = B$ is considered where B is the relative height of the openings, $\frac{h_1}{H_1}$.

The thermal boundary condition for the adiabatic walls is $\frac{\partial \theta}{\partial n} = 0$, where n denotes the outward normal direction to the given wall. At the vertical heated wall, $\frac{\partial \theta}{\partial X} = 1$.
For the boundary conditions of vorticity ζ, it is calculated using the relation

$$-\frac{\partial^2 \psi}{\partial X^2} - \frac{\partial^2 \psi}{\partial Y^2} = \zeta.$$

At the outlet, convective boundary condition is applied for U, V, ψ, ζ and θ.

To measure the heat transfer at a boundary within a fluid, the Nusselt number (Nu), which is the ratio of convective to conductive heat transfer across (normal to) the boundary is calculated.
The heat transfer coefficient in terms of local Nusselt number (Nu) is defined by [27],

$$Nu = \frac{1}{\theta} \tag{5.12}$$

5.2 Discretization method for the governing equations

The transformation applied here to transform this bottom wavy enclosure to a uniform rectangular enclosure is

$$X = \xi \ ,$$
$$Y = \eta + \lambda(1 - \cos(2\pi N\xi))(1 - \eta),$$

where N determines 2 times the number of undulations in the bottom wavy boundary and ξ and η- are the coordinates in the computational region, X and Y- are the coordinates of physical region.

In order to solve this mixed convection problem in a vented cavity, stream-function vorticity formulation of the governing equations is considered. The governing equations (5.11), (5.10) and (5.9) are of the type

$$a\frac{\partial^2 \phi}{\partial x^2} + g\frac{\partial^2 \phi}{\partial x \partial y} + b\frac{\partial^2 \phi}{\partial y^2} + c\frac{\partial \phi}{\partial x} + d\frac{\partial \phi}{\partial y} + r\phi = \chi + l_1\frac{\partial \epsilon_1}{\partial x} + l_2\frac{\partial \epsilon_1}{\partial y} + l_3\frac{\partial \epsilon_2}{\partial x} + l_4\frac{\partial \epsilon_2}{\partial y} \tag{5.13}$$

as considered in Chapter 2. For equation (5.11), $a = -1$, $b = -1$, $g = 0$, $c = URePr$, $d = VRePr$, $r = 0$, $\chi = 0$, $l_1 = 0$, $l_2 = 0$, $l_3 = 0$, $l_4 = 0$ and $\phi = \theta$.
Using the above mentioned transformation, equation (5.13) becomes

$$a_1\frac{\partial^2\hat{\phi}}{\partial\xi^2} + b_1\frac{\partial^2\hat{\phi}}{\partial\eta^2} + g_1\frac{\partial^2\hat{\phi}}{\partial\xi\partial\eta} + c_1\frac{\partial\hat{\phi}}{\partial\xi} + d_1\frac{\partial\hat{\phi}}{\partial\eta} + r_1\hat{\phi} = f_1, \tag{5.14}$$

where the coefficients a_1, b_1, g_1, c_1, d_1, r_1, f_1 are calculated using the relations available in equation (2.3) in Chapter 2. After discretization, using the same procedure followed in Chapter 2 for time independent case, the equation can be written in algebraic form, as:

$$\sum_{s_1=-1}^{1}\sum_{s_2=-1}^{1} w_{i+s_1,j+s_2}\phi_{i+s_1,j+s_2} = F_{i,j}. \tag{5.15}$$

To solve the algebraic system of equations (5.15), biconjugate gradient stabilized method without preconditioning is used.

Similarly, for equation (5.10), $a = -1$, $b = -1$, $g = 0$, $c = URe$, $d = VRe$, $r = 0$, $\chi = 0$, $l_1 = \dfrac{Ra}{RePr}$, $l_2 = 0$, $l_3 = 0$, $l_4 = 0$, $\phi = \zeta$ and $\epsilon_1 = \theta$ and for equation (5.9), $a = -1$, $b = -1$, $g = 0$, $c = 0$, $d = 0$, $r = 0$, $\chi = \zeta$, $l_1 = 0$, $l_2 = 0$, $l_3 = 0$, $l_4 = 0$ and $\phi = \psi$.
Equations (5.10) and (5.9) are solved following the similar discretizations and solution procedures.

The equations are solved in the computational plane on a 41×41 grid as this grid is verified to be sufficient to produce grid independent results for this problem. Numerical results obtained are transformed back into the physical domain for the purpose of discussion. The convergence criterion chosen in this problem is considered as the error is bounded above by 0.5×10^{-4}.

5.3 Comparison of Results:

For comparison of results, a rectangular cavity is considered and mixed convection problem is solved keeping all the parameters same as in [82]. The cavity is heated from the left side of the cavity with a constant heat flux and a laminar horizontal cold jet from the bottom of the heated wall is applied. The fluid leaves the cavity through the top of the opposite vertical wall. The results are compared with the existing results of the mixed convection problem in a rectangular vented cavity [82]. The streamline and isotherm contours of the mixed convection problem in a rectangular vented cavity with Reynolds number ($Re = 10$) and Rayleigh number $Ra = 0$ (Fig 5.2 and 5.3), 10000 (Fig

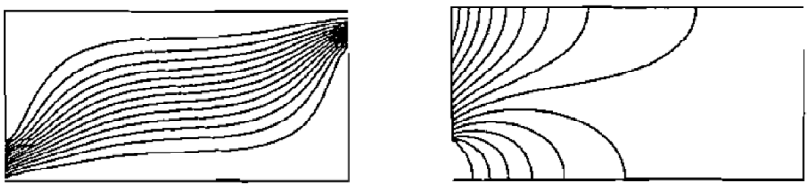

Figure 5.2: Streamline and isotherm contour for Re=10 and Ra=0 of the existing result

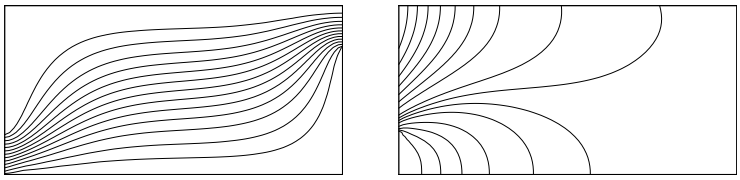

Figure 5.3: Streamline and isotherm contour for Re=10 and Ra=0 of the present result

5.4 and 5.5) and 100000 (Fig 5.6 and 5.7) are compared. It is observed that the results obtained using the proposed scheme are in a good agreement with the results discussed in [82].

5.4 Results and Discussion

The governing equations are solved using the proposed HOC schemes. Results are compared with the already published results. Streamlines and isotherms for $Re = 10$ and

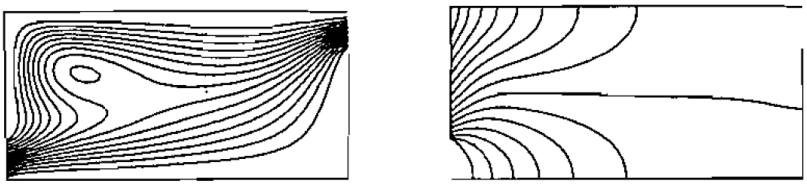

Figure 5.4: Streamline and isotherm contour for Re=10 and Ra=10000 of the existing result

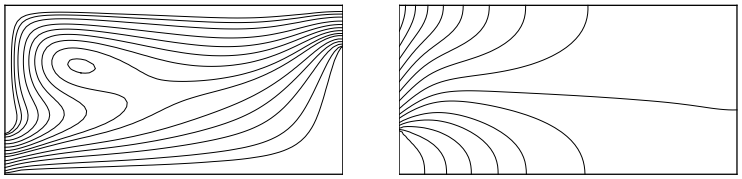

Figure 5.5: Streamline and isotherm contour for Re=10 and Ra=10000 of the present result

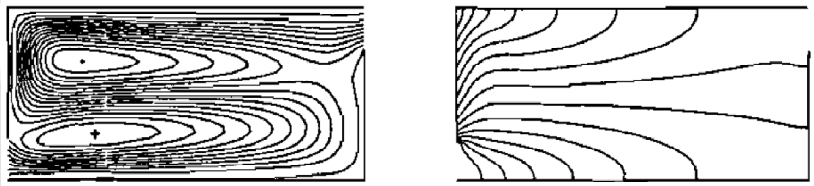

Figure 5.6: Streamline and isotherm contour for Re=10 and Ra=100000 of the existing result

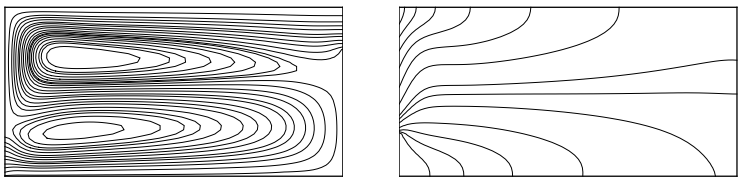

Figure 5.7: Streamline and isotherm contour for Re=10 and Ra=100000 obtained from present result

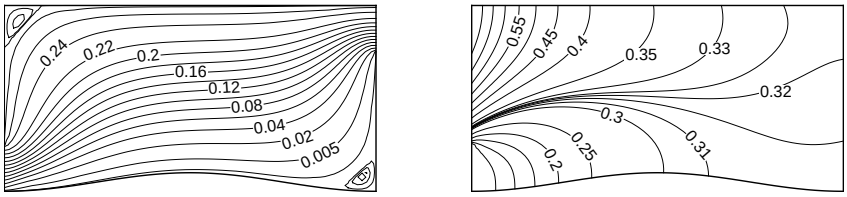

Figure 5.8: Streamline and isotherm contour Re=10 and Ra=0

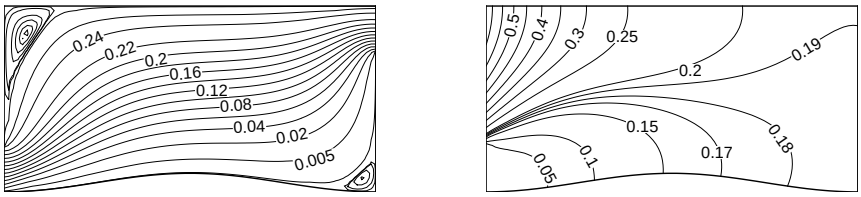

Figure 5.9: Streamline and isotherm contour Re=20 and Ra=0

$Ra = 0, 1000, 100000$, depicted in the Figs 5.3, 5.5 and 5.7 respectively are qualitatively similar to those of Raji and Hasaoui [82]. With the increase of Ra, i.e., the difference between cold and hot walls, the flow becomes complex by forming two vortices in the streamlines patterns and also in isotherms projecting the free convection dominated flow.

Figs 5.8-5.10 show streamlines and isotherms of the vented cavity, where bottom wall is wavy with single bump. Isolines are drawn for different Reynolds numbers (namely $Re = 10, 20, 100$). When natural convection is absent and the flow is governed by forced convection only, one can observe that vortices are formed in the left upper and right lower corners and gradually grow with the increase of Reynolds numbers. Thermal boundary layers are developed near the heated wall with the increase of Re. Two separate temperature zones are slowly formed with higher Re, which is a clear indication of influences of larger vortices.

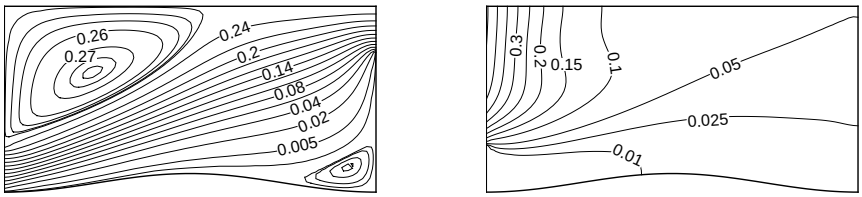

Figure 5.10: Streamline and isotherm contour Re=100 and Ra=0

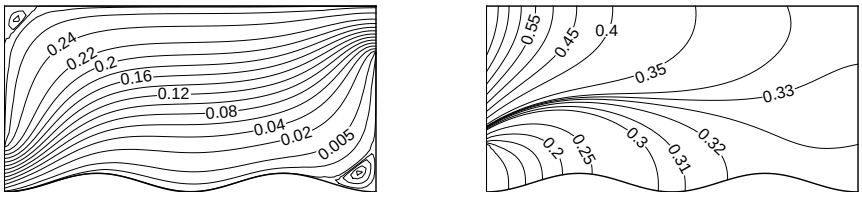

Figure 5.11: Streamline and isotherm contour Re=10 and Ra=0

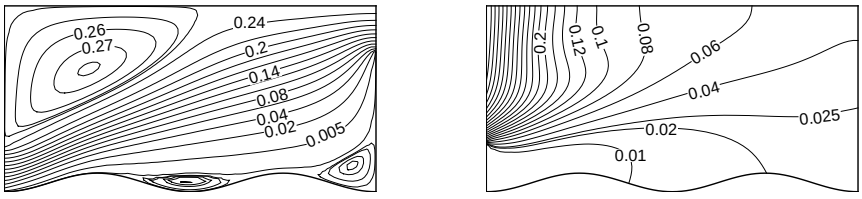

Figure 5.12: Streamline and isotherm contour Re=100 and Ra=0

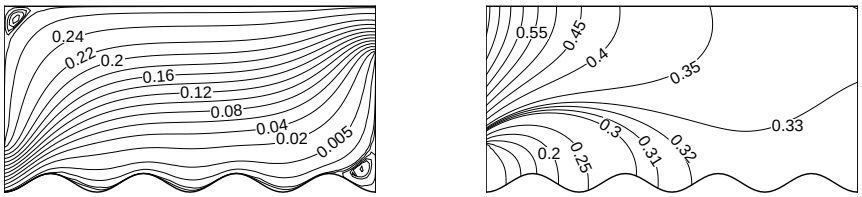

Figure 5.13: Streamline and isotherm contour Re=10 and Ra=0

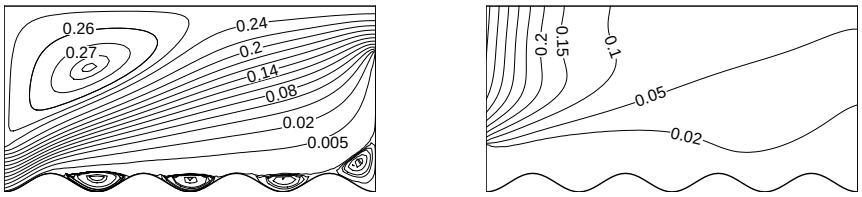

Figure 5.14: Streamline and isotherm contour Re=100 and Ra=0

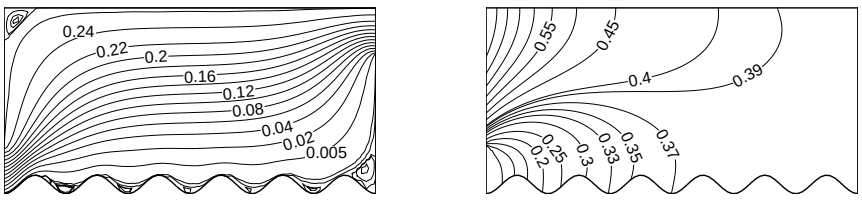

Figure 5.15: Streamline and isotherm contour Re=10 and Ra=0

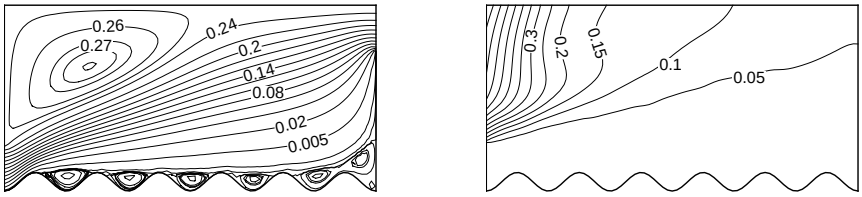

Figure 5.16: Streamline and isotherm contour Re=100 and Ra=0

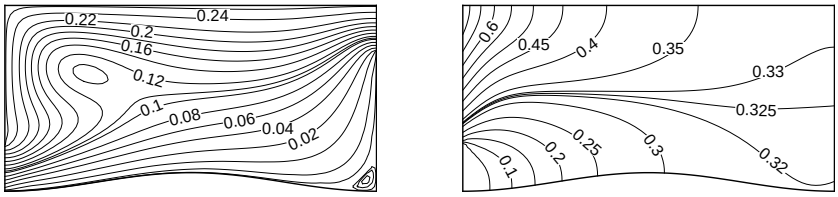

Figure 5.17: Streamline and isotherm contour Re=10 and Ra=10000

Figs 5.11-5.16 show the effects of waviness of the bottom wall on flow phenomena and heat transfer in the vented cavity. There is no significant change in the flow structure in the upper half of the cavity due to multiple waves at the bottom wall, however vortices are formed at each depression of the wavy wall. These depressed (toss) zones behave like dead zone pockets. Heat transfer rate increases with the increase of number waves up to a certain number and after that the rate of heat transfer does not increase even if the number of waviness increases.

Figs 5.17-5.20 show streamlines and isotherms for $Ra = 10000$ and $Re = 10$ for different values of N i.e a mixed convection situation where both forced as well as free convection are present. Notable observation is that there is no vortex at the left upper corner of the cavity but there is a vortex at the right bottom corner of the cavity. With the increase of N, the vortex at the right bottom corner becomes larger. Temperature profiles, i.e., isotherms are also different from the earlier one ($Ra = 0$) due to natural

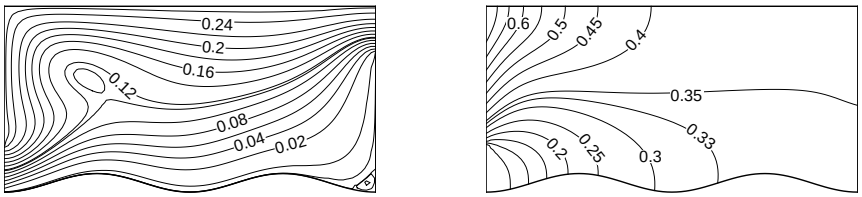

Figure 5.18: Streamline and isotherm contour Re=10 and Ra=10000

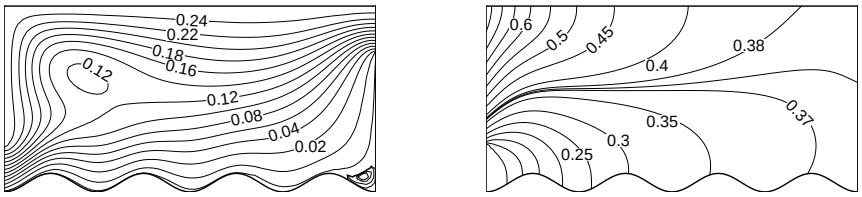

Figure 5.19: Streamline and isotherm contour Re=10 and Ra=10000

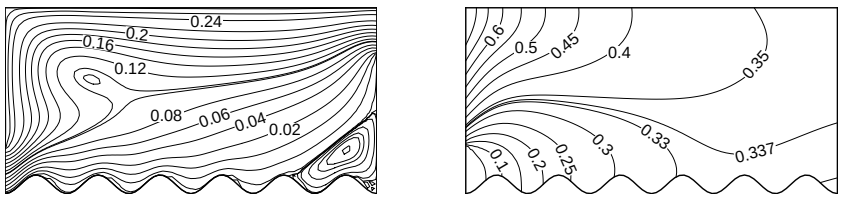

Figure 5.20: Streamline and isotherm contour Re=10 and Ra=10000

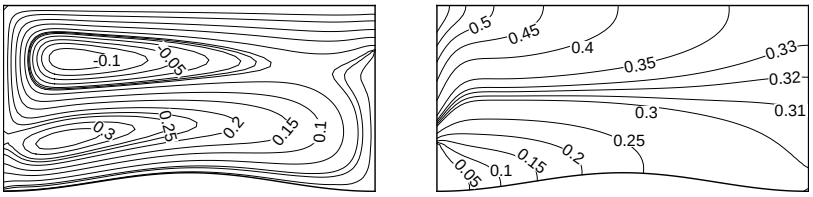

Figure 5.21: Streamline and isotherm contour Re=10 and Ra=100000

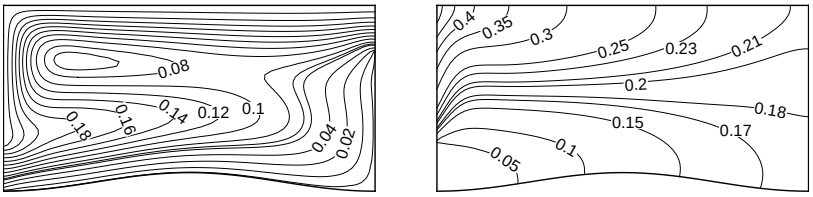

Figure 5.22: Streamline and isotherm contour Re=20 and Ra=100000

convection.

Figs 5.21-5.24 show the streamlines and isotherms for different Re varying from 10 to 200 when $Ra = 100000$ with single wavy bump. For smaller value of Reynolds number, say, $Re = 10$, the natural convection dominates and there is a circulatory motion inside the cavity. Two separate vortices are formed in the middle of the cavity near the hot wall. The flow becomes a natural convection dominated flow combined with the inlet flow which makes two vortices. Hotter fluid moves upward along the hot wall, which is visible from the temperature profile. With an increase in Re, it is noticed that the influence of natural convection is overpowered by forced convection and streamlines as well as isotherms are straightened as circulations due to natural convection are subsided at $Re = 100$. If Re is increased further to $Re = 200$, corner vortices due to fluid motion are formed again and natural convection becomes insignificant, though the overall temperature of the fluid in the cavity increases.

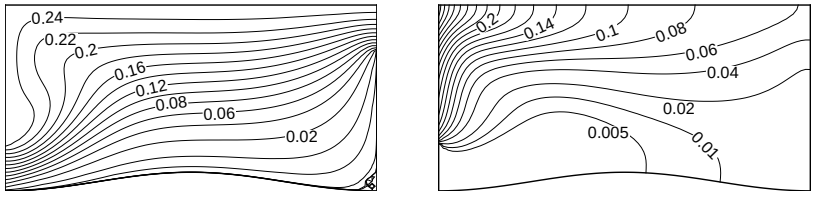

Figure 5.23: Streamline and isotherm contour Re=100 and Ra=100000

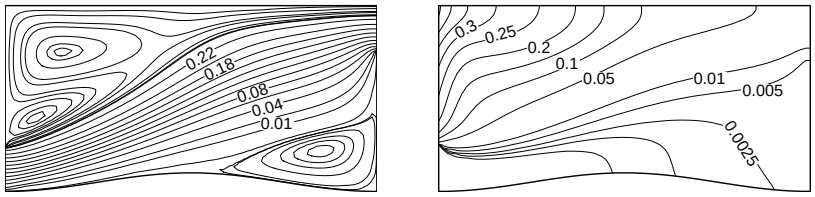

Figure 5.24: Streamline and isotherm contour Re=200 and Ra=100000

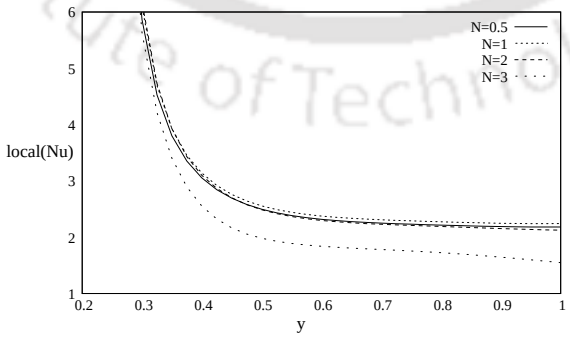

Figure 5.25: local Nusselt number for different value of N for Re=100 and Ra=0

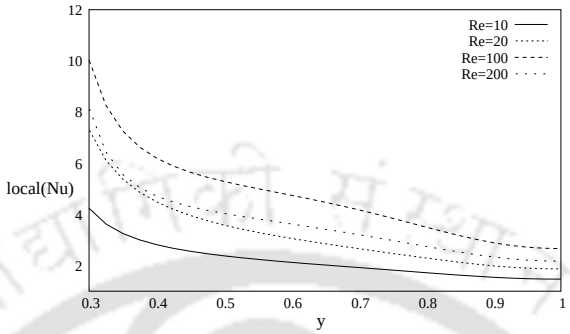

Figure 5.26: local Nusselt number for different value of Re for Ra=100000 and N=1

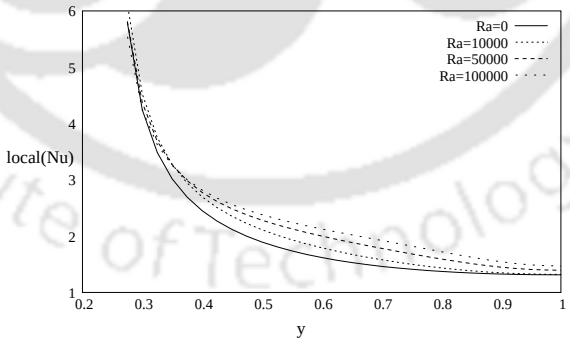

Figure 5.27: local Nusselt number for different value of Ra for $Re = 10$ and N=1

The general trend of the Figs 5.25-5.27 is that the local Nusselt number decreases along the vertical height. Heat transfer near the inlet is maximum whereas it decreases as it moves away from the inlet towards the top of the cavity. Fig 5.25 shows the effect of undulation on heat transfer rate with fixed $Re = 100$ and $Ra = 0$. It shows that when $N = 1$, i.e., when the number of waves is 2 on the bottom wall, the local heat transfer is more compared to that for $N = 0.5$, 2 and 3. When $N = 3$, the local heat transfer rate along the heated wall becomes minimum. Fig 5.26 shows the effects of Re with fixed $Ra = 100000$ and $N = 1$. Local heat transfer increases with the increase of Re from 10 to 100, but when Re increases to 200, the heat transfer rate is less than that for $Re = 100$. Fig 5.27 explains the effect of Ra with fixed $Re = 10$ and $N = 1$. It shows that with the increase of Ra (i.e., the increase in heat flux q at the left wall), the local heat transfer rate increases.

5.5 Conclusions

A mixed convection problem in a vented cavity is numerically studied in this chapter. The cavity is of rectangular shape with the bottom wavy wall. The inlet of this vented cavity is at the bottom of the left wall and it is assumed that there is a constant heat flux at the portion of this wall above the inlet, the outlet is at the top of the opposite vertical wall. The results are discussed when the Prandtl number is 0.71, the Rayleigh number varying from 0 to 100000. The non-dimensional governing equations are solved using the proposed high order compact finite difference scheme. Some important observations of this study are:

(1) Heat transfer rate is high near the lowest point of the heated wall where the inlet meets.

(2) With the increase of Ra, the local heat transfer rate at the heated wall increases.

(3) With the increase of the number of waves at the bottom wall, the heat transfer rate decreases.

6 Magnetohydrodynamic flow in a dilated channel

6.1 Dilated channel problem

Liquid metal flows in rectangular ducts under imposed magnetic fields are important for the metallurgical and materials processing applications, e.g. in electromagnetic flow control, in continuous steel casting and in growth of large silicon crystals. Another area of applications is the liquid metal cooling blankets of breeder type for fusion reactors. The simplest case of a uniform magnetic field parallel to the side wall of the duct has received considerable attention from theoreticians and experimentalists over the past 50 years. The problem is governed by the Reynolds number (Re) and the Hartmann number (Ha), the square of which represents the ratio between the Lorentz and the viscous forces. The velocity field in liquid metal flows under a strong magnetic field tends to vary little along the magnetic field lines so that in many situations such flows are almost two-dimensional. This striking property of this particular kind of MHD flow was first studied in the 1970s [38] and can be observed in many laboratory experiments and industrial applications [8]. The first experimental and theoretical work on MHD channel flow was undertaken by Hartmann and Lazarus [24]. The laminar velocity profile in MHD channel flow is the so-called Hartmann flow (channel flow of an electrically conducting fluid in the presence of a uniform magnetic field). The physical problem of particular interest in this chapter is that of MHD flows confined in a dilated channel and placed in a strong, vertical, steady and uniform magnetic field B_0 in the perpendicular direction. Flow phenomena in such channels resemble with the blood flow through aneurysmal vessels. Many authors [56, 55, 75] have investigated the flow of blood through arteries in the presence of magnetic field under different conditions. In fact, the Lorentz force arising out of the flow across the magnetic lines of force acts on the constituent particles of blood and alters the hemodynamic indicators of blood flow. The potential use of

such MHD principles in prevention and rational therapy of arterial hypertension was explored by Vardanyan [105], who showed that for steady flow of blood in an artery of circular cross-section, a uniform transverse magnetic field alters the flow rate of blood. Recently, Misra et al.[67] investigated the steady MHD flow of a viscous fluid in a slowly varying channel in the presence of a uniform magnetic field. For the endovascular treatment of aneurysms, the experimental studies [44, 46, 45, 100, 98, 99, 102, 104] have indicated the need for a better understanding of the relevant hemodynamic effects. There are numerical studies [9, 16, 17, 21, 30, 47, 76, 39, 40] concerning the hemodynamic effects in aneurysmal vessels. Among these, numerical studies based on finite element methods [9, 17, 21, 47] have been performed on the flow fields in lateral dilated vessel geometries. Although it may be sometimes difficult to relate the assumed geometry and flow conditions to those seen clinically, as such often the simplifications used have helped to provide some understanding of the complexity of underlying physics. In their studies, they have assumed the vessel boundary as rigid and the fluid flow characteristics as Newtonian because the effects of non-Newtonian fluid properties and wall elasticity are not prominent [100, 98, 99].

In the present study, the effects of channel geometry and magnetohydrodynamic forces on the flow field are discussed. The study is restricted to $Re = 1000$ as the transition experiments conducted by Patel and Head [74] showed that the plane Poiseuille flow undergoes transition to turbulence for Re as low as 1000, the Reynolds number being formed using the channel centerline velocity and half the channel width.

In this chapter, the numerical solutions of the flow characteristics in lateral and axisymmetric nonuniform rigid dilated channels are discussed and also the effects of the size of the dilated part on the flow is included.

6.1.1 Geometry of the problem

Dilated channel shows some kind of expansion in the channel. In case of lateral dilated channel, the expansion happens only on one side (the upper wall), while for axisymmetric case, the expansion is on the both sides and symmetric about the centerline i,e the expansions are on both the upper and the lower walls as shown in the Figs 6.1 and 6.2. The walls are considered to be rigid and impermeable. For lateral dilated channel geometry, lower wall is taken as the x-axis and for the other case, centerline is considered as the x-axis. The y-axis is considered to be perpendicular to the x-axis for both the cases. The dilation is assumed to be symmetric about the y-axis as well.

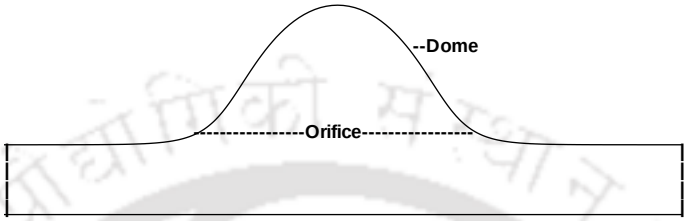

Figure 6.1: Lateral dilated channel

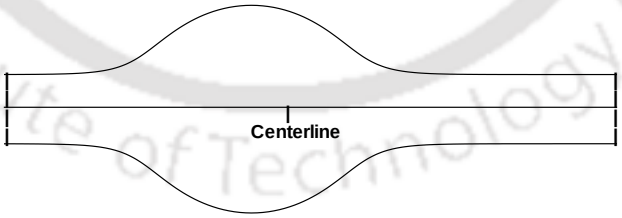

Figure 6.2: Axisymmetric dilated channel

6.1.2 Governing equations for dilated channel problem:

The fluid considered here is electrically conducting in the presence of a constant magnetic field applied in the perpendicular direction of the channel. The flow through the channel is assumed to be two-dimensional, incompressible, viscous, laminar and Newtonian. The assumptions imposed on the flow model are as follows:

(a) The effects of induced magnetic and electric fields due to the flow of electrically conducting fluid are negligible.

(b) No external electric field is present in the dilated channel.

The equations that govern the flow in a dilated channel in presence of a magnetic field can be introduced as:

$$\frac{\partial u}{\partial x}+\frac{\partial v}{\partial y}=0, \tag{6.1}$$

$$\rho\left(\frac{\partial u}{\partial t}+u\frac{\partial u}{\partial x}+v\frac{\partial u}{\partial y}\right)=-\frac{\partial p}{\partial x}+\mu\left(\frac{\partial^2 u}{\partial x^2}+\frac{\partial^2 u}{\partial y^2}\right)-\sigma B^2 u, \tag{6.2}$$

and

$$\rho\left(\frac{\partial v}{\partial t}+u\frac{\partial v}{\partial x}+v\frac{\partial v}{\partial y}\right)=-\frac{\partial p}{\partial y}+\mu\left(\frac{\partial^2 v}{\partial x^2}+\frac{\partial^2 v}{\partial y^2}\right), \tag{6.3}$$

where u and v are the velocities along the x and y- directions respectively, t is time, ρ is the density of the fluid, σ is the conductivity of the fluid, p is the pressure, μ is the coefficient of the viscosity, B is the strength of the magnetic field applied on the perpendicular direction of the dilated channel.

In non-dimensional form, these equations can be written as

$$\frac{\partial U}{\partial X}+\frac{\partial V}{\partial Y}=0, \tag{6.4}$$

$$\frac{\partial U}{\partial \tau}+u\frac{\partial U}{\partial X}+V\frac{\partial U}{\partial Y}=-\frac{\partial P}{\partial X}+\frac{1}{Re}\left(\frac{\partial^2 U}{\partial X^2}+\frac{\partial^2 U}{\partial Y^2}\right)-\frac{Ha^2}{Re}U, \tag{6.5}$$

$$\frac{\partial V}{\partial \tau}+U\frac{\partial V}{\partial X}+V\frac{\partial V}{\partial Y}=-\frac{\partial P}{\partial Y}+\frac{1}{Re}\left(\frac{\partial^2 V}{\partial X^2}+\frac{\partial^2 V}{\partial Y^2}\right). \tag{6.6}$$

For non-dimensionalization, we consider $X=\frac{x}{L}$, $Y=\frac{y}{L}$, $U=\frac{u}{U_0}$, $V=\frac{v}{U_0}$, $\tau=\frac{tU_0}{L}$, $P=\frac{p}{\rho U_0^2}$, $Re=\frac{U_0 L}{\nu}$ is the Reynolds number, where L is the unperturbed channel width, U_0 is the average velocity of the flow at the entrance and ν is the kinematic viscosity, $Ha(=BL\sqrt{(\sigma/\rho\nu)})$ is the Hartmann number.

If we introduce stream-function (ψ) and vorticity (ζ) as:

$$U = \frac{\partial \psi}{\partial Y}, V = -\frac{\partial \psi}{\partial Y} \tag{6.7}$$

and

$$\zeta = \frac{\partial V}{\partial X} - \frac{\partial U}{\partial Y}, \tag{6.8}$$

the above equations can be written as

$$-\frac{\partial^2 \psi}{\partial X^2} - \frac{\partial^2 \psi}{\partial Y^2} = \zeta, \tag{6.9}$$

$$Re\frac{\partial \zeta}{\partial \tau} - \frac{\partial^2 \zeta}{\partial X^2} - \frac{\partial^2 \zeta}{\partial Y^2} + URe\frac{\partial \zeta}{\partial X} + VRe\frac{\partial \zeta}{\partial Y} = Ha^2\frac{\partial U}{\partial Y}. \tag{6.10}$$

In the absence of any magnetic field, the governing Navier-Stokes equations in terms of streamfunction and vorticity become

$$-\frac{\partial^2 \psi}{\partial X^2} - \frac{\partial^2 \psi}{\partial Y^2} = \zeta, \tag{6.11}$$

$$Re\frac{\partial \zeta}{\partial \tau} - \frac{\partial^2 \zeta}{\partial X^2} - \frac{\partial^2 \zeta}{\partial Y^2} + URe\frac{\partial \zeta}{\partial X} + VRe\frac{\partial \zeta}{\partial Y} = 0. \tag{6.12}$$

6.1.3 Boundary conditions

No-slip boundary condition is applied at the upper and lower boundaries whereas Hartmann velocity profile is specified to set the inflow boundary condition. Since the physical condition at infinite distance has to be imposed at a finite downstream location, the outflow condition for the downstream boundary is considered as fully developed flow condition.

The imposed inlet boundary condition is as follows.

For lateral dilated channel:

$$\begin{aligned} V &= 0, \\ U &= 6Y(1-Y) \text{ for } Ha = 0, \qquad (6.13) \\ U &= \frac{3}{4}\left(\frac{\cosh\left(\frac{Ha}{2}\right) - \cosh\left(Ha\left(Y-\frac{1}{2}\right)\right)}{\sinh^2\left(\frac{Ha}{4}\right)}\right) \text{ for } Ha \neq 0, \qquad (6.14) \end{aligned}$$

and for axisymmetric dilated channel:

$$\begin{aligned} V &= 0, \\ U &= 1.5(1-Y^2) \text{ for } Ha = 0, \qquad (6.15) \\ U &= \frac{3}{4}\left(\frac{\cosh\left(\frac{Ha}{2}\right) - \cosh\left(\frac{Ha}{2}Y\right)}{\sinh^2\left(\frac{Ha}{4}\right)}\right) \text{ for } Ha \neq 0. \qquad (6.16) \end{aligned}$$

Initially, the whole system was at rest and at the inlet a velocity profile as discussed above is imposed. This is considered as initial condition.

6.2 Numerical methods for solving the governing equations

The transformation, used to map the nonuniform dilated channel (in the physical domain) to a rectangular channel (in computational domain), is

$$X = \xi + \frac{D_1 \sinh(D_2\pi\xi)}{\cosh(D_2\pi\xi) + \cos(D_2\pi\eta)}, \qquad (6.17)$$

$$Y = \eta + \frac{D_1 \sin(D_2\pi\eta)}{\cosh(D_2\pi\xi) + \cos(D_2\pi\eta)}, \qquad (6.18)$$

where X-Y is the physical plane and ξ-η is the computational plane. The constants D_1 and D_2 ($1 \leq D_1 \leq 3, \quad 0.1 \leq D_2 \leq 1$) are used to control the size of the dilated part of the channel.

Using this transformation, the governing equations with time derivative term (6.10) for this problem, which is of the type

$$l\frac{\partial\phi}{\partial t} + a\frac{\partial^2\phi}{\partial x^2} + g\frac{\partial^2\phi}{\partial x\partial y} + b\frac{\partial^2\phi}{\partial y^2} + c\frac{\partial\phi}{\partial x} + d\frac{\partial\phi}{\partial y} + r\phi = \chi + l_1\frac{\partial\epsilon_1}{\partial x} + l_2\frac{\partial\epsilon_1}{\partial y} + l_3\frac{\partial\epsilon_2}{\partial x} + l_4\frac{\partial\epsilon_2}{\partial y}, \qquad (6.19)$$

may be written as:

$$l\frac{\partial\hat{\phi}}{\partial t} + a_1\frac{\partial^2\hat{\phi}}{\partial\xi^2} + b_1\frac{\partial^2\hat{\phi}}{\partial\eta^2} + g_1\frac{\partial^2\hat{\phi}}{\partial\xi\partial\eta} + c_1\frac{\partial\hat{\phi}}{\partial\xi} + d_1\frac{\partial\hat{\phi}}{\partial\eta} + r_1\hat{\phi} = f_1, \qquad (6.20)$$

where the coefficients are obtained using the relations available in (2.3) in Chapter 2.

After discretization, using the same procedure discussed in Chapter 2 for time dependent case, the equation can be written in algebraic form, as:

$$\begin{aligned} \sum_{s_1=-1}^{1}\sum_{s_2=-1}^{1} w_{i+s_1,j+s_2}\phi^{(n+1)}_{i+s_1,j+s_2} &= \sum_{s_1=-1}^{1}\sum_{s_2=-1}^{1} w'_{i+s_1,j+s_2}\phi^{(n)}_{i+s_1,j+s_2} \\ &+ \Delta t\left(\mu F^{(n+1)}_{i,j} + (1-\mu)F^{(n)}_{i,j}\right). \qquad (6.21) \end{aligned}$$

For equation (6.10), $\phi = \zeta$, $l = Re$, $a = -1$, $b = -1$, $c = URe$, $d = VRe$, $g = 0$, $r = 0$, $\chi = 0$, $l_1 = 0$, $l_2 = Ha^2$, $l_3 = 0$, $l_4 = 0$ and $\epsilon_1 = U$.

Equation (6.9) is of the type

$$a\frac{\partial^2\phi}{\partial x^2} + g\frac{\partial^2\phi}{\partial x\partial y} + b\frac{\partial^2\phi}{\partial y^2} + c\frac{\partial\phi}{\partial x} + d\frac{\partial\phi}{\partial y} + r\phi = \chi + l_1\frac{\partial\epsilon_1}{\partial x} + l_2\frac{\partial\epsilon_1}{\partial y} + l_3\frac{\partial\epsilon_2}{\partial x} + l_4\frac{\partial\epsilon_2}{\partial y}, \quad (6.22)$$

which, after taking the transformation, becomes

$$a_1\frac{\partial^2\hat{\phi}}{\partial\xi^2} + b_1\frac{\partial^2\hat{\phi}}{\partial\eta^2} + g_1\frac{\partial^2\hat{\phi}}{\partial\xi\partial\eta} + c_1\frac{\partial\hat{\phi}}{\partial\xi} + d_1\frac{\partial\hat{\phi}}{\partial\eta} + r_1\hat{\phi} = f_1, \quad (6.23)$$

where the coefficients are obtained using the relations available in (2.3) in Chapter 2.

After discretization, using the same procedure discussed in Chapter 2 for time independent case, the equation can be written in algebraic form, discussed in Chapter 2, as:

$$\sum_{s_1=-1}^{1}\sum_{s_2=-1}^{1} w_{i+s_1,j+s_2}\phi_{i+s_1,j+s_2} = F_{i,j}. \quad (6.24)$$

For equation (3.9), $\phi = \psi$, $a = -1$, $b = -1$, $c = 0$, $d = 0$, $g = 0$, $r = 0$, $\chi = \zeta$, $l_1 = 0$, $l_2 = 0$, $l_3 = 0$, $l_4 = 0$.

Biconjugate-Gradient stabilized methods without preconditioning are applied for solving the system of equations in all the cases whenever it appears during the process of solving the equations after discretizations.

6.2.1 Grid independency

Generally, any desired accuracy in a solution is obtained by reducing the grid size in the computation. Reduction of grid size implies an increase in number of grid points which in turn affects the computational cost. To overcome this situation, we need a standard grid size so that further reduction in grid size does not influence results of the problem.

Here, the computational cost of the results using $(h, k) = (\frac{1}{80}, \frac{1}{50})$ i.e., grid size 81×5001, is very much compared to $(h, k) = (\frac{1}{40}, \frac{1}{25})$ where grid size is 41×2501. Since the results obtained from these two types of grid sizes differ slightly, the grid size 41×2501 is considered to be the reasonable grid size for the grid-independent solutions of the problem and is used for the required results for discussion.

6.2.2 Results and Discussions

In order to discuss the results of the problem, the governing equations are solved through the proposed HOC scheme for the parameters Reynolds number ranging from 100 to

Table 6.1: Values of ψ_{max} and the position of primary vortex for different grid sizes in dilated channel problem

(h, k)	Re	Ha	ψ_{max}	center of the primary vortex (x, y)
$\left(\frac{1}{40}, \frac{1}{25}\right)$	100	1	7.19331	(0.645887, 2.03994)
		2	2.67059	(-0.266104, 2.16078)
		3	1.827575	(-1.46201, 2.19796)
$\left(\frac{1}{80}, \frac{1}{50}\right)$	100	1	7.1935	(0.582729, 2.04857)
		2	2.67053	(-0.266104, 2.16078)
		3	1.82751	(-1.44881, 2.16228)

1000 and Hartmann number from 1 to 15. Discussions are made with the help of graphs.

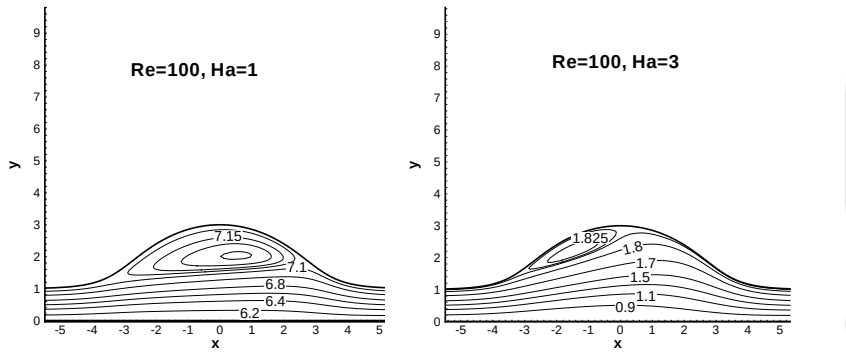

Figure 6.3: Streamline contour with Re=100 for Ha=1 and Ha=3

Fig 6.3 and Fig 6.4 show that with the increase in Hartmann number (magnetic strength), the vortex formed in the dome gradually becomes weaker and pushed by the main flow towards the upper side in the dome and ultimately it disappears. This is because initially the velocity of the fluid was higher and when the fluid crosses the dome, some fluid moves backward and a vortex is formed. But with the increase of Hartmann number, the velocity decreases and the amount of fluid which moves backward is less and hence the vortex moves to the left side of the dilated part. Due to further increase in Ha, there is no backward flow in the dilated part and no vortex is formed. The fluid

moves in the forward direction only.

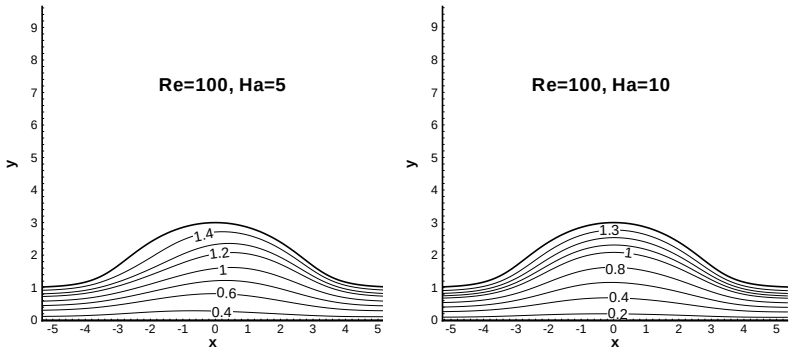

Figure 6.4: Streamline contour with Re=100 for Ha=5 and Ha=10

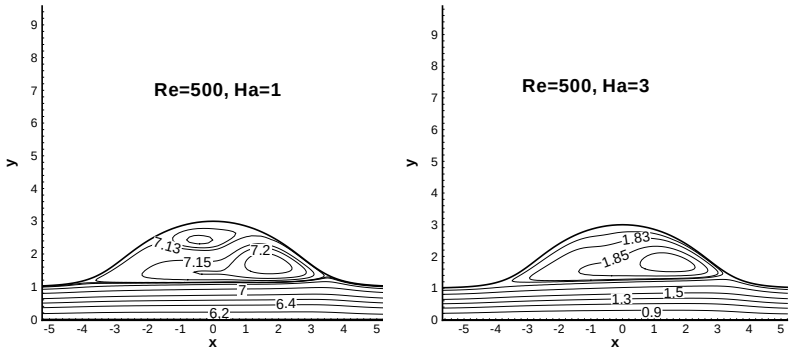

Figure 6.5: Streamline contour with Re=500 for Ha=1 and Ha=3

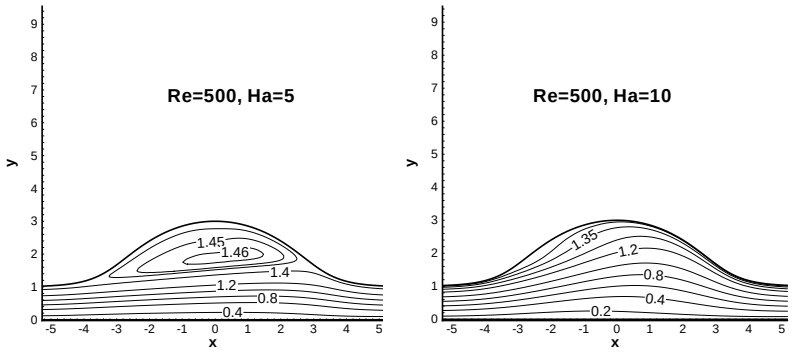

Figure 6.6: Streamline contour with Re=500 for Ha=5 and Ha=10

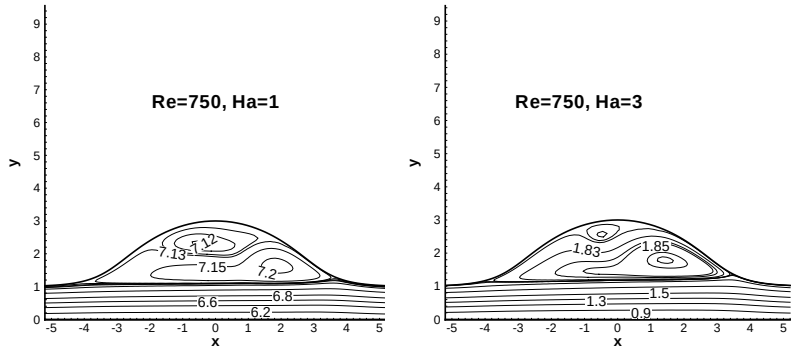

Figure 6.7: Streamline contour with Re=750 for Ha=1 and Ha=3

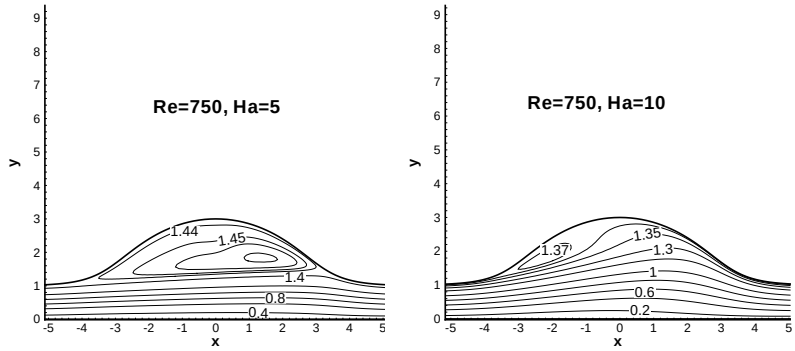

Figure 6.8: Streamline contour with Re=750 for Ha=5 and Ha=10

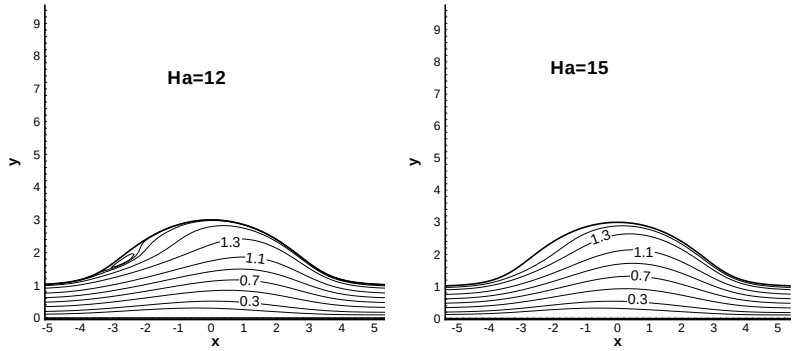

Figure 6.9: Streamline contour with Re=750 for Ha=12 and Ha=15

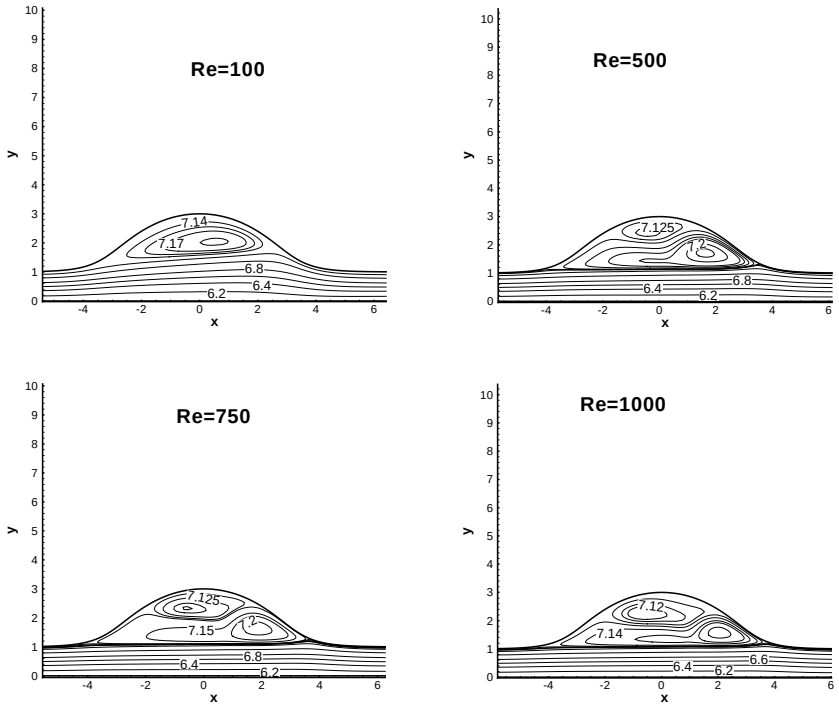

Figure 6.10: Streamline contour with Ha=1 for different Re

Fig 6.5 and Fig 6.6 show the streamline contours for $Re = 500$ and $Ha = 1, 3, 5$ and 10. With the increase of Reynolds number, the velocity increases and two vortices appear in the dilated part and with the increase of Hartmann number, the velocity decreases. When $Ha = 1$, there are two vortices, one at the right side of the dilated part and other one is a secondary vortex at the top portion of the dilated part. When Hartmann number increases to $Ha = 3$, there is only one vortex at the right side of the dilated part. When $Ha = 5$, the vortex moves slightly upward and when $Ha = 10$, vortex disappears. Fig 6.7, Fig 6.8 and Fig 6.9 show the streamline contours of the fluid where the Reynolds number is taken as $Re = 750$ and Hartmann number as $Ha = 1, 3, 5, 10, 12$ and 15. When $Ha = 1$, there are two vortices in the dilated part and the size of the secondary vortex at the top portion becomes larger than that in the case when $Re = 500$ and $Ha = 1$. When $Ha = 3$, there are two vortices when the size of the secondary vortex becomes smaller. When $Ha = 5$, there is only one vortex, which occupies the whole dilated part and this vortex moves to the back side of the dilated part when Hartmann number is $Ha = 10$. With the increase of the Hartmann number to $Ha = 15$, this vortex disappears and there is no back flow in the dilated channel.

With the increase of Hartmann number, the Lorentz force increases, which enhances

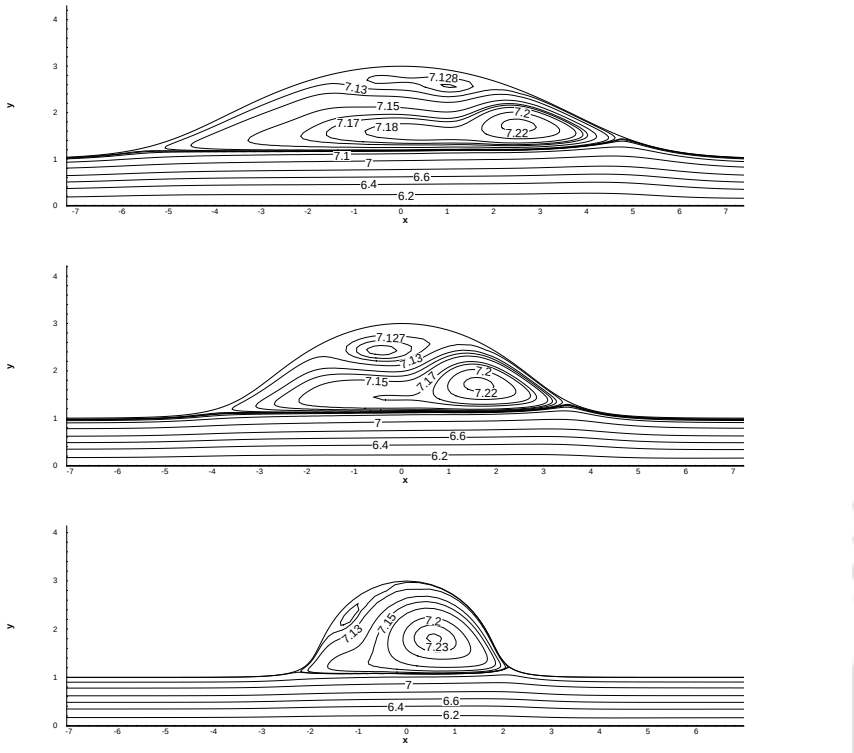

Figure 6.11: Streamline contour with Re=500 and Ha=1 for different length of orifice

the retardation of the flow. From the Figs 6.5-6.8, it can be seen that with the increase of the Hartmann number, the number of the vortices decreases and they slowly disappear since the velocity of the flow gradually reduces.

Fig 6.10 shows the effects of Reynolds number for $Ha = 1$. With the increase of Reynolds number, the velocity of the fluid generally increases. For $Re = 100$, flow separation takes place in the dilated part and one vortex is formed spanning almost the whole of the dilated part. For $Re = 500$, there is another secondary vortex in the dilated channel. When Re increases to 750 and 1000, the secondary vortices become larger and the circulations become stronger as the velocity increases with the increase of Reynolds number.

Figs 6.11 and 6.12 show the effects of the size of dilation in the flow. It has been compared for the Reynolds number, $Re = 500$ and $Ha = 1$ with different sizes of dilation. Here, the height of the dilated part is kept fixed whereas the length of the orifice varies. From the figures, it can be concluded that with the increase of orifice length, the flux in the dilated part increases, as a result the secondary and tertiary flow separations take place inside and near the dome.

We have studied the flow patterns for different Ha in the full axisymmetric dilated

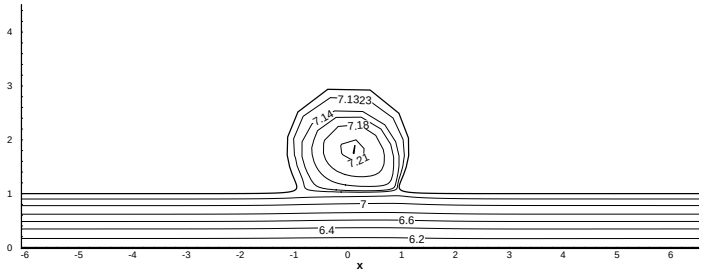

Figure 6.12: Streamline contour with Re=500 and Ha=1

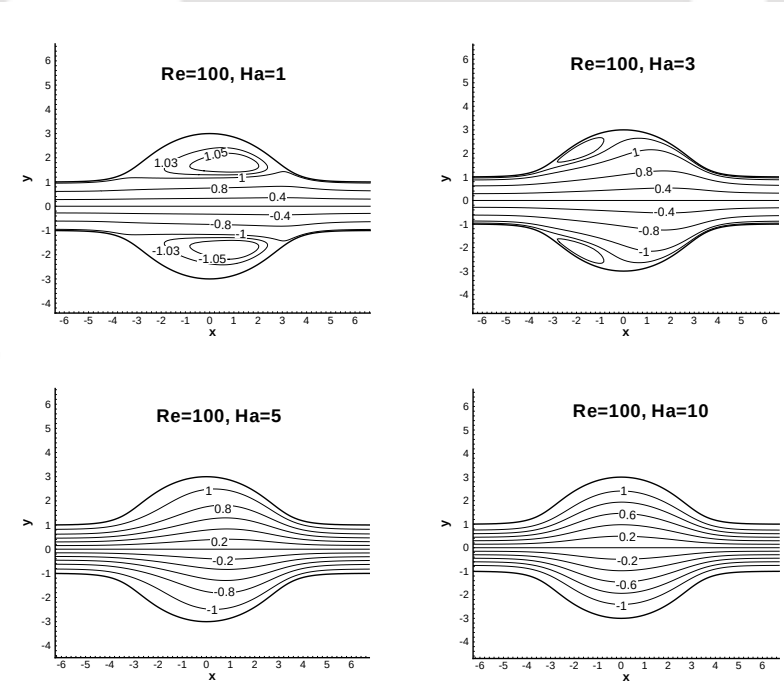

Figure 6.13: Streamline contour with Re=100

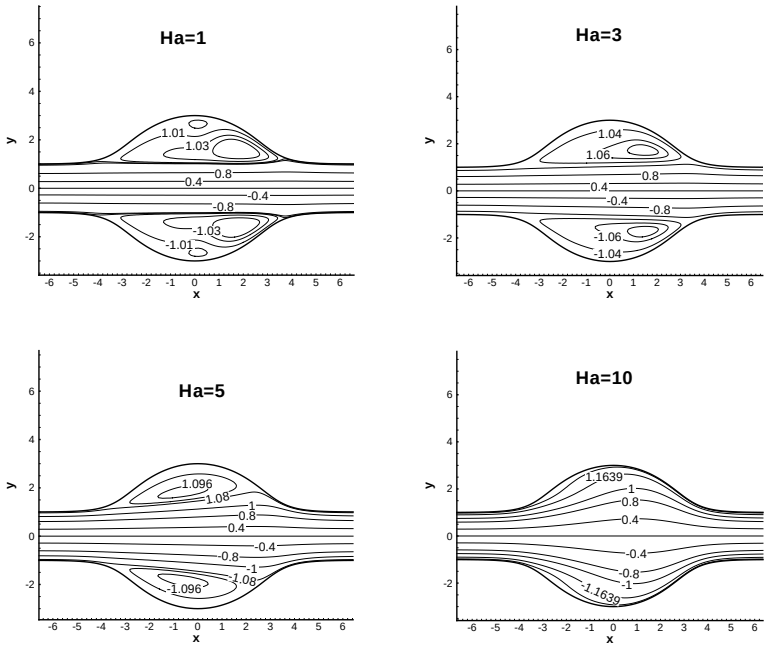

Figure 6.14: Streamline contour with Re=500

channel. In Figs 6.13 and 6.14, the streamline contours are presented for $Re = 100$ and $Re = 500$, respectively, for different Hartmann number $Ha = 1, 3, 5$ and 10. When $Re = 100$ and $Ha = 1$, there are two vortices in the dilated part of the channel, one at the upper dilated portion of the channel, which covers almost all dilated part of the channel and the other one at the lower portion of the channel, which covers the lower dilated part of the channel. The vortices disappear for $Ha \geq 5$. With the increase of Re to 500, the number of vortices increases in both sides of the dilated channel. With the increase of Hartmann number, the number of vortices reduces and for $Ha \geq 10$, vortices disappear. It is observed that the curves of constant stream function values and the size of the recirculation zones are symmetrical with respect to the centerline. With the increase of Re, the fluid velocity increases and the vortices appear. With the increase of Hartmann number Ha, the fluid velocity decreases and the vortices diminish. With the increase of the length of the dilated part, the velocity of the flow increases and the number of vortices also increases.

Fig 6.15 shows the streamline contours for $Re = 500$, $Ha = 1, 3, 5$ and 10. Here, the length of the dilated part is less than that of Fig 6.14, the flow separation takes place even after $Ha = 10$ unlike the case shown in Fig 6.14. When the orifice length is short, the flow inside the dilated part becomes stronger and more number of vortices

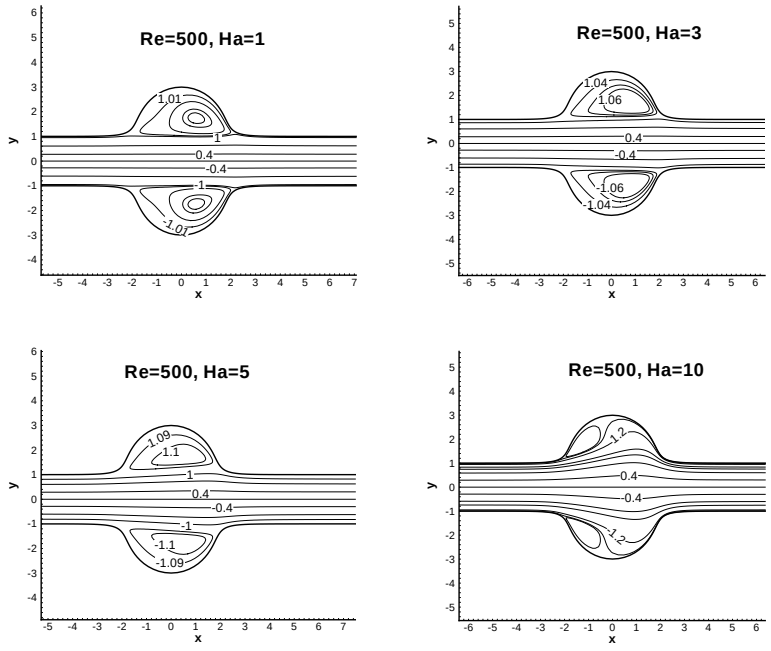

Figure 6.15: Streamline contour with Re=500 (with different orifice length from Fig (6.14))

are formed.

6.3 Conclusions

In this chapter, a magnetohydrodynamic flow in a dilated channel is considered. Lateral and axisymmetric dilation ases are studied and streamline contours are discussed. The proposed fourth order accurate HOC finite difference scheme is used to solve the problem. Some important observations of this study are listed as:
(1) With the increase of Reynolds number, the number of vortices increases in the dilated part of the channel.
(2) With the increase of Hartmann number, the number of vortices decreases and flow becomes simpler.
(3) As the length of the dilated part becomes larger, flux increases and flow becomes more complicated.

भारतीय प्रौद्योगिकी संस्थान गुवाहाटी
Indian Institute of Technology Guwahati

7

Conclusions and Future work

In this thesis, an improved version of of the existing higher order compact (HOC) scheme is proposed to make it more robust and more general in nature from the application point of view. There was difficulty in dealing with the governing equations that contained mixed derivative and source terms involving derivatives in the governing equations in the existing HOC schemes. In the proposed version, this complication is resolved so as to solve more general problems with complex geometries. The higher order compact (HOC) finite difference scheme is modified for a convection-diffusion-reaction equation with non-homogeneous source function containing derivative terms, which is applicable on nonorthogonal curvilinear grid. The scheme is applied for various types of problems such as lid driven cavity problem, natural convection problem, mixed convection problem, vented cavity problem for non uniform grid in order to demonstrate the strength of the proposed scheme. In some problems, magnetic field is also considered to study the effect of magnetic field.

In Chapter 2, both time independent and time dependent forms of the HOC finite difference schemes are discussed. Results obtained by using this modified scheme are compared with the analytical solutions of the two problems and appreciable agreements are observed. Lid driven problem in a square cavity with bottom wavy wall and also in a vase-shaped cavity are solved by using the proposed scheme.

In Chapter 3, the natural convection in two-dimensional wavy enclosure in presence of magnetic field has been studied numerically. The left and right walls of the enclosure are wavy whereas the top and bottom walls are straight. The bottom wall is heated either uniformly or non-uniformly ($T(x) = \sin(\pi x)$). In this study, Rayleigh number is varies from 1000 to 100000, Hartmann number from 1 to 10. Two Prandtl numbers are considered as 0.71 and 7. The number of undulation is kept fixed at $M = 2$. High order compact finite difference scheme proposed in Chapter 2 is used to solve the non-

dimensional governing equations. The important results obtained are as follows:
(1) When the Rayleigh number is higher ($> 10^3$), the local Nusselt number at the bottom wall shows an oscillatory behaviour due to the presence of multiple vortices in the cavity. However, the local Nusselt number attains its maximum value at the corner points of the bottom wall and the minimum one at the center.
(2) For nonuniform heating of the bottom wall, the heat transfer rate is 0 at the corners of this wall. A sinusoidal type of local heat transfer rate is observed showing minimum at the corner points as well as at the center of the bottom wall.
(3) Local heat transfer rate at the center of the bottom wall is higher in the case of nonuniform heating in comparison to that of uniform heating.
(4) When Ra is 1000, there is no difference in the local heat transfer rate at the bottom wall for the Prandlt number 0.71 and 7, but as Ra increases to 100000, a noticeable difference in local Nusselt number at the bottom wall for these two Prandlt numbers is observed.
(5) With the increase in Hartmann number, the velocity as well as the heat transfer rate decreases.

In Chapter 4, a mixed convection problem in a trapezoidal cavity is considered. The bottom wall is heated uniformly, while the inclined side walls are cold and the moving top wall is adiabatic. The modified fourth order accurate HOC finite difference scheme is used to solve the problem. The Grashof number Gr varies from 1000 to 100000, Prandtl numbers are considered as 0.71 and 7. Some significant observations of this study are listed as:
(1) Local heat transfer rate at the edges of the heated wall is high and a parabolic type profile is observed for the Nusselt number along the bottom wall.
(2) With the increase of Gr, the heat transfer rate increases.
(3) With the increase of the height of the trapezoidal cavity from 1 to 3, enhancement in the local heat transfer rate is observed.
(4) The heat transfer rate along the bottom wall shows a unimodal trend up to a certain value of the width of the bottom wall. With further increase in the width, the unimodal trend becomes bimodal.

A mixed convection problem in a vented cavity is numerically studied in Chapter 5. The cavity is of rectangular shape with the bottom wavy wall. The inlet of this vented cavity is at the bottom of the left wall and it is assumed that there is a constant heat flux at the rest of this wall and the outlet is at the top of the opposite vertical wall. The results are discussed when the Prandtl number is 0.71, the Rayleigh number varying from 0 to 100000. The non dimensional governing equations are solved using

the proposed high order compact finite difference scheme. Some important observations of this study are:
(1) Heat transfer rate is high near the top of the inlet.
(2) With the increase in Ra, the local heat transfer rate at the heated wall increases.
(3) With the increases in the number of waves at the bottom wall, the heat transfer rate decreases.

Chapter 6 deals with the magnetohydrodynamic flow in a dilated channel. Both lateral and axisymmetric dilation cases are studied and streamlines contours are examined. The proposed fourth order accurate HOC finite difference scheme is used to solve the problem numerically. Some important observations of this study are:
(1) With the increase of the Reynolds number, the number of vortices increases in the dilated part of the channel.
(2) With the increase of the Hartmann number, the number of vortices decreases and flow becomes simpler.
(3) As the length of the dilated part becomes larger, flux increases and flow becomes more complicated.

From all the studies, it can be concluded that the proposed scheme is a powerful and robust HOC finite difference scheme. It can efficiently handle the hydrodynamic flows, magnetohydrodynamic flows and heat transfer problems in complex geometries accurately, with ease.

7.1 Future scopes:

Some ideas related to this work for further research are mentioned in this section.
1. In this thesis, the enclosure consists of inlet and outlet, either a constant velocity profile or parabolic velocity profiles are prescribed at the inlet. Study of these types of problems with pulsatile flows at the inlet will be interesting.
2. Two dimensional problems are solved throughout the thesis. The scheme can be extended to be used to solve three dimensional channel or tube problems.
3. Study of non-Newtonian fluid through stenosed tube with elastic wall would be an important work.

Bibliography

[1] L. Adjlout, O. Imine, A. Azzi, and M. Belkadi, *Laminar natural convection in an inclined cavity with a wavy wall*, International Journal of Heat and Mass Transfer, 45 (2002), pp. 2141–2152.

[2] S. Alchaar, P. Vasseur, and E. Bilgen, *Natural convection heat transfer in a rectangular enclosure with a transverse magnetic field*, Journal of Heat Transfer, 117 (1995), pp. 668–673.

[3] V. S. Arpaci and P. S. Larsen, *Convection Heat Transfer*, Prentice Hall, 1984.

[4] H. Asan and L. Namli, *Laminar natural convection in a pitched roof of triangular cross-section: summer day boundary conditions*, Energy and Buildings, 33 (2000), pp. 69–73.

[5] T. Basak, S. Roy, S. K. Babu, and I. Pop, *Finite element simulations of natural convection flow in an isosceles triangular enclosure filled with a porous medium: Effects of various thermal boundary conditions*, International Journal of Heat and Mass Transfer, 51 (2008), pp. 2733–2741.

[6] T. Basak, S. Roy, and A. Balakrishnan, *Effects of thermal boundary conditions on natural convection flows within a square cavity*, International Journal of Heat and Mass Transfer, 49 (2006), pp. 4525–4535.

[7] T. Basak, S. Roy, A. Singh, and I. Pop, *Finite element simulation of natural convection flow in a trapezoidal enclosure filled with porous medium due to uniform and non-uniform heating*, International Journal of Heat and Mass Transfer, 52 (2009), pp. 70–78.

[8] L. Bhler, *Instabilities in quasi-two-dimensional magnetohydrodynamic flows*, Journal of Fluid Mechanics, 326 (1996), pp. 125–150.

[9] A. C. Burleson, C. M. Strother, and V. T. Turitto, *Computer modeling of intracranial saccular and lateral aneurysms for the study of their hemodynamics*, Neurosurgery, 37 (1995), pp. 774–784.

[10] G. Carey and W. Spotz, *Higher-order compact mixed methods*, Communications in Numerical Methods in Engineering, 13 (1997), pp. 553–564.

[11] C. Cha and Y. Jaluria, *Recirculating mixed convection flow for energy extraction*, International Journal of Heat and Mass Transfer, 27 (1984), pp. 1801–1812.

[12] A. J. Chamkha, S. H. Hussain, and Q. R. Abd-Amer, *Mixed convection heat transfer of air inside a square vented cavity with a heated horizontal square cylinder*, Numerical Heat Transfer, Part A: Applications, 59 (2011), pp. 58–79.

[13] C. Choi and A. Ortega, *Mixed convection in an inclined channel with a discrete heat source*, in Thermal Phenomena in Electronic Systems, 1992. I-THERM III, InterSociety Conference on, IEEE, 1992, pp. 40–48.

[14] P. K. Das and S. Mahmud, *Numerical investigation of natural convection inside a wavy enclosure*, International Journal of Thermal Sciences, 42 (2003), pp. 397–406.

[15] S. Dennis and J. Hudson, *Compact h 4 finite-difference approximations to operators of navier-stokes type*, Journal of Computational Physics, 85 (1989), pp. 390–416.

[16] J. A. Ekaterinaris, C. V. Ioannou, and A. N. Katsamouris, *Flow dynamics in expansions characterizing abdominal aorta aneurysms*, Annals of Vascular Surgery, 20 (2006), pp. 351–359.

[17] E. A. Finol and C. H. Amon, *Flow-induced wall shear stress in abdominal aortic aneurysms: Part i-steady flow hemodynamics*, Computer Methods in Biomechanics & Biomedical Engineering, 5 (2002), pp. 309–318.

[18] J. Garandet, T. Alboussiere, and R. Moreau, *Buoyancy driven convection in a rectangular enclosure with a transverse magnetic field*, International Journal of Heat and Mass Transfer, 35 (1992), pp. 741–748.

[19] E. Gartland, Jr, *Discrete weighted mean approximation of a model convection-diffusion equation*, SIAM Journal on Scientific and Statistical Computing, 3 (1982), pp. 460–472.

[20] C. Gau, Y. Jeng, and C. Liu, *An experimental study on mixed convection in a horizontal rectangular channel heated from a side*, Journal of Heat Transfer, 122 (2000), pp. 701–707.

[21] C. F. Gonzalez, Y. I. Cho, H. V. Ortega, and J. Moret, *Intracranial aneurysms: flow analysis of their origin and progression.*, American Journal of Neuroradiology, 13 (1992), pp. 181–188.

[22] G. Guo and M. A. Sharif, *Mixed convection in rectangular cavities at various aspect ratios with moving isothermal sidewalls and constant flux heat source on the bottom wall*, International Journal of Thermal Sciences, 43 (2004), pp. 465–475.

[23] M. M. Gupta, R. P. Manohar, and J. W. Stephenson, *A single cell high order scheme for the convection-diffusion equation with variable coefficients*, International Journal for Numerical Methods in Fluids, 4 (1984), pp. 641–651.

[24] J. Hartmann and F. Lazarus, *Hg-dynamics II: Experimental Investigations on the Flow of Mercury in a Homogeneous Magnetic Field*, Levin & Munksgaard, 1937.

[25] G. Holtzman, R. Hill, and K. Ball, *Laminar natural convection in isosceles triangular enclosures heated from below and symmetrically cooled from above*, Journal of Heat Transfer, 122 (2000), pp. 485–491.

[26] T. Hsu, *Mixed convection in a rectangular enclosure with discrete heat sources*, Numerical Heat Transfer: Part A: Applications, 38 (2000), pp. 627–652.

[27] T.-H. Hsu, P.-T. Hsu, and S.-P. How, *Mixed convection in a partially divided rectangular enclosure*, Numerical Heat Transfer, Part A Applications, 31 (1997), pp. 655–683.

[28] F. Ideriah, *Prediction of turbulent cavity flow driven by buoyancy and shear*, Journal of Mechanical Engineering Science, 22 (1980), pp. 287–295.

[29] J. Imberger and P. Hamblin, *Dynamics of lakes, reservoirs, and cooling ponds*, Annual Review of Fluid Mechanics, 14 (1982), pp. 153–187.

[30] T. Ishikawa, S. Oshima, and R. Yamane, *Vortex enhancement in blood flow through stenosed and locally expanded tubes*, Fluid Dynamics Research, 26 (2000), pp. 35–52.

[31] R. Iwatsu and J. M. Hyun, *Three-dimensional driven-cavity flows with a vertical temperature gradient*, International Journal of Heat and Mass Transfer, 38 (1995), pp. 3319–3328.

[32] R. Iwatsu, J. M. Hyun, and K. Kuwahara, *Mixed convection in a driven cavity with a stable vertical temperature gradient*, International Journal of Heat and Mass Transfer, 36 (1993), pp. 1601–1608.

[33] Y. Jaluria and C. Cha, *Heat rejection to the surface layer of a solar pond*, Journal of Heat Transfer, 107 (1985), pp. 99–106.

[34] D. D. Joye, *Comparison of correlations and experiment in opposing flow, mixed convection heat transfer in a vertical tube with grashof number variation*, International Journal of Heat and Mass Transfer, 39 (1996), pp. 1033–1038.

[35] S. Kakarantzas, I. Sarris, A. Grecos, and N. Vlachos, *Magnetohydrodynamic natural convection in a vertical cylindrical cavity with sinusoidal upper wall temperature*, International Journal of Heat and Mass Transfer, 52 (2009), pp. 250–259.

[36] J. C. Kalita, D. Dalal, and A. K. Dass, *A class of higher order compact schemes for the unsteady two-dimensional convection–diffusion equation with variable convection coefficients*, International Journal for Numerical Methods in Fluids, 38 (2002), pp. 1111–1131.

[37] K. M. Khanafer and A. J. Chamkha, *Mixed convection flow in a lid-driven enclosure filled with a fluid-saturated porous medium*, International Journal of Heat and Mass Transfer, 42 (1999), pp. 2465–2481.

[38] Y. B. Kolesnikov and A. Tsinober, *Experimental investigation of two-dimensional turbulence behind a grid*, Fluid Dynamics, 9 (1974), pp. 621–624.

[39] B. R. Kumar and K. Naidu, *Finite element analysis of nonlinear pulsatile suspension flow dynamics in blood vessels with aneurysm*, Computers in Biology and Medicine, 25 (1995), pp. 1–20.

[40] ——, *Hemodynamics in aneurysm*, Computers and Biomedical Research, 29 (1996), pp. 119–139.

[41] R. Kumar and T.-D. Yuan, *Recirculating mixed convection flows in rectangular cavities*, Journal of Thermophysics and Heat Transfer, 3 (1989), pp. 321–329.

[42] P. Lax and B. Wendroff, *Systems of conservation laws*, Communications on Pure and Applied Mathematics, 13 (1960), pp. 217–237.

[43] S. K. Lele, *Compact finite difference schemes with spectral-like resolution*, Journal of Computational Physics, 103 (1992), pp. 16–42.

[44] Z. Li and C. Kleinstreuer, *Blood flow and structure interactions in a stented abdominal aortic aneurysm model*, Medical Engineering & Physics, 27 (2005), pp. 369–382.

[45] T.-M. Liou, W.-C. Chang, and C.-C. Liao, *Ldv measurements in lateral model aneurysms of various sizes*, Experiments in Fluids, 23 (1997), pp. 317–324.

[46] T.-M. Liou and C.-C. Liao, *Flowfields in lateral aneurysm models arising from parent vessels with different curvatures using ptv*, Experiments in Fluids, 23 (1997), pp. 288–298.

[47] M. Löw, K. Perktold, and R. Raunig, *Hemodynamics in rigid and distensible saccular aneurysms: a numerical study of pulsatile flow characteristics.*, Biorheology, 30 (1992), pp. 287–298.

[48] R. J. MacKinnon and R. W. Johnson, *Differential-equation-based representation of truncation errors for accurate numerical simulation*, International Journal for Numerical Methods in Fluids, 13 (1991), pp. 739–757.

[49] A. H. Mahmoudi, M. Shahi, and F. Talebi, *Effect of inlet and outlet location on the mixed convective cooling inside the ventilated cavity subjected to an external nanofluid*, International Communications in Heat and Mass Transfer, 37 (2010), pp. 1158–1173.

[50] S. Mahmud and A. S. Islam, *Laminar free convection and entropy generation inside an inclined wavy enclosure*, International Journal of Thermal Sciences, 42 (2003), pp. 1003–1012.

[51] M. Mamun, M. Rahman, R. Saidur, S. Nagata, and T. Tanim, *Analysis of Mixed Convection in a Lid Driven Trapezoidal Cavity*, INTECH Open Access Publisher, 2011.

[52] O. Manca, S. Nardini, K. Khanafer, and K. Vafai, *Effect of heated wall position on mixed convection in a channel with an open cavity*, Numerical Heat Transfer: Part A: Applications, 43 (2003), pp. 259–282.

[53] R. Mansour and R. Viskanta, *Shear-opposed mixed-convection flow and heat transfer in a narrow, vertical cavity*, International Journal of Heat and Fluid Flow, 15 (1994), pp. 462–469.

[54] W. D. McQuain, C. J. Ribbens, C.-Y. Wang, and L. T. Watson, *Steady viscous flow in a trapezoidal cavity*, Computers & Fluids, 23 (1994), pp. 613–626.

[55] C. Midya, G. Layek, A. Gupta, and T. R. Mahapatra, *Magnetohydrodynamic viscous flow separation in a channel with constrictions*, Journal of Fluids Engineering, 125 (2003), pp. 952–962.

[56] J. Misra, B. Pal, and A. Gupta, *Hydromagnetic flow of a second-grade fluid in a channelsome applications to physiological systems*, Mathematical Models and Methods in Applied Sciences, 8 (1998), pp. 1323–1342.

[57] M. Moallemi and K. Jang, *Prandtl number effects on laminar mixed convection heat transfer in a lid-driven cavity*, International Journal of Heat and Mass Transfer, 35 (1992), pp. 1881–1892.

[58] A. Mohamad and R. Viskanta, *Laminar flow and heat transfer in rayleigh–benard convection with shear*, Physics of Fluids A: Fluid Dynamics (1989-1993), 4 (1992), pp. 2131–2140.

[59] ——, *Flow structures and heat transfer in a lid-driven cavity filled with liquid gallium and heated from below*, Experimental Thermal and Fluid Science, 9 (1994), pp. 309–319.

[60] ——, *Flow and heat transfer in a lid-driven cavity filled with a stably stratified fluid*, Applied Mathematical Modelling, 19 (1995), pp. 465–472.

[61] B. Noye and H. Tan, *Finite difference methods for solving the two-dimensional advection–diffusion equation*, International Journal for Numerical Methods in Fluids, 9 (1989), pp. 75–98.

[62] A. Omri and S. B. Nasrallah, *Control volume finite element numerical simulation of mixed convection in an air-cooled cavity*, Numerical Heat Transfer: Part A: Applications, 36 (1999), pp. 615–637.

[63] S. Ostrach, *Natural convection in enclosures*, Journal of Heat Transfer, 110 (1988), pp. 1175–1190.

[64] H. Ozoe and K. Okada, *The effect of the direction of the external magnetic field on the three-dimensional natural convection in a cubical enclosure*, International Journal of Heat and Mass Transfer, 32 (1989), pp. 1939–1954.

[65] H. F. Oztop, E. Abu-Nada, Y. Varol, and A. Chamkha, *Natural convection in wavy enclosures with volumetric heat sources*, International Journal of Thermal Sciences, 50 (2011), pp. 502–514.

[66] H. F. Oztop and I. Dagtekin, *Mixed convection in two-sided lid-driven differentially heated square cavity*, International Journal of Heat and Mass Transfer, 47 (2004), pp. 1761–1769.

[67] B. Pal, J. Misra, and A. Gupta, *Steady hydromagnetic flow in a slowly varying channel*, Proceedings-National Academy of Sciences, India. Section A, Physical Sciences, 66 (1996), pp. 247–262.

[68] S. K. Pandit, J. C. Kalita, and D. Dalal, *A transient higher order compact scheme for incompressible viscous flows on geometries beyond rectangular*, Journal of Computational Physics, 225 (2007), pp. 1100–1124.

[69] E. Papanicolaou and Y. Jaluria, *Mixed convection from an isolated heat source in a rectangular enclosure*, Numerical Heat Transfer, 18 (1991), pp. 427–461.

[70] ——, *Transition to a periodic regime in mixed convection in a square cavity*, Journal of Fluid Mechanics, 239 (1992), pp. 489–509.

[71] ——, *Mixed convection from a localized heat source in a cavity with conducting walls: a numerical study*, Numerical Heat Transfer, Part A Applications, 23 (1993), pp. 463–484.

[72] ——, *Mixed convection from simulated electronic components at varying relative positions in a cavity*, Journal of Heat Transfer, 116 (1994), pp. 960–970.

[73] ——, *Computation of turbulent flow in mixed convection in a cavity with a localized heat source*, Journal of Heat Transfer, 117 (1995), pp. 649–658.

[74] V. Patel and M. Head, *Some observations on skin friction and velocity profiles in fully developed pipe and channel flows*, Journal of Fluid Mechanics, 38 (1969), pp. 181–201.

[75] K. Pavlov, *Magnetohydrodynamic flow of an incompressible viscous fluid caused by deformation of a plane surface*, Magnitnaya Gidrodinamika, 4 (1974), pp. 146–147.

[76] R. A. Peattie, T. J. Riehle, and E. I. Bluth, *Pulsatile flow in fusiform models of abdominal aortic aneurysms: flow fields, velocity patterns and flow-induced wall stresses*, Journal of Biomechanical Engineering, 126 (2004), pp. 438–446.

[77] L. A. B. Pilkington, *Review lecture. the float glass process*, Proceedings of the Royal Society of London. Series A, Mathematical and Physical Sciences, 314 (1969), pp. 1–25.

[78] M. Pirmohammadi and M. Ghassemi, *Effect of magnetic field on convection heat transfer inside a tilted square enclosure*, International Communications in Heat and Mass Transfer, 36 (2009), pp. 776–780.

[79] A. K. Prasad and J. R. Koseff, *Combined forced and natural convection heat transfer in a deep lid-driven cavity flow*, International Journal of Heat and Fluid Flow, 17 (1996), pp. 460–467.

[80] M. Rahman, M. Alim, M. Mamun, M. Chowdhury, and A. Islam, *Numerical study of opposing mixed convection in a vented enclosure*, ARPN Journal of Engineering and Applied Sciences, 2 (2007), pp. 25–36.

[81] A. Raji and M. Hasnaoui, *Mixed convection heat transfer in a rectangular cavity ventilated and heated from the side*, Numerical Heat Transfer, Part A Applications, 33 (1998), pp. 533–548.

[82] ——, *Mixed convection heat transfer in a rectangular cavity ventilated and heated from the side*, Numerical Heat Transfer, Part A Applications, 33 (1998), pp. 533–548.

[83] ——, *Mixed convection heat transfer in ventilated cavities with opposing and assisting flows*, Engineering Computations, 17 (2000), pp. 556–572.

[84] ——, *Combined mixed convection and radiation in ventilated cavities*, Engineering Computations, 18 (2001), pp. 922–949.

[85] N. Rudraiah, R. Barron, M. Venkatachalappa, and C. Subbaraya, *Effect of a magnetic field on free convection in a rectangular enclosure*, International Journal of Engineering Science, 33 (1995), pp. 1075–1084.

[86] T. Sekhar and B. H. S. Raju, *An efficient higher order compact scheme to capture heat transfer solutions in spherical geometry*, Computer Physics Communications, 183 (2012), pp. 2337–2345.

[87] ——, *Spherical geometry hoc scheme to capture low pressures within a wake*, East Asian Journal on Applied Mathematics, 3 (2013), pp. 93–106.

[88] T. Sekhar, B. H. S. Raju, and P. Murthy, *Higher order compact scheme for laminar natural convective heat transfer from a sphere*, Applied Mathematical Modelling, 40 (2016), pp. 2039–2055.

[89] T. Sekhar, B. H. S. Raju, and Y. Sanyasiraju, *Higher-order compact scheme for the incompressible navier-stokes equations in spherical geometry*, Communications in Computational Physics, 11 (2012), pp. 99–113.

[90] S. Sen, *A new family of (5, 5) cc-4oc schemes applicable for unsteady navier–stokes equations*, Journal of Computational Physics, 251 (2013), pp. 251–271.

[91] J. Sesterhenn, *A characteristic-type formulation of the navier–stokes equations for high order upwind schemes*, Computers & Fluids, 30 (2000), pp. 37–67.

[92] P. Shankar, V. Meleshko, and E. Nikiforovich, *Slow mixed convection in rectangular containers*, Journal of Fluid Mechanics, 471 (2002), pp. 203–217.

[93] M. Sharif, *Laminar mixed convection in shallow inclined driven cavities with hot moving lid on top and cooled from bottom*, Applied Thermal Engineering, 27 (2007), pp. 1036–1042.

[94] M. Sheikholeslami, H. R. Ashorynejad, D. Domairry, and I. Hashim, *Investigation of the laminar viscous flow in a semi-porous channel in the presence of uniform magnetic field using optimal homotopy asymptotic method*, Sains Malaysiana, 41 (2012), pp. 1177–1229.

[95] S. Singh and M. Sharif, *Mixed convective cooling of a rectangular cavity with inlet and exit openings on differentially heated side walls*, Numerical Heat Transfer: Part A: Applications, 44 (2003), pp. 233–253.

[96] P. Sompong and S. Witayangkurn, *Simulation of natural convection in a complicated enclosure with two wavy vertical walls*, Applied Mathematical Sciences, 6 (2012), pp. 2833–2842.

[97] W. Spotz and G. Carey, *High-order compact scheme for the steady stream-function vorticity equations*, International Journal for Numerical Methods in Engineering, 38 (1995), pp. 3497–3512.

[98] H. Steiger, A. Poll, D. Liepsch, and H.-J. Reulen, *Haemodynamic stress in lateral saccular aneurysms*, Acta Neurochirurgica, 86 (1987), pp. 98–105.

[99] H. Steiger, A. Poll, D. Liepsch, and H.-J. Reulen, *Haemodynamic stress in terminal aneurysms*, Acta Neurochirurgica, 93 (1988), pp. 18–23.

[100] H. J. Steiger, A. Poll, D. Liepsch, and H.-J. Reulen, *Basic flow structure in saccular aneurysms: a flow visualization study*, Heart and Vessels, 3 (1987), pp. 55–65.

[101] J. Stephenson, *Single cell discretizations of order two and four for biharmonic problems*, Journal of Computational Physics, 55 (1984), pp. 65–80.

[102] C. M. Strother, V. B. Graves, and A. Rappe, *Aneurysm hemodynamics: an experimental study.*, American Journal of Neuroradiology, 13 (1992), pp. 1089–1095.

[103] K. Torrance, R. Davis, K. Eike, P. Gill, D. Gutman, A. Hsui, S. Lyons, and H. Zien, *Cavity flows driven by buoyancy and shear*, Journal of Fluid Mechanics, 51 (1972), pp. 221–231.

[104] H. Ujiie, D. W. Liepsch, M. Goetz, R. Yamaguchi, H. Yonetani, and K. Takakura, *Hemodynamic study of the anterior communicating artery*, Stroke, 27 (1996), pp. 2086–2094.

[105] V. Vardanian, *Effect of a magnetic field on blood flow*, Biofizika, 18 (1972), pp. 491–496.

[106] M. Venkatachalappa and C. Subbaraya, *Natural convection in a rectangular enclosure in the presence of a magnetic field with uniform heat flux from the side walls*, Acta Mechanica, 96 (1993), pp. 13–26.

[107] M. R. Visbal and D. V. Gaitonde, *On the use of higher-order finite-difference schemes on curvilinear and deforming meshes*, Journal of Computational Physics, 181 (2002), pp. 155–185.

[108] W.-J. Yang, Orhan Aydin, *Mixed convection in cavities with a locally heated lower wall and moving sidewalls*, Numerical Heat Transfer: Part A: Applications, 37 (2000), pp. 695–710.

[109] M. Yanwen, F. Dexun, T. Kobayashi, and N. Taniguchi, *Numerical solution of the incompressible navier-stokes equations with an upwind compact difference scheme*, International Journal for Numerical Methods in Fluids, 30 (1999), pp. 509–521.